Transport in manganites under high pressure and single-walled carbon nanotubes

by Keith Bradley

B.A. (University of Chicago) 1996
C.A.S. (University of Cambridge) 1996

A dissertation submitted in partial satisfaction of the

requirements for the degree of

Doctor of Philosophy

in

Physics

in the

GRADUATE DIVISION

of the UNIVERSITY OF CALIFORNIA AT BERKELEY

Committee in Charge:

Professor Alex Zettl, Chair

Professor Marvin Cohen

Professor Norman Phillips

Spring 2001

Transport in manganites under high pressure and single-walled carbon nanotubes

Keith Bradley

Abstract

Transport in manganites at high pressure and single-walled carbon nanotubes

Keith Bradley

Doctor of Philosophy in Physics

University of California at Berkeley

Professor Alex K. Zettl, Chair

This thesis consists of two parts. The first part discusses a high-pressure search for superconductivity in manganites. Colossal magnetoresistance manganites are reviewed. No superconductivity is observed in $La_{0.6}Pb_{0.4}MnO_3$ or $Nd_{0.66}Pb_{0.33}MnO_3$ at pressures up to 150 kbar and temperatures down to 2.2 K. New techniques for measuring resistance under hydrostatic pressure, developed for this experiment, are described in detail.

The second part discusses several transport experiments on single-walled carbon nanotubes. The thermoelectric power of bulk samples is examined to identify the effect of atmospheric gas. Negative thermopower is discovered in degassed nanotubes. The binding energy of adsorbed oxygen on nanotubes is estimated to be 0.4 eV. A model involving degenerate doping is presented to account for the range of thermopower data. Measure-

ments of $1/f$ noise support the idea that oxygen adds carriers to nanotubes. The last chapter describes an attempt to observe shot noise in carbon nanotube devices. Measurements of noise is measured as a function of frequency between 100 MHz and 1 GHz obviate the $1/f$ noise spectrum. The first measurement is reported, in which diffusive conduction is observed in a nanotube rope device 1 micron long.

Acknowledgments

Many people have contributed both to this thesis and to my education. From these people, as well as many others, I learned a great deal, though not as much as they had to teach.

Professors Alex Zettl and Marvin Cohen in Berkeley and Professor Gil Lonzarich in Cambridge have shown me how to do science. Professors Norman Phillips, Peter Yu, Steven Louie, Paul McEuen, and Raymond Jeanloz were generous of their time and thought. John Donovan and Bob Prohaska helped with much of the manganites synthesis and analysis. At those points where the work balanced on a point, crucial intervention came from Lincoln Bourne, Reinhardt Buehler, and especially Stan Tozer and Seung-Hoon Jhi. I also engaged in helpful discussions with Isaac Silvera.

I am grateful to Anne Takizawa, Lynn Pelosi, and Caroline Day for smoothing the path. The machinists of the physics department are excellent teachers. George Webber and Tom Pedersen, and Joseph Kant taught me how to design and how to build. Marco Ambrosini, Alex Vaynberg, and Dave Murai made many of the parts. Drawings that I did not myself entirely believe possible turned into real experiments in their hands. Steve Butler, the man behind the Zettl labs' electron-beam evaporator, was a constant source of cheer. Armando Baeza made the diamond anvil cell, and I always enjoyed talking with him.

A great cast of graduate students, postdocs, and undergraduates befriended me and gave me ideas. The list is too long to give completely, but includes Robin Benedetti,

Charles Piskoti, Thomas Wagberg, Willi Mickelson, Brian Demczyk, Weiqiang Han, Mike Calvisi, Jacob Sprunck, David Roundy, Connie Tung, and Filipe Ribeiro. I admire the courage of Uday Varadarajan and Helene Grossman. Ashley Christianson and Renee Bulow did important parts of the work. Kasra Khazeni built the first Zettl group diamond anvil cell. F. Malte Grosche in Cambridge provided my first laboratory training. Jeff Gore and Manu Forero worked out the local recipe for nanotube devices. Phil Collins, Jim Hone and Michael Fuhrer are still serving me as models. Phil generously introduced me to nanotubes and their problems. Xiaosheng Huang, who will be carrying on the high-pressure project, was a constant optimist in the last year. Adam Fennimore, Masa Ishigami, John Cumings, and Aileen Wang made the lab a wonderful place to live and to work.

I needed my wife Kathleen, and she responded. I do not think that this work would have been possible without her support. My parents and her parents were also extremely helpful.

CHAPTER 1

Colossal Magnetoresistance Manganites

Although the unusual phenomenon in these materials of double exchange magnetism has been known since 1951[1], interest has surged in the last decade. Their technological potential, particularly as magnetic field sensors in magnetic storage devices, has driven research in sample synthesis. The 1993 discovery of large negative magnetoresistance in films of $La_{1-x}Ba_xMnO_3$ and in $La_{1-x}Ca_xMnO_3$ revealed the inadequacy of the double exchange model.[2,3] Subsequent observations, including persistent photoconductivity, polaron conduction, and colossal magnetoresistance in stoichiometric compounds, have deepened this mystery.

The manganites are a particularly complex genus of the family of transition metal perovskites. Their cousins include the high-temperature superconductors, in which superconductivity and antiferromagnetism compete, and the ferroelectric and piezoelectric strontium titanate. In all of these materials, exchange interactions produce strong correlation between the holes which dope them. A number of effects complicate the picture in the manganese perovskites. Double exchange from the cation substitution doping is the best understood of these. The Jahn-Teller effect of manganese ions couples the carriers to the lattice. In addition, the role of the strong disorder is difficult to calculate.

Perovskite substances with stoichiometry ABO_3 crystallize in the nearly cubic structure shown in Fig. 1. In the ideal structure, A atoms occupy the vertices of the conven-

tional cubic cell, with B atoms at the center. At the face centers, the O atoms surround the B atoms in octahedra. In most realizations of this structure, such as $SrRuO_3$, $LaCuO_3$, $CaFeO_3$, the A atoms are strong electron donors, and the Fermi level runs through the d levels of the transition metal B atoms. There is no direct overlap between B atoms, so that these levels are usually hybridized with the oxygen $2p$ levels. Because the transfer term between B atoms is indirect, the $d-p$ bands are much narrower than in the elemental metals.

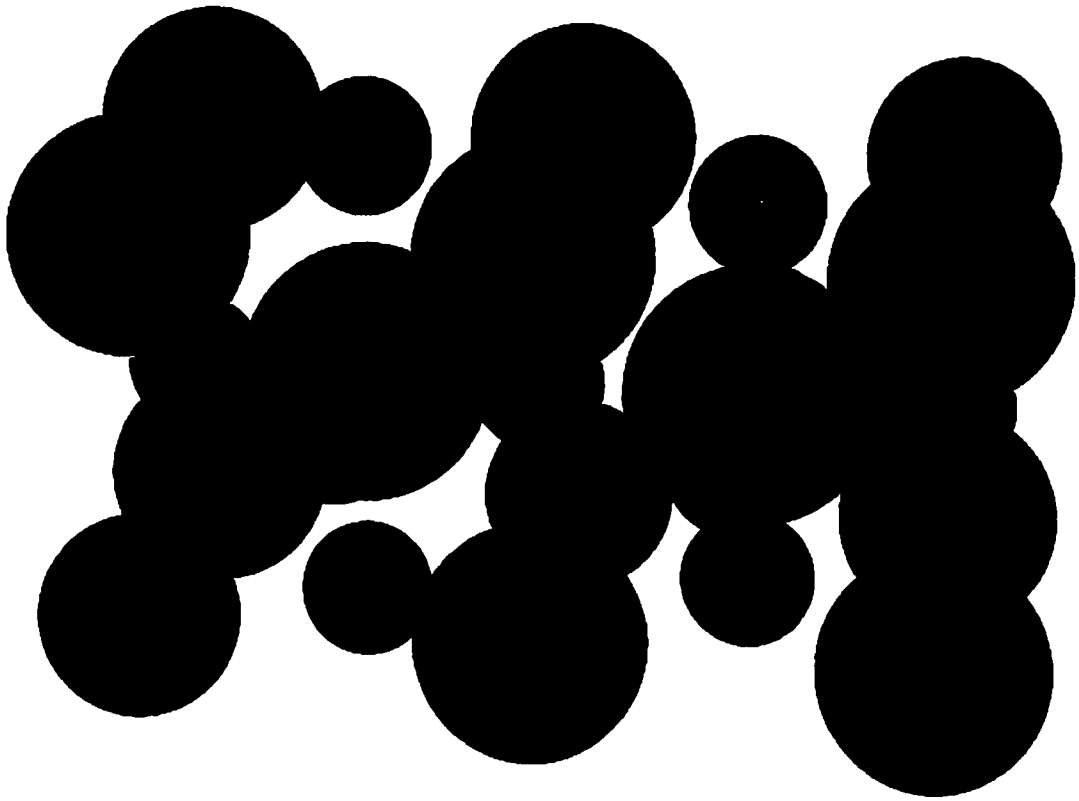

Figure 1. The prototype perovskite structure of $LaMnO_3$.

Structure

The prototype manganite is $LaMnO_3$, with a lattice parameter of 0.386 nm.[4] Most of the structural complications that play a role in the manganites can be observed in this material. It has therefore been studied in some detail,[5,6] and it serves as a useful model to introduce these complications.

To begin with, the crystal is slightly distorted from cubic by a size mismatch between the two cations. An ideal cubic crystal would feature ionic radii r_A, r_B, and r_O, such that the oxygen ions are packed well with the cations: $t = \left(\frac{r_A + r_O}{\sqrt{2}(r_B + r_O)}\right) = 1$. When this tolerance factor t is less than one, the cubic lattice is unstable because of the additional attraction between A and O atoms. The cell volume decreases by two mechanisms. The rhombohedral distortion brings opposite A atoms closer together and increases the vertex angle to 92°.[4] In addition, the MnO_6 octahedra tilt to move the long Mn-O bonds away from the crystallographic axes. Adjacent octahedra tilt in opposite directions, as shown in Fig. 2, to produce a complicated orthorhombic or even monoclinic structure. In $LaMnO_3$ the zigzag Mn-O-Mn angle is a substantial 160°.[5]

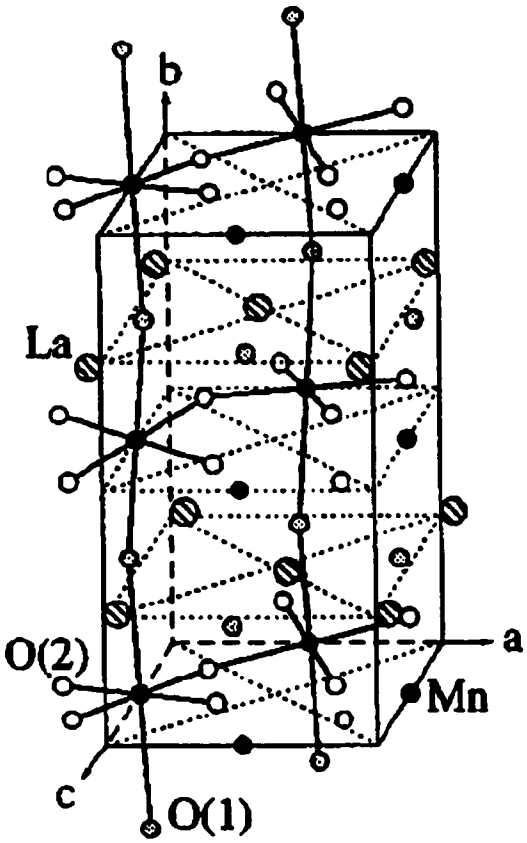

Figure 2. Bond buckling from cation size mismatch.[5]

The structure is further distorted by the well-known Jahn-Teller effect of Mn^{+3} ions. Each oxygen moves closer to one Mn neighbor, 0.192 nm, and farther from the other, 0.216 nm.[7] The octahedra are stretched in one direction and compressed in the perpendicular plane. Although the role of the Jahn-Teller distortion in determining the magnetic and orbital ordering have long been suspected, a static, ordered Jahn-Teller distortion was only first directly observed by Rodriguez-Carvajal *et al.* in 1998.[8] The alternately directed distortions form a checkerboard in the ab-plane. A first-order transition to an undistorted cubic phase was observed at 750 K. (A fascinating feature that will not be discussed in this brief review is the associated ordering of electronic orbitals.[9])

Colossal magnetoresistance

$LaMnO_3$ can be doped with holes by two means. Unlike most perovskites, this material tends to incorporate an excess of oxygen by means of cation vacancies rather than by interstitial oxygen.[10] Compositions as far as $LaMnO_{3.18}$[6,11] have been synthesized.

Because the Mn^{+4} ion is not Jahn-Teller active, this doping weakens the Jahn-Teller order and lowers the ordering temperature. The transition temperature crosses room temperature at the composition $LaMnO_{3.06}$. Much higher doping levels can be achieved by substituting divalent cations,[12,13,14,15] such as Ca^{+2}, Sr^{+2}, or Pb^{+2}, for lanthanum. In each series such as $La_{1-x}Ca_xMnO_3$ (LCMO-x), the rhombohedral, tilt, and Jahn-Teller distortions vary with the average cation radius.[16] These variations combine with the heavy hole doping and strong disorder of the cation substitution to produce a rich variety of electronic and magnetic phases.

All these materials feature spins localized at the manganese sites which order below Neel or Curie temperatures. In stoichiometric $LaMnO_3$ below 140 K, spins of 3 μ_B per ion are ferromagnetically ordered in the *ab* plane; ordered planes are antiferromagnetically ordered along the *c* axis, in a structure termed A type.[17,18,19] As cation deficiency increases, weakening the Jahn-Teller order, the bond-buckling Mn-O-Mn angle increases towards 180°. Meanwhile, the spin order, observed by neutron scattering, quickly evolves towards ferromagnetism, becoming fully ferromagnetic at $\delta = 0.1$. Huang *et al.*[20] observed suppression of the antiferromagnetic order in calcium-doped samples by $x = 0.06$. They attributed the difference to the presence of additional oxygen doping.

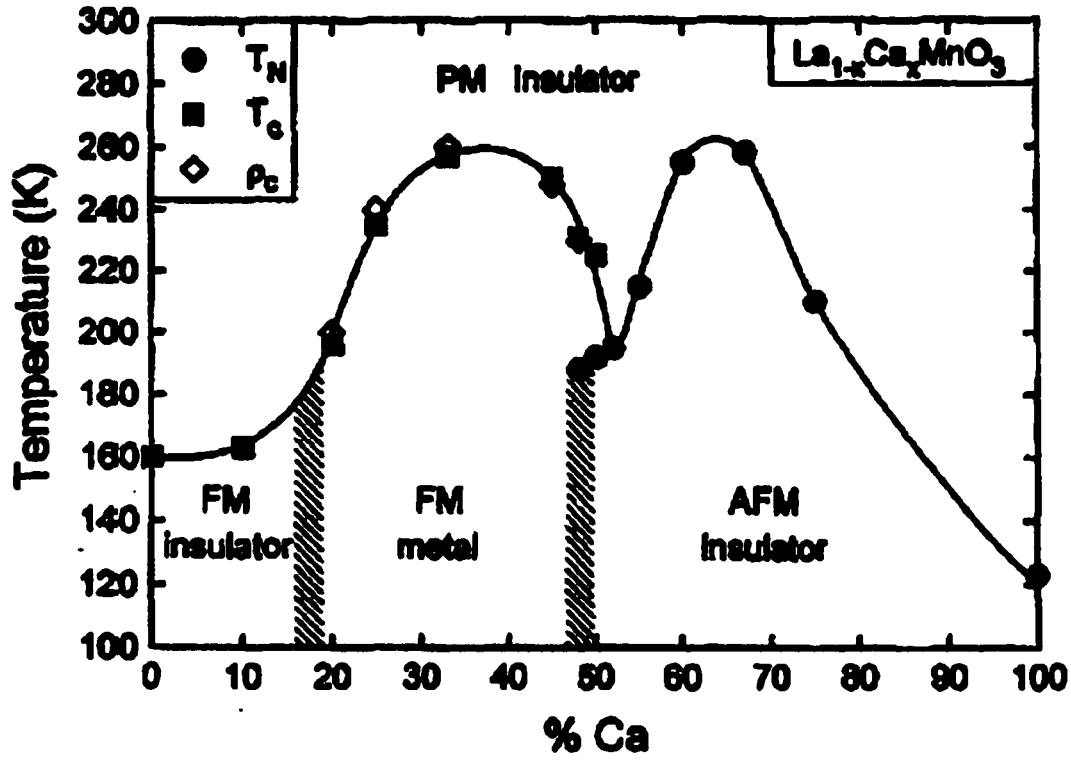

Figure 3. The phase diagram of $La_{1-x}Ca_xMnO_3$, determined by Schiffer *et al.*[21]

The magnetic phase diagram of the complete strongly doped LCMO system, shown in Fig. 3, was mapped by Schiffer *et al.*[21] in 1995 using magnetization and resistance measurements. Although they were unable to observe the antiferromagnetic state at $x = 0$, probably because of oxygen non-stoichiometry, several major phases could be distinguished in their samples. In the ferromagnetic insulator for $x < 0.2$, they observed a saturation magnetization of 2.7 μ_B per ion, which is consistent with neutron diffraction data.[20] The materials between $x = 0.5$ and $x = 1$ are antiferromagnetic insulators. Their magnetic structures are presumably similar to the G-type, rock salt-like order of $CaMnO_3$, in which neighboring spins alternate directions.[22] Very near $x = 0.5$, there is a

reentrant antiferromagnetic transition below a ferromagnetic transition. This magnetic reordering is a strongly first-order transition that is related to the charge-ordering that will be described later. In a special range of doping, $0.2 \leq x \leq 0.5$, the low-temperature phase is a ferromagnetic metal; and it is in this range that colossal magnetoresistance is observed.

The resistivity and the ferromagnetism are coupled together by the double-exchange mechanism to be discussed later. A manganite sample in the paramagnetic phase has zero spontaneous magnetization and behaves as an insulator. As its temperature is lowered, the sample develops a spontaneous magnetization below the Curie temperature, and the resistance drops precipitously. As the temperature is lowered further, critical fluctuations decrease, the magnetization increases, and the resistivity continues to drop. If a magnetic field is applied, at any temperature, the magnetization increases, and the resistivity decreases. Just above the Curie temperature, the resistivity is particularly high because of its insulating characteristic. In a field strong enough to saturate the magnetization, the sample becomes metallic and the resistivity drops to nearly its $T = 0$ value. So the magnetoresistance shows a dramatic peak near the Curie temperature.

Theory of double exchange

The basic mechanism for the metal-insulator transition is the link between magnetism and transport provided by double exchange. This interaction was first proposed by Zener[1] in 1951 and was subsequently analyzed in a mean field treatment by Anderson and Haseg-awa,[23] de Gennes,[24] and Kubo and Ohata.[25] The degenerate $3d$ orbitals of the manganese atoms are split, first by intra-atomic exchange and then by their cubic environments,

into three t_{2g} and two e_g levels. In the Mn^{+4} ion present in the $x = 1$ end compound, the t_{2g} levels are half-filled. In the Mn^{+3} ion present in the $x = 0$ compound, the e_g level contains one electron, which causes the Jahn-Teller distortion. The manganese d electrons, with no direct coupling, interact only through indirect couplings through the intervening atoms, such as the weak superexchange interaction to be discussed later. But in the intermediate, heavily doped compounds, double exchange is possible due to hopping of electrons from Mn^{+3} to Mn^{+4}.

Zener observed that the system comprising a Mn^{+3} ion, a Mn^{+4} ion, an O^{-2} ion, and their electrons is apparently degenerate. The extra electron, in the e_g orbital, can be on either manganese ion without affecting the single-atom energies. Including intraatomic exchange by means of Hund's rule, there are eight states that can be written down: $3d^4_{1/2}2p^6 3d^3_{1/2}$, $3d^4_{1/2}2p^6 3d^3_{-1/2}$, $3d^3_{1/2}2p^6 3d^4_{1/2}$, $3d^3_{1/2}2p^6 3d^4_{-1/2}$, and those with the opposite spins. In the presence of interactions, the degenerate orbitals will mix to form bonding and antibonding orbitals. As long as the interaction is spin-preserving, only those pairs of orbitals, such as $3d^4_{1/2}2p^6 3d^3_{1/2}$ and $3d^3_{1/2}2p^6 3d^4_{1/2}$, in which the spin wavefunctions overlap can produce the low-energy bonding orbitals. The difference in energy between these bonding orbitals and the unmixed, opposite-spin orbitals thus constitutes an effective spin coupling. A model Hamiltonian for the crystal can be written $H = J\sum(\bar{S}\cdot\bar{\sigma})_{ij}(c^\dagger_i c_j) + \sum t_{ij}(c^\dagger_i c_j)$.[25] Traditionally, following Anderson and Hasegawa, the Hund's rule coupling J has been taken to be infinite. The effective Hamiltonian is then $H = J\sum t_{ij}\cos(\Theta_{ij}/2)c^\dagger_i c_j$, where Θ is the angle between neighboring sites'

spins. The interesting appearance of $\Theta/2$ rather than Θ refers to the facts discussed above: Antiparallel pairs of spins, with $\Theta = \pi$, are not split, while parallel spins are split into bonding and antibonding orbitals ($\Theta = 0$ and $\Theta = 2\pi$).

Double exchange affects magnetization in a relatively straightforward way. The energy to be gained from spin alignment causes double exchange manganites to be ferromagnetically ordered at low temperature. The effect on transport is indirect. In the ferromagnetic state, the charge carriers should occupy states in a broad band determined by the large transfer term t_{ij}. Above the critical temperature, they experience a disordered environment, as $\cos\Theta_{ij}/2$ varies from site to site. The disorder should localize them in an Anderson transition. The process of exchange-induced magnetic order below a critical temperature is common to many transition-metal oxides. The manganites are unusual. Because double exchange is a real interaction (as opposed to a virtual interaction) and takes place in strongly doped systems, the ferromagnetic state is metallic. The process of localization is likewise common in disordered systems. In the manganites, however, the disorder has a significant magnetic origin.

An applied field increases spin order at a given temperature, and thus decreases the electrical resistivity. To some extent, then, the colossal magnetoresistance may be regarded as a vindication of the double exchange model. In recent years the discovery of colossal magnetoresistance in nominally undoped pyrochlore manganites[29] has undermined this notion. But any failure of double exchange to serve that system does not make it less successful in the perovskite manganites of known doping. Some key ingredients

have been more directly verified. Using manganese X-ray emission to probe manganese core electronic environments, Tyson *et al.*[26] demonstrated that the manganese valences are +4 and +3 in the correct ratios, without any disproportionation to +2. Transitions between the exchange-split manganese states have been observed by optical spectroscopy.[27] The hybridized character of the states at the Fermi level have been confirmed by electron energy-loss spectroscopy[13] in which holes in the O $2p$ band were observed.

An early extension of the model by Searle and Wang[28] predicted the formation of a half metal. This unusual feature has been described in detail by Pickett and Singh[31] on the basis of the calculated band structure shown in Fig. 4. In an itinerant-electron ferromagnet such as iron, the bands of majority spin and minority spin electrons are shifted down and up, respectively, by the itinerant exchange. Excess majority spin due to this filling produces the magnetization. Since the spin-dependent double-exchange term determines the bandwidth in the manganites, the effect of ferromagnetic polarization can be even stronger. The minority spin carriers in the background of polarized spins in fact occupy the unsplit ($\Theta = \pi$) orbitals discussed earlier. The majority spin band is lowered and broadened by the exchange, to have a bandwidth of order 1 eV. Consequently the minority carriers have a gap, while the majority carriers are metallic. In contrast to iron, the bulk of

the magnetization arises from the localized t_{2g} electrons, with $S = 3/2$. The experimental signature, a large spin polarization at the Fermi level, was first resolved unambiguously in $La_{1-x}Sr_xMnO_3$ by spin-polarized photoemission spectroscopy.[32] Wei *et al.*[33] observed the exchange-split bonding and antibonding orbitals in LCMO by scanning tunneling spectroscopy.

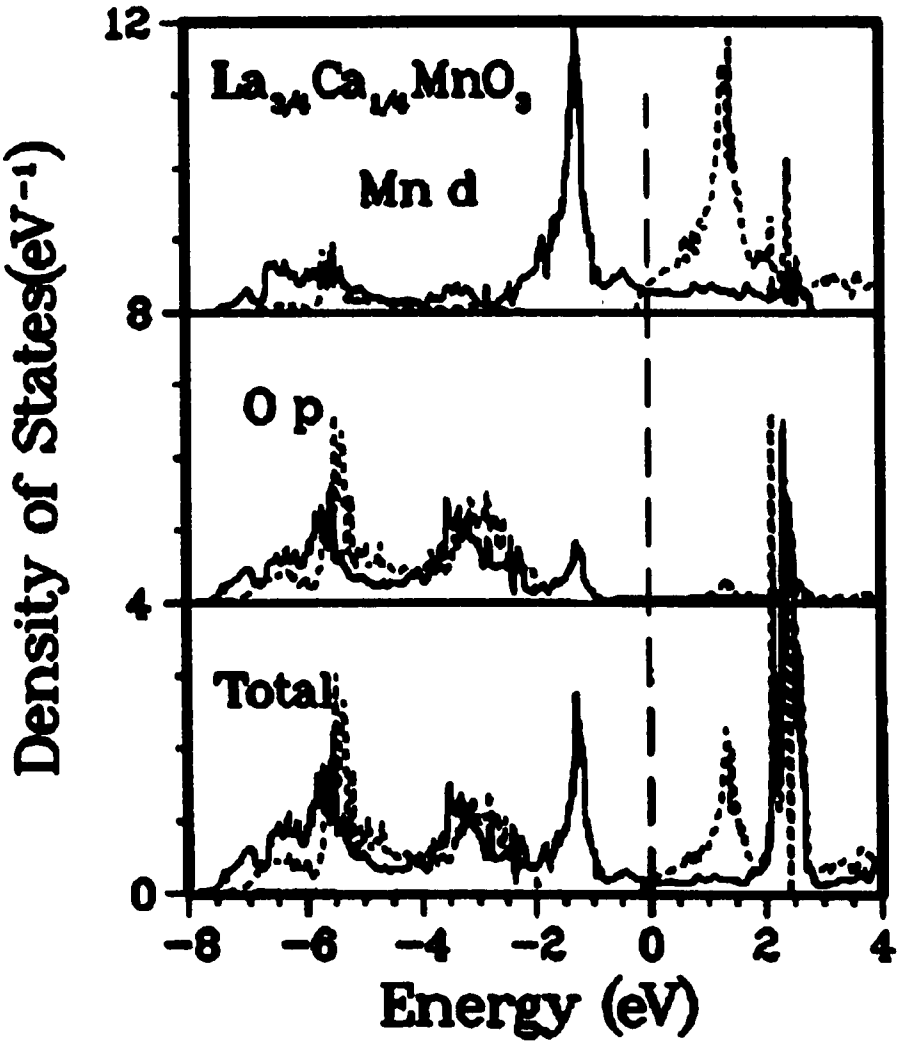

Figure 4. Pickett and Singh's nearly half-metallic band structure.[31]

Competing interactions

Double exchange has little to say about the boundaries of the ferromagnetic metallic phase in the $x - T$ diagram. If it were the only interaction, the entire composition series should feature colossal magnetoresistance and metal-insulator transitions at low temperature. The boundaries can be discussed in order of increasing complexity. At the low-doping end, the increasingly strong antiferromagnetic interactions eventually dominate, producing an antiferromagnetic insulator. At the high-doping end, charge and orbital ordering set in at the commensurate concentration $x = 0.5$. Meanwhile, throughout the phase diagram, interaction with the Jahn-Teller distorted lattice weakens the metallicity in profound ways.

Superexchange

Superexchange is the more common interaction involving identical atoms in transition metal oxides. The name refers to a variety of virtual exchange processes involving either the t_{2g} or e_g electrons. For example, in Mn^{+4}-O^{-2}-Mn^{+4} systems there is a process involving the hopping of a t_{2g} electron through the oxygen to the other manganese and back to its source. Such processes generally second-order perturbation terms, with energies proportional to t^4, rather than the t^2 of double exchange. They are also generally antiferromagnetic; as in this example, the Pauli exclusion principle and Hund's rule force the interaction term to be zero when both atoms have the same spin.

Superexchange interactions play an important role in determining the boundaries of the ferromagnetic metal phase in the $x - T$ diagram. An early model of this effect at the

low x end by de Gennes[24] began from the layered antiferromagnetic structure of $LaMnO_3$. The magnetic structure is stabilized by the antiferromagnetic coupling between layers produced by superexchange. This coupling energy, proportional to $\cos\Theta$ (Θ is the angle between the spins of adjacent layers) competes with a ferromagnetic double exchange coupling energy proportional to $\cos\Theta/2$ and to the doping level x. As doping increases, the spins between adjacent layers cant with respect to each other by an angle $\cos\Theta/2 = xt/(JS^2)$; indeed this feature is observed experimentally, as described above. To some extent, then, the disappearance of the ferromagnetic metallic phase at small hole doping can be regarded as a strengthening of superexchange-induced antiferromagnetism at the expense of double exchange.

Charge ordering

In the other direction, as x increases, the ferromagnetic critical temperature first increases and then, after a maximum near $x = 0.35$, decreases again. The conductivity of the high-temperature paramagnetic insulating phase increases and decreases simultaneously. Worledge *et al.*[34] explained this behavior in terms of a Hubbard-like interaction. In their model, conduction takes place by the hopping of hole-like carriers. As the number of carriers increases, on-site repulsion forces each site to be singly occupied. This restriction on the hopping causes the conductivity to decrease.

By $x = 0.5$, the low-temperature metallic state disappears. What appears is a complicated competition between different magnetic, electronic, and structural phases. A ferromagnetic transition at 225 K in LCMO-0.5 is followed by an antiferromagnetic

transition at 155 K; the reentrant transition is partly due to the competition between double exchange and superexchange. The antiferromagnetic state is also characterized by charge ordering. Sheng and Ting[35] incorporated a form of long-range Coulomb repulsion into a more detailed double-exchange model. They concluded that the carrier repulsion favors the segregation of ions and carriers into lines or sheets of fixed charge.

Powder X-ray diffraction patterns[36,37] manifest additional peaks that indicate long-range order in this segregation. The structure consists of sheets of Mn^{+3} ions separated by sheets of Mn^{+4} ions. Mori *et al.*[38] reported beautiful real-space TEM images of this structure for a variety of doping levels greater than 0.5. At several commensurate concentrations, such as 1/2, 2/3, and 3/4, there are charge-ordered structures in which successive Mn^{+3} layers from the 1/2 structure are replaced by Mn^{+4}. Intermediate dopings segregate into small commensurate regions.

The $x = 0.5$ charge-ordered state is quite fragile. Small amounts of incommensurability, due to oxygen non-stoichiometry can cause a sample to phase-separate into nanometer-sized ferromagnetic metallic and antiferromagnetic charge-ordered domains.[36] In several materials the ferromagnetic metallic state is actually metastable at $x = 0.5$. Kuwahara *et al.* found a first-order, hysteretic insulator-metal transition in $Nd_{1-x}Sr_xMnO_3$ under applied magnetic field.[39] Several groups have induced[40] the transition in $Pr_{1-x}Ca_xMnO_3$ by both X-ray and infrared irradiation. The Tokura group has even activated the transition with a high applied electric field.[42] All these persistent photo-, magneto-, and electro-conductivity effects depend sensitively on sample doping level. Slightly away

from the half-doped boundary, the metallic state persists for long times after the transition; while at the boundary, the metallic state exists only in filaments as long as current is still being carried.

Jahn-Teller polarons

The Jahn-Teller distortion plays a role in all areas of the phase diagram, and is probably as important as double exchange. The active distortion the Mn^{+3} ion imposes on its local environment amounts to an extremely strong electron-phonon interaction involving the $e_g - O2p$ conduction band and a LO phonon band. Oxygen isotope effects clearly indicate the importance of this coupling. A well-developed literature reports large isotope effects in practically every phase transition temperature throughout the range of doping. Guo-Meng *et al.*[43] observed a 20 K shift in the ferromagnetic T_c of LCMO-0.2, which corresponds to an isotope coefficient α of 0.85. The value of alpha decreases as the doping level increases, to 0.14 near the charge-order boundary.[44] The charge-ordering transition, by contrast, behaves in the opposite way: α = –0.41.[45] The heavier O^{18} atoms seem to enhance the tendency of manganites to form insulating phases. A vivid demonstration was provided by Babushkina *et al.*,[46] who suppressed the metallic state in $La_{0.175}Pr_{0.525}Ca_{0.3}MnO_3$ from 95 K to below 4.2 K by O^{18} substitution.

An early argument by Millis, Littlewood, and Shraiman[47] suggested that the Jahn-Teller effects are indeed responsible for what they described as the low values of T_c in all the ferromagnetic manganites. Although double exchange magnetism can be mapped to the Heisenberg Hamiltonian, the available magnetic data are not entirely consistent with

this interpretation. The critical exponents of LSMO have been carefully measured[48] to match the Heisenberg model. The magnon dispersions of several materials have been measured by neutron diffraction;[49] most also fit the Heisenberg model, at least for moderate q. But the critical temperature is far too low. The spin-wave stiffness K for $La_{0.67}Pb_{0.33}MnO_3$ (LPMO-0.33) is 45 meV. In the Heisenberg model for a cubic lattice, $T_c \approx 2.9K\frac{(S+1)}{S}$, where for the case of manganites $S = 1.5$. The critical temperature should be 0.2 eV or 2600 K, much larger than typically observed values of 1-300 K. Millis and his coworkers suggested that polarons arising from the Jahn-Teller distortion could reduce T_c. What is needed is an additional source of fluctuations or disorder to localize the carriers. A carrier hopping between sites of different valency in the double-exchange sense meets not only potentially a different spin, so that the band is split by exchange; but also certainly a different local atomic environment, either distorted or non-distorted. The Jahn-Teller effect splits the degenerate e_g orbitals; the magnitude of the split has been estimated at 0.6 eV.[50] This may be enough to suppress T_c by the required amount.

A hopping hole carries an atomic rearrangement with it, and therefore should be thought of as a polaron. A great amount of theoretical effort has been dedicated to this picture of polarons which interact by double exchange. Roder, Zang, and Bishop[51] discussed the effect of the additional interaction on T_c. The bandwidth of the polarons is narrower than the bandwidth of double exchange carriers by a factor $\exp(-\varepsilon\gamma^2/h\omega)$, where $\varepsilon\gamma^2$ is an interaction strength; and T_c is reduced similarly. Since $\omega \propto M^{-1/2}$, the

isotope exponent $\alpha = \frac{1}{2}\frac{\varepsilon\gamma^2}{\hbar\omega}$. Using the value of Guomeng *et al.* of 0.85, we have a reduction factor of 5.5. This comes reasonably close to explaining the discrepancy between the Heisenberg $T_c \sim 2000$ K and the measured LSMO-0.15 T_c of 200 K.

The resulting picture is rather complicated. The high-temperature insulating state is relatively easy to understand: the narrow-bandwidth electrons are localized in the background of fluctuating spins and atoms. The low-temperature model must now include not only the half-metallic density of states of delocalized holes but also their affiliated delocalized Jahn-Teller distortions. Do the delocalized holes participate in the Jahn-Teller effect at all? Several attempts have explored the low-temperature dynamic structure. Booth *et al.*[52,53] studied the X-ray absorption fine structure (XAFS) of LCMO above and below T_c. Because they lacked the resolution to distinguish the different lengths of Mn-O bonds, the high-temperature static Jahn-Teller distortion appeared as an anomalously broad peak in the XAFS Fourier transform. This peak narrowed significantly across the ferromagnetic transition. Other authors have calculated pair distribution functions with higher resolution from neutron scattering[54] and XAFS.[55] The high-temperature distortion, with three Mn-O bond lengths of 0.213 nm, 0.201 nm, and 0.191 nm that correspond to the interlocking cooperative structure, disappears at low temperature. At low temperature there is still a distortion, however, featuring two more similar bond lengths of 0.201 nm and 0.191 nm. (The bond length of undistorted LCMO is 0.190 nm.) The low-temperature distortion has been interpreted as a large polaron, in which the strain is spread over a volume comparable to the hole's radius.

The notion of delocalized polarons in CMR manganites has been used to explain several puzzles. For example, the unusual zone-boundary softening[57] observed in the magnon dispersion has been attributed to magnon-phonon interactions.[56] The failure of Kubo and Ohata's original prediction for the temperature dependence of the resistivity has been resolved by two subsitute scattering mechanisms: two-magnon processes due to the half-metallicity and polaron relaxation.[58] Most enticingly, the gap observed in the tunneling spectroscopy data of Wei *et al.*[33] has been explained as a pseudogap caused by the formation of polarons.[59]

CHAPTER 2

Synthesis of manganites

Motivation

The CMR manganites differ from other perovskite oxides in two important respects. First, the bandwidth results from double exchange, instead of superexchange. Second, the phonon interaction is much stronger than in many other materials. This second fact has led to the suggestion that manganites may, in certain regimes, be good superconductors.[60] Similarities that encourage this idea include the possible observation of a pseudogap and the fragile antiferromagnetic metal that has been seen near $x = 0.5$.[61]

The stability of the low-temperature metallic phase of colossal magnetoresistance manganites is determined by the electronic bandwidth in competition with the cation disorder potential, the exchange splitting, the Jahn-Teller coupling, and the on-site Hubbard repulsion. The phases reached when some of these interactions dominate have been discussed in the previous chapter. The most sensitive parameter with which to tune the interactions is bandwidth, and the most effective method with which to tune the bandwidth is the application of pressure.

A number of researchers have studied the effects of small amounts of hydrostatic pressure (P<20 kbar) in various manganite materials. The general result is that T_c increases at a rate of 2-3 K/kbar[62] due to increased bandwidth. As the lattice contracts, greater overlap between Mn and O orbitals leads to more hybridization and an increased hopping integral

t. The observation by Argyriou *et al.*[63] of exchange-induced striction in $La_{1-x}Sr_xMnO_7$ raises an interesting additional possibility. As pressure increases the overlap, the double-exchange term increases proportionate to t. The superexchange, although smaller at zero pressure, increases as t^2. At high enough pressures, a strong overlap may result in super-exchange-induced bandwidth. The material should then be an antiferromagnetic metal and potentially a superconductor. High pressure has been used to search for this state.

The importance of pressure that is hydrostatic comes from the sensitivity of the manganites to anisotropic stress. As discussed in the last chapter, insulating ground states of manganites that are both lightly doped and highly doped feature orbital order in cooperation with the static, long-range Jahn-Teller distortion. The orthorhombic distortion is favored by applied uniaxial strains. The most evidence has come from studies of thin film behavior which have compared the transport of films of different thicknesses[64] or epitaxial films on different substrates.[65] The transport properties of films have also been correlated directly the strain by structural measurements.[66] To minimize this effect, it is important to use hydrostatic pressure; the means by which this was achieved are discussed in the next chapter.

A second important consideration is that samples should not be polycrystalline. Many workers have shown that the magnetoresistance properties of powder samples are dominated by spin-dependent tunneling between the grains.[67,68] Mathur *et al.*[69] explicitly measured the magnetoresistance due to a single grain boundary and were able to explain much of the low-field behavior of bulk samples from their data. In the environment of a

high-pressure cell, granular samples are likely to be particularly fragile as the pressure-transmitting fluid forces its way into cracks and fills any voids. Grains which experience slightly different pressures may remain on the ferromagnetic side of any sensitive transition, making superconductivity difficult to observe clearly.

Bulk crystals of $La_{1-x}Pb_xMnO_3$ and $Nd_{1-x}Pb_xMnO_3$

Single crystals of $Nd_{1-x}Pb_xMnO_3$ (NPMO-x) were synthesized according to the flux-growth method of Morrish *et al.*[70,71] Powders of Nd_2O_3, PbO, and MnO_2 in the desired molar ratios were mixed with a flux comprising 1/3 PbO and 2/3 PbF_2 by mass. The ratio of flux to powder was 4.56:1 by mass. These powders were ground in a mortar and pestle for five minutes. The mixture was transferred to a platinum crucible, over which a loose platinum lid was fitted. The platinum crucible was placed in a lidded alumina crucible, which was placed in a Lindberg box oven open to the air. The reaction proceeded by heating the materials quickly to 1450°C. After reacting at 1450°C for 16 hours, they were cooled to 800°C at a slow rate of 1.5°C per hour. At this temperature the crystals had formed, and the oven was turned off to produce a quick cooldown to room temperature.

Black, shiny, rectangular crystals were then found in the bottom of the platinum crucible. The size of these crystals varied with cooling rate, with the concentration of the flux, and also with the mixing stoichiometries of the powders. For some runs an excess of PbO was added. After these runs there were droplets of a light red, translucent solid mixed among the crystals, which was probably excess PbO. The crystals were pried away from the crucible with tweezers. Sometimes a layer of hard, black deposit remained on the bot-

tom of the crucible together with crystals too small to be pried up intact. This material could be removed by first boiling the crucibles in concentrated sulfuric acid and then sonicating them in concentrated hydrochloric acid.

The crystals were characterized by energy-dispersive X-ray spectroscopy at the Electron Probe Microanalysis facility in the Department of Geology. As X-ray absorption standards $NdPO_4$, PbO, and MnO_2 were used. The crystals had voids and channels as wide as ten microns and as long as hundreds of microns. The stoichiometry of the crystals was found to be extremely uniform at $x = 0.17 \pm 0.02$. This represents a significant deviation from the most commonly attempted stoichiometry of $x = 0.4$. One possible cause of this discrepancy might be evaporation of lead from the crucible. However, a number of runs left excess lead oxide frozen in droplets amidst the crystals. It seems unlikely that there was insufficient lead to incorporate in the crystals. The $x = 0.17$ stoichiometry seems to be particularly stable. Several crystals that had been synthesized by Jia and Khazeni were also tested; their compositions were similar.

Resistance measurements provide an important verification of these results. Samples were selected at random from batches with incorrect stoichiometries. The resistances of these samples were measured as a function of temperature with a standard four-probe technique. Gold wires were attached using silver paint or silver epoxy, and the two-wire resistances were generally not more than twice the four-wire resistances. Measured resistivities were approximately 10KΩcm. All these samples showed insulating behavior with temperature; no insulator-metal transitions were observed. This confirms the EDX result that the samples were insufficiently doped to reach the ferromagnetic metallic phase.

Epitaxial films of LCMO-x

Single-crystal films of LCMO-x were also synthesized. First, powders of LCMO-x were made by solid-state reaction. Powders of La_2O_3, $CaCO_3$, and MnO_2 with La:Ca:Mn ratios of 2:1:3 were ground in a mortar and pestle. The material was calcined at 1250°C in air for 5 hours. After regrinding, it was heated to 1380°C and reacted for 12 hours in air. After a third grinding, the material was reacted at 1390°C for 20 hours in air. Finally, the powders were ground again. They were pressed into 1/4" diameter, 1/2" long pellets in

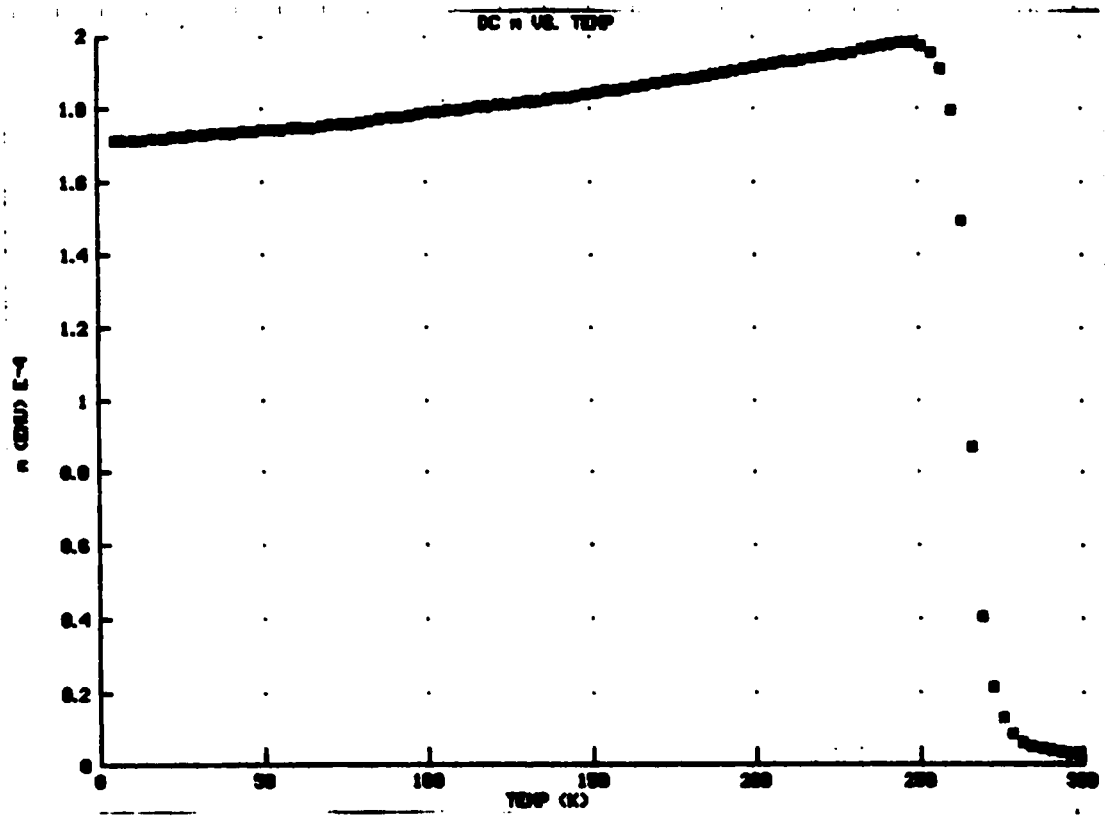

Figure 1. Spontaneous magnetization of the LCMO-0.33 powders, showing T_c=260 K

a steel die at a pressure of 14 kbar. The resulting pellets were hard and dense. X-ray diffraction and magnetization measurements confirmed that they contained single-phase LCMO-x.

Epitaxial films were grown on $LaAlO_3$ (100) substrates by pulsed laser deposition.[72] The PLD facility in the Integrated Materials Laboratory at UC-Berkeley features a 248 nm KrF excimer laser focused to a spot 3.5 mm in diameter. The LCMO pellets were mounted as targets for the laser and were illuminated with 3 J/cm2 pulses at a repetition rate of 10 Hz. Substrates were attached to a heater block using silver paint and were maintained at 700°C throughout the growth. Before ablation, the chamber was evacuated by a cryopump to 2×10^{-6} torr and then filled with 200 mtorr of oxygen. During the synthesis oxygen continued to flow at 75 sccm. Typically several thousand pulses were used to grow films of tens of nanometers in thickness.

The details of transport measurements under high pressure are described in the next chapter.

Figure 2 shows the high-temperature data from a typical experiment. The resistance of these materials decreases steadily as the pressure is increased. The insulator-metal transition temperature continues to increase as it does at low pressure, rapidly leaving the temperature range accessible to a diamond anvil cell.

In successful experiments in $La_{0.67}Pb_{0.33}MnO_3$ and $Nd_{0.6}Pb_{0.4}MnO_3$ at pressures up to 150 kbar, no superconductivity was found above 2.2 K.

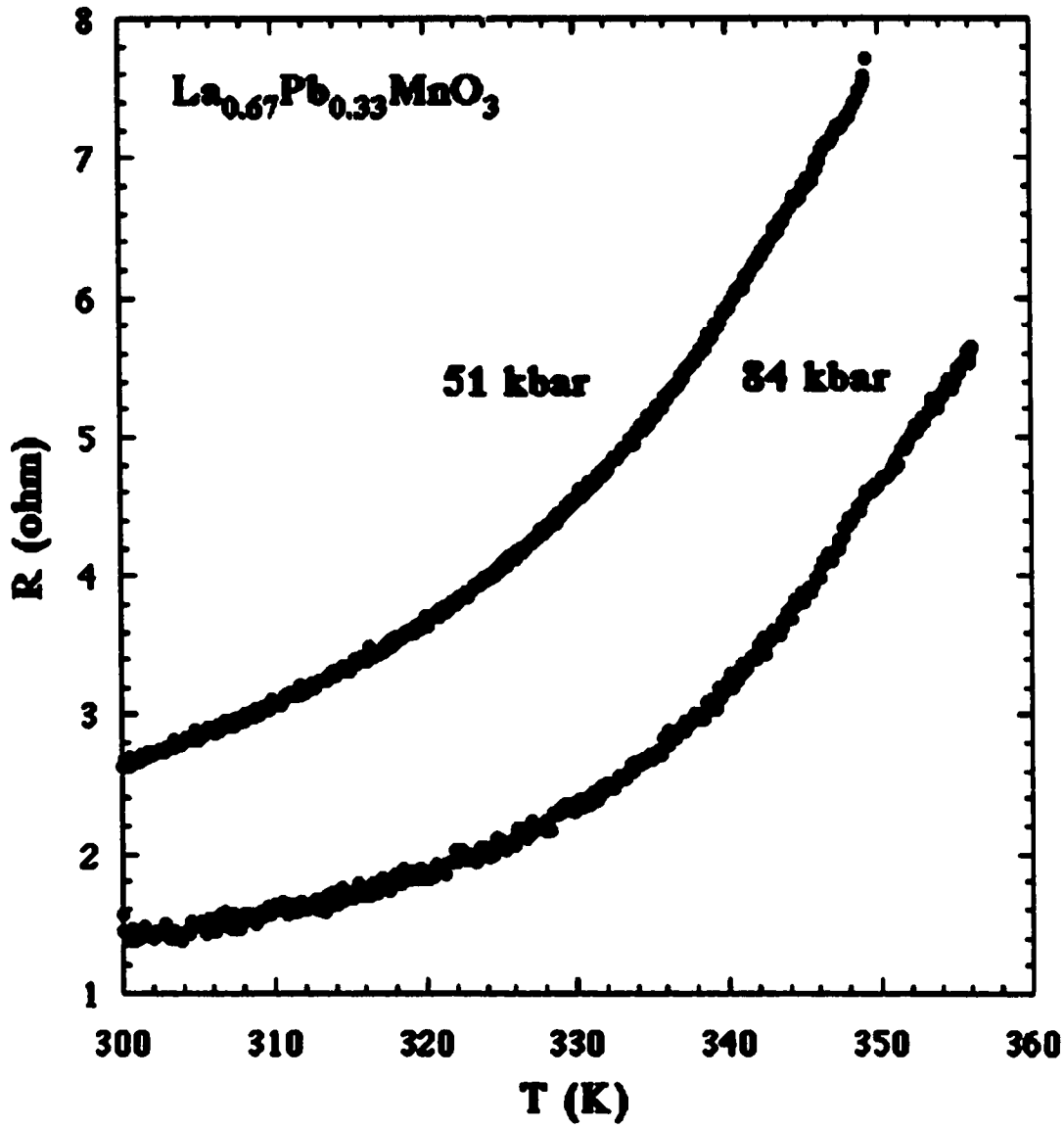

Figure 2. The high temperature, high pressure resistance of a manganite sample.

CHAPTER 3

Diamond Anvil Cell Techniques

In this chapter are described the methods by which high hydrostatic pressure is generated and maintained and samples are mounted for resistance measurements under pressure.

Introduction

Varying the thermodynamic quantity of pressure can reveal exciting new physics, as solids undergo phase transitions and modified densities. In solid water, for example, the known diagram includes twelve distinct phases produced by the delicate nature of hydrogen bonding. Pressure is potentially as useful a variable as temperature, but the difficulty of high-pressure experiments has tended to obscure this potential. The thermodynamic conditions in which we live include a high mean temperature and a low mean pressure. For almost all solid materials, the temperature of 300 K is within an order of magnitude of a phase transition such as melting. The pressure of 1 bar (0.1 MPa), though, is negligible by comparison to solid-solid phase transitions and to bulk moduli. Compared to the moduli of most solid materials, atmospheric pressure is negligible.

The properties of materials under high pressures have consequently only begun to be investigated. The pioneering work by Bridgman[73] using tungsten carbide anvils demonstrated the feasibility of solid-state phase diagram explorations. These apparatuses suf-

fered from the difficulty of optical access as well as from fundamental limits on the achievable pressures.

The development of the diamond anvil cell (DAC) by Sam Weir in the 1960's eliminated both obstacles at the same time. Because diamonds are transparent, the DAC proved to be ideal for optical measurements, including spectroscopy and x-ray diffraction studies. Extraordinary pressures can be achieved because of the high modulus and strength of diamond. The fundamental limit placed by that strength is not known. Clark *et al.*[74] suggested that it lies at 5 Mbar, just beyond the current record pressure of 4.6 Mbar.[75] Certainly it is not uncommon for today's well-designed pressure cells to reach 2 Mbar.

The disadvantages of the diamond anvil cell have always been the small sample volume and the difficulty of traditional solid-state measurements. A battery of techniques will be required to understand new physics at high-pressures. Magnetic susceptibility is the most advanced,[76] and has primarily been used to observe superconducting transitions.[77] Recently attention has turned to the development of nuclear magnetic resonance at high pressure.[78] Transport experiments, despite their ubiquity in zero-pressure physics, have remained uncommon.

Several challenges have to be faced to measure resistance under pressure. Electrical leads must be insulated from the typically metallic gaskets. Tozer[79] was unable to insulate wires from gaskets at pressures above 100 kbar. The method of Catledge *et al.*,[80] in which the leads are coated with epitaxial diamond films, is too expensive and time-consuming for widespread use. Sample contact is an additional problem. Peter Yu's group[81] relied on

highly non-hydrostatic pressure to push wires into their sample. This method has been pushed to observe a superconducting phase in CsI at 2.2 Mbar.[82]

For materials like the manganites, in which stress is significant, non-hydrostatic pressures are unacceptable. To carry out the experiments discussed in the previous chapter, a set of techniques was developed to measure resistance under hydrostatic pressure. In this chapter will be described the apparatus used to generate high hydrostatic pressure and mount samples for resistance measurements.

Design of the DAC

The catalog of diamond anvil cell designs has been reviewed by Jayaraman[83] and by Eremets.[84] Figure 1 diagrams the cell used in the Zettl labs. The cell contained three components: the diamond anvils themselves, a mechanism for aligning them securely, and a means to maintain the pressure. High pressure was achieved by amplification of force. The anvils distributed the force required to produce high pressure in the small area of the culets into a larger area of weaker material, and thence into the bulk of the pressure cell. At the highest pressures there was still considerable pressure in the bulk of the pressure cell, so that it was important to use extremely strong materials. Since the DAC described here was used to search for superconductivity, it was made out of beryllium copper, a strong non-magnetic alloy.

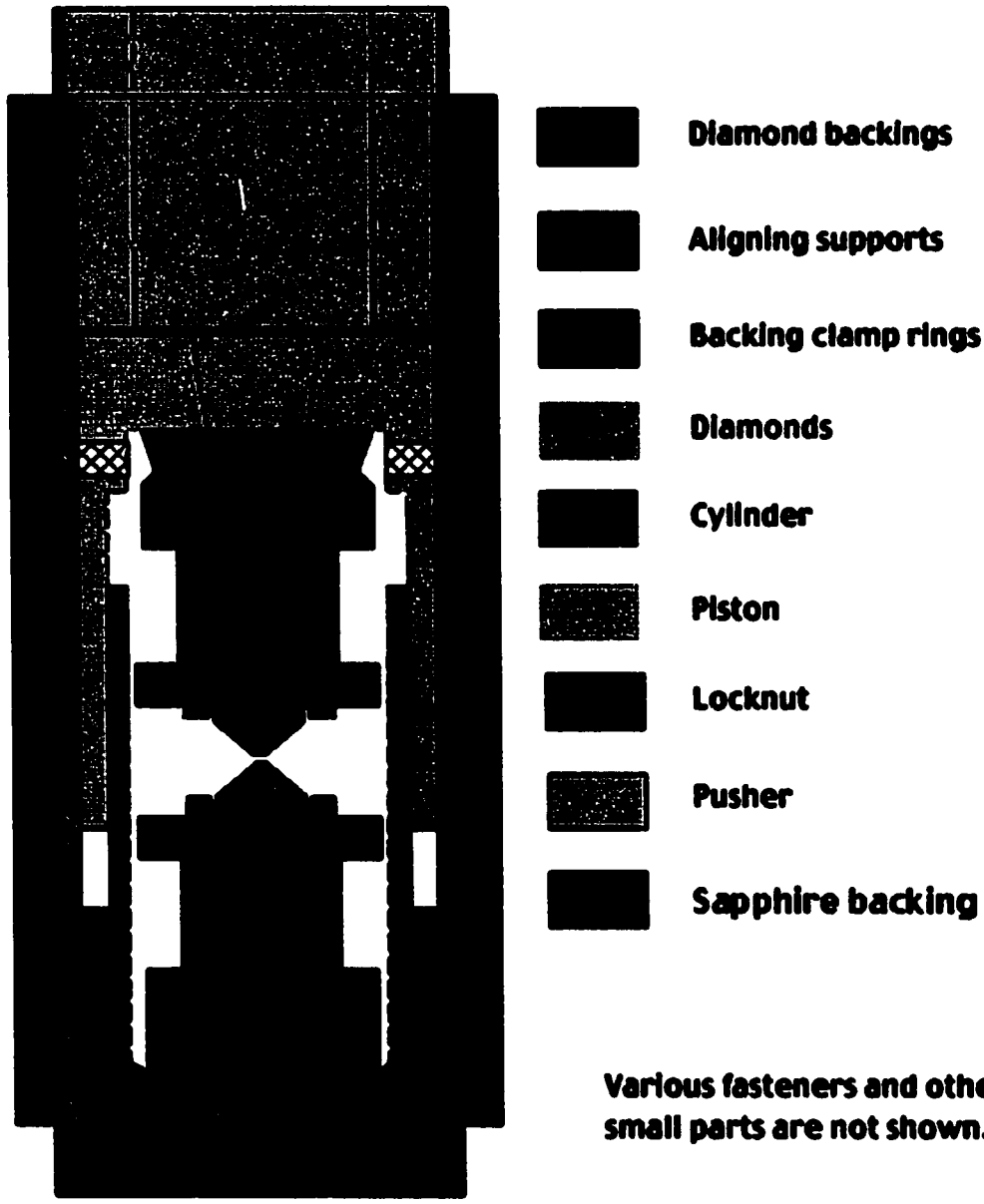

Figure 1. Diagram of the 800 kbar diamond anvil cell

The DAC in the Zettl labs was intended to reach 800 kbar, which is the boundary above which diamonds must be recut after each pressurization.[85] The design pressure of 1 Mbar allows some margin of error for actually reaching 800 kbar. The available pressure was directly determined by the size of the culet and table of the diamond. Smaller culets would allow higher pressures at the cost of smaller sample volumes. After extensive experimentation with sample mounting, culets 450 microns in diameter were chosen to be the smallest practical. The cut of the diamonds, shown in Fig. 2, was designed to maximize the table-culet ratio with respect to the mass of the uncut diamonds. (Diamonds that could produce larger tables were too rare and expensive.) The diamonds were cut to order from low-fluorescence Type Ia octahedral crystals, and massed 0.3 carat each.

Pressure distributions during indentation can be calculated from the theory of elasticity;[84] the peak pressure at the center of an indenter is generally three times larger than the

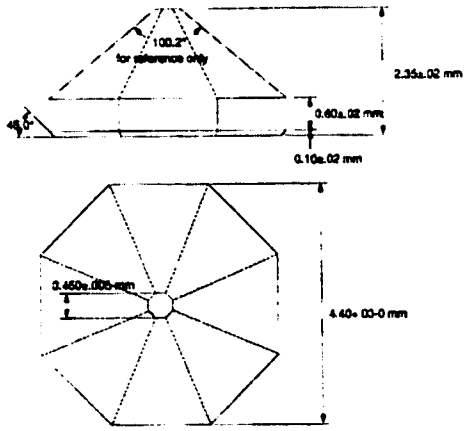

Figure 2. Design of the anvils used in the 800 kbar DAC.

average pressure. To reach a pressure of 1 Mbar at the center of the specified culet, a force of 1250 lbs would be required. The peak pressure at the table of the diamond would then be 10 kbar, which is near the yield strength of beryllium copper. To distribute this stress from the table of the diamond into a larger area of the relatively soft metal, a single crystal of sapphire was inserted as an intermediate backing. Although sapphire is clear, it contains chromium impurities with the same fluorescence spectra as the chromium in rubies. The quantity of chromium in the path of the excitation laser in the 1/8" thick sapphire was large enough to obscure the fluorescence peaks from the small chips in the high-pressure volume. Conical holes were drilled in the sapphires with diamond drills on a high-speed lathe. At the sharp corners of the diamonds dangerous stresses could be concentrated which could crack the sapphires. To mitigate this danger the sapphire backings were coated with a 1 micron evaporated film of soft indium. Diamonds pressing into the indium plastically deformed it to smooth the pressure distribution.

Figure 3. The diamond backings mounted in their seats. The left seat is the hemispherical rocker, and the right seat is used for lateral alignment.

The diamonds were held in place by a four-tongued clamping ring made of springy BeCu foil. Each diamond, on top of a sapphire disk, was clamped to a cylindrical BeCu seat. These seats were in turn clamped to the body of the pressure cell alignment mechanisms, shown in Fig. 3. These mechanisms were capable of aligning the diamonds in three respects: lateral positioning, rotation, and angular alignment. Lateral and rotational alignments were achieved by moving the diamond in the cylinder, while angular alignment was achieved by moving the diamond in the piston. The cylinder diamond seat was clamped to a disk with an angled groove around its bottom. Three set screws in the cylinder could be loosened or tightened to move the disk laterally while keeping it firmly clamped to the cylinder. Meanwhile, the clamping ring could be loosened to permit the diamond seat to be

rotated in the disk until it aligns with the piston diamond. This diamond seat rested in a backing with a hemispherical base. The hemispherical seat rotated in a matching hemispherical cavity in the cylinder centered on the culet of the diamond. Long screws fastening the clamping ring could be loosened or tightened to adjust the angle of the diamond. To preserve these alignments, the piston was made to fit tightly into the cylinder. The two matching faces were ground after the cell was age-hardened. A pin in the cylinder and matching slot in the piston ensured that the rotational alignment was preserved.

The pressure containment roughly followed the Mao-Bell design, with the force was applied uniformly along the axis by a pusher. Because the cell was required to fit in the bore of the Zettl labs' 1.5" superconducting magnet, it was not possible to use the lever/scissors arrangement of the ordinary Mao-Bell diamond anvil cell. Instead, the piston base was threaded to receive a locknut that pushes down on the cylinder. An earlier version of this design featured a 20-pitch thread, but it was found that at pressures above 300 kbar, the rotation needed to produce small increments of pressure was impracticably small. The current design incorporated a threaded pusher on the other side of the cylinder. In Fig. 4 the pusher has been turned a few threads into the locknut. Holes in the pusher, the cylinder, and the locknut allowed the pusher to be locked to either the cylinder or the locknut by the insertion of small BeCu pins. At low pressures, when the amount of turning required to increase the pressure was quite large, the pusher was locked to the locknut, so that the locknut/pusher assembly moved in over 27 threads per inch. At roughly 150 kbar, the pusher had rotated so that its holes lined up with those in the cylinder. These were locked together and the pusher was released from the cylinder. Now, as the locknut

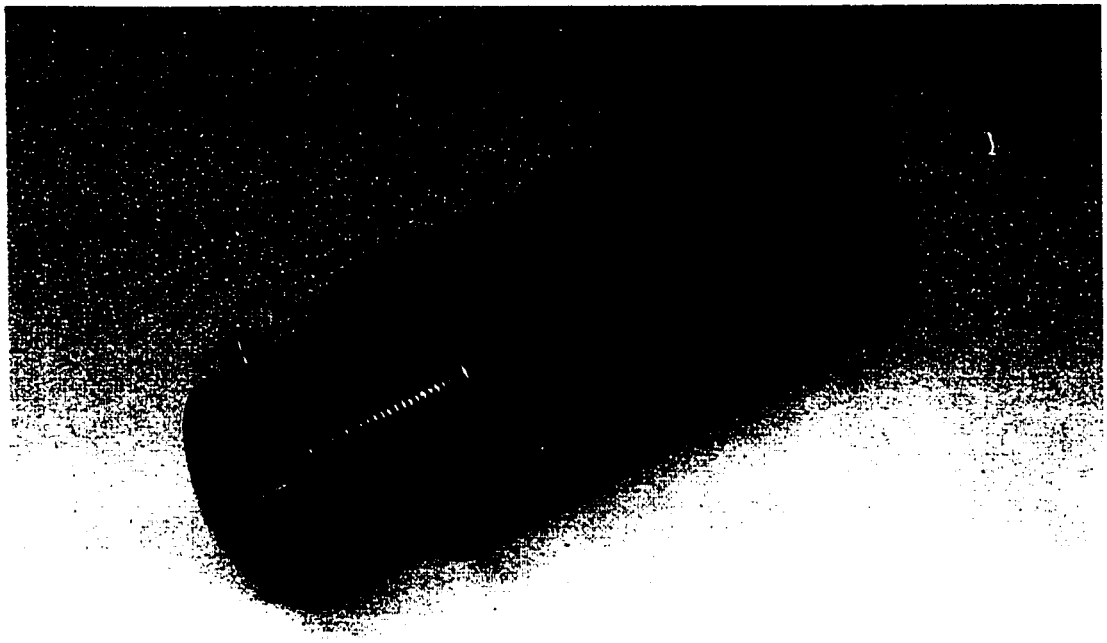

Figure 4. Locknut and pusher. The two different kinds of locking pins can be seen in the pusher.

rotated, the pusher moved in over an effective pitch of 756, providing fine control over the pressure.

Several additional holes in the pressure cell allowed the introduction of accessories necessary for the experiments. Both clamping rings had threaded holes for mounting a gasket. Both sides of the pressure cell also had holes through which wires could be fed for the resistance measurements. These wires passed through Teflon tubes stuck in grooves cut in the diamond seats and held in place by the four-tongued rings. They were then

Figure 5. Piston and cylinder inside views. The four-tongued rings can be seen clamping the diamonds. The gray surface beneath the diamonds is the indium coating on the sapphire backings.

glued to the diamonds with MS907 epoxy. Additional holes allowed tubes to be inserted to conduct cryogenic pressure fluid directly to the sample volume.

The pressure was measured by the ruby fluorescence technique[86,87] using a CVI Digikrom 480 spectrometer. The pressure cell was mounted in a special holder in the sample area of an Olympus BX60 microscope. To focus on the rubies with objectives located outside the height of the pressure cell, a converging lens was mounted in a small adjust-

able lens holder in the space above the cylinder. This brought the image of the sample volume to within the working distance of the microscope at the cost of some demagnification.

Preparation of experiments

Gaskets were made in batches of aged BeCu 25. Metal strip of 0.10" thickness was heat treated according to the Brush-Wellman recipe.[88] This metal was tested to have reached a hardness of 40 on the Rockwell C scale. Holes were drilled using tungsten carbide drills and a specially made die with holes to match the mounting holes. The gaskets were then cut and filed to fit inside the cell.

First the diamonds were cleaned with cotton-tipped swabs. A small amount of acetone was sprayed on a swab, with whiich the pavilion or culet off a diamond was brushed. After all the surfaces were wiped until no contanimation was visible, the procedure was repeated with ethanol-soaked swabs.

Before every experiment the pressure cell was aligned. The pressure cell was assembled without a gasket between the diamonds. When the diamonds were about 10 microns apart it was easy to determine whether the lateral or rotational alignment needed to be adjusted. When these alignments were acceptable the diamonds were pushed to within 1 micron while being observed under high magnification in transmitted light. When the diamonds approached within 1 micron of each other, colored interference fringes could be seen.. The angular misalignment of the diamonds appeared as a pattern of fringes and could be corrected using the hemispherical rocker. After several iterations of lateral, rotational, and angular alignment, the diamonds were aligned within 0.1° of being parallel.

At this point there were no fringes, and as the diamonds were pushed together, the culet flashed a series of uniform colors. The alignment tended to change very little during an experiment. The alignment was never adjusted during the preparation of an experiment, so as to avoid destroying the brittle gaskets.

A gasket had next to be preindented. This process work-hardened the metal so that it was much stronger in the vicinity of the pressure area. In addition, the pre-indentation produced octagonal dents in the gasket that caused it to align itself readily during subsequent assembly. Any stress in the gasket before indentation would cause it to misalign when it was remounted later in the process. The gasket was mounted to one of the clamping rings with three brass screws. The screws were tightened so that the gasket was level in the cell, as ascertained by eye, and held with a small ability to move freely. The cell was assembled and transferred to the small press. This press was marked to allow recording of the point at which the pusher began to push the diamonds into the gasket, and to identify wher the diamonds were in contact. To indent gaskets for electrical transport experiments the diamonds were pushed against the gasket almost to contact. When the cell was disassembled, the gasket had a deep octagonal indentation in each side and a circular ridge of material that had flowed out of the hole.

Insulating gaskets

The material in the flat part of the gasket had to be completely removed to prevent electrical contact. The gasket was mounted in a 1/2" Cajon quick-disconnect vacuum fitting between the washer and the nut. This assembly could be mounted in the vise of a miniature drill press, which was itself mounted in a three-axis micromanipulator. With a

tungsten carbide spiral drill, a hole nearly 2/3 the diameter of the culet was drilled in the center of the flat part of the indentation. This hole had large burrs on both sides. The drill was used to mill the hole until it was only 20 microns smaller than the culet. This process removed the burr from the top side. The gasket was then turned over and the burr on the other side was milled away. After this machining, during which WD40 was used for coolant, the gasket was cleaned by sonicating it in solvents.

These details of the gasket shaping were important. If the hole in the metal was too large, the insulating composite did not form well. If the hole was too small or the edges were rough, the wires would make contact to the metal through the insulator. Figure 6 indicates the ideal situation: the beryllium copper acted only as a holder for the insulating gasket.

The gasket was then remounted on the diamond. The insulating gasket composite was mixed from hard insulating powder and soft epoxy. At first alumina powder of 0.3 micron size was used, and this worked well. Following a suggestion by Reinhardt Buehler,[89] diamond powder of 0.1 micron size was also used. The diamond powder produced a harder gasket that withstood higher pressures. There was an increased risk of damaging the anvils with the small, hard diamond grains, but no damage was observed. The epoxy was Miller-Stephenson 907 epoxy. This epoxy was found to have convenient viscosity and curing properties. Stycast 1266, by contrast, was much less viscous before curing and harder when cured, so that the gasket was excessively brittle.

The insulating gasket was constructed in such a way that it could be removed undamaged from the diamond anvil cell for drilling. The best way was found to be as follows.

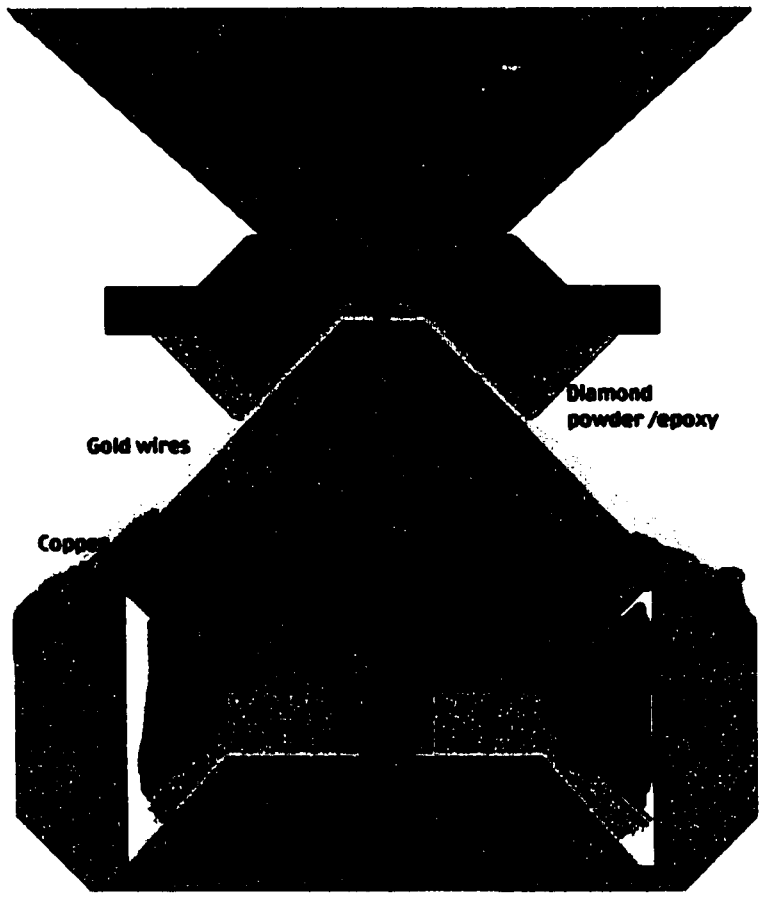

Figure 6. Sketch of the sample volume, showing the placement of the ruby pressure gauge and the wired sample within an insulating gasket.

The epoxy was mixed by combining a small drop of epoxy on a glass slide with a larger quantity of insulating powder. As necessary, more epoxy or more powder was added with a wooden stick. The desired consistency was a mixture that was dry to the appearance but noticeably cohesive and springy. The piston diamond was cleaned thoroughly. Then a small amount of composite on a sharpened wooden stick was applied within the indentation in the gasket. The cell was assembled and compressed gently by hand. When the cell was disassembled, some composite occasionally remained on the piston diamond. To

minimize this, the piston and cylinder were rotated slightly with respect to one another before disassembly. Any excess composite stuck on the piston diamond was removed. Large pieces could be removed with a wooden stick and added to the gasket. Smaller pieces were removed by a soaked cotton swab. More composite was added to the gasket, and the process was repeated.

After several iterations, the composite in the gasket had formed a cohesive mass, and it was then formed into the correct shape and air bubbles were eliminated. More material with a different method of compression consisting of an alternation between gentle hand compression and firm compression in the mechanical press. The gasket could be thinned significantly by very little pressure, because the epoxy was not set yet. The compression was controlled by distance, working first until the gasket was 80 microns thick, then 150, then 250. During this phase it was detrimental to rotate the piston and cylinder before separation. Some material remained on the piston diamond; this material was removed, the diamonds were cleaned, and the process was repeated. Finally the point was reached when the gasket had been compressed in the press to 250 microns, and the diamond had come away quite clean. The next-to-last step was to dismount the gasket and clean any residue from the cylinder diamond. This process ensured that the cured gasket did not stick to the diamond. However, a few pieces occasionally broke off from the gasket at that point. The gasket was remounted, material was added, and the cell was compressed again until the thickness was 250 microns.

Composite that flowed out of the indentation formed a wall extending above the sides of the indentation. This wall was destroyed with a sharpened wooden stick so that the

hard, cured wall would not damage the wires. Finally, to seal the composite edges and insure that the entire gasket was insulated, pure epoxy was painted on the metal part of the gasket and just over the edges of the composite. After this the gasket was cured on the diamond.

The sample volume

After the gasket is cured, it was removed it from the cylinder diamond intact. A small hole to form the sample volume was drilled using a National Jet diamond vee-drill. The construction of this drill guaranteed that the center of the drill bit's cutting surface coincided with the center of its rotation. The separation of the motor from the drill also minimized vibration. The combination of these features allowed me to drill 50 micron holes precisely. The drill bits themselves were spade drills ground to order by the National Jet company. The material of the drills, tungsten carbide, was hard enough to drill through the diamond/epoxy composite when the drill had been freshly sharpened. Each bit could only be used for this process once before being sent back to the company for resharpening.

Newport micromanipulators were attached to the drill's workpiece mount. A small, steel gasket mount on top had three holes to match the mounting holes in the gasket. In the center of the mount awas a 1/16" hole which accepted a small brass cylinder.. Each disposable cylinder consisted of a section to fit in the hole and a post which fit snugly inside the gasket indentation. The height was chosen to match that of the diamond. When the gasket was mounted on this steel piece as it would be in the pressure cell, the brittle insulating gasket was supported by the brass post as it would be by the diamond.

The drill was centered in the gasket indentation by eye through a microscope. The construction of the drill allowed hand control of the drill stopping point to within less than 1 micron. The hole was drilled gently at a speed of 1 micron per second, using distilled water as the coolant. Because of the support from the brass post, the bottom side of the gasket did not fracture or burr, and the drill cut through to the brass cleanly. The gasket was not sonicated afterwards, as the composite was brittle and fragile. Soaking in isopropanol removed the remaining water.

The next step was to scatter ruby particles on the diamond underneath the gasket. In addition to providing the pressure gauges, the ruby also increased the friction between the gasket and the diamond, helping it to contain the pressure. The ruby was prepared once each year by crushing a ruby ball in an agate mortar and pestle. After it was ground into a fine powder, the powder was mixed with isopropanol in a sealed vial by sonication. The smaller grains stayed suspended for a few hours, while the larger grains fell out. After half an hour, the liquid was decanted, into a new vial. In preparing an experiment, the powder was remixed into the liquid and allowed to settle for ten minutes to separate the largest grains. A drop of this suspension on a thin copper wire was allowed to evaporate until its diameter was slightly smaller than the culet size. This concentrated suspension was transferred to the culet of the diamond, with no liquid allowed to flow over onto the pavilion. The resulting ruby particles were typically 1-2 microns across, and they were densely scattered on the culet.

The gasket (with sample attached, as discussed below) could not be mounted directly on the diamond. It was necessary to provide a seal that functioned at low pressures to con-

tain the pressure fluid before compression. The gasket was glued to the diamond with five-minute epoxy. The film of epoxy covered the pavilion and a thin ring around the circumference of the culet. The choice of glue was important. Miller-Stephenson 907 was too viscous to be spread as a thin film on the culet. When the weight of the gasket settled down on the glue, the MS907 extruded into the hole, obscuring the rubies.

At this point the cylinder diamond was ready.

Sample Preparation

Polishing and thinning

Samples for the diamond anvil cell were thin, small platelets with smooth clean surfaces and four wires strongly attached. The details of the sample preparation were found to affect the efficiency and reliability of measurements significantly. This section will describe means by which such samples were prepared from bulk crystals.

Some materials, including layered perovskite superconductors and quasi-one-dimensional charge density wave conductors, can easily be cleaved to produce flat surfaces. Preparing thin samples of these materials was as simple as gluing one side to a slide and removing layer after layer with tape.

Most materials, including cubic perovskite manganites and silicon, do not cleave, and must be polished thin. The apparatus assembled and constructed in the Zettl labs allowed the preparation of few-micron-thick samples with areas of square millimeters. There were four diamond-impregnated lapping plates with successively finer grits ending in

3000 grit and diamond polishing pastes beginning at 3000 grit and ending at 0.1 micron. A custom-machined manual jig and sample mount maintained the flatness of the sample.

To polish a sample, the crystal was glued to a flat silicon chip with a very thin film of superglue. The silicon chip was glued to the brass rod with mounting wax. The brass rod was pushed into the polishing jig, and the pair were placed face down onto the polishing surface. For the coarse polishing, the surface was a lapping plate coated with lapping oil. For the fine polishing, the surface was a piece of dry clean glossy photo paper with a dot of polishing paste on the back side. This dry clean photo paper was placed glossy side down on a dry clean granite block.[90] The sample was polished by rubbing the jig on the polishing surface in a figure-eight motion.

A complete polishing sequence began with a coarse plate and moved successively through the plates and the pastes. The sample was polished with a plate or a paste until the desired thickness had been removed. If the goal was simply a smooth surface, the crystal was polished with a given particle size until several particle diameters' worth of thickness had been removed. When the goal was to thin the sample, the crystal was polished with a given particle size as long as enough thickness remained to be able to polish it smooth with the following particle sizes.

The sample thickness was measured using two techniques. A dial indicator with 0.0001" divisions was mounted on a granite plate at such a height that its tip was just below the top of the brass rod placed on the granite plate. The reading of the dial indicator was precise to within one micron as long as the thermal expansion of the brass rod was taken into account. However, the thickness of the film holding the sample introduced

some error to the measurement. In addition the fine focus knob on the large microscope was calibrated with respect to this dial indicator to move the microscope stage 5.7 micron per knurl or 102 microns per revolution. The film of glue could be observed in the microscope, so the error due to its thickness could be eliminated.

The sample preparation proceeded as follows. The sample was polished or cleaved to produce a flat surface. This surface was coated with electron resist and patterned using the JEOL 6400 and NPGS in the Microlab with an array of squares. After the exposed resist was developed, the surface was cleaned by appropriate methods. For example, silicon would be cleaned with HF to remove its native oxide; blue bronze or manganites would be ion milled to remove any damaged layers. Immediately after cleaning contact electrodes were deposited. The resist and metal film were lifted off in acetone. The samples were then polished to 5-10 microns thickness. After being removed from the polishing jig by acetone, they were rinsed several times with acetone and ethanol. The resulting samples were delicate, large, thin plates of material with arrays of cleanly deposited metal on one side. These plates could be cut into samples using a clean, oil-free razor blade. Before cutting, a sample had to be covered with liquid, preferably ethanol, so that the small pieces did not fly away from the cutting area. The samples took the form of small rectangles with large contact pads on each corner.

Attaching the wires

The wires were flattened, cut, and glued to the samples. The flattening was crucial, because round wires rolled as they were first pressed to the gasket, and this movement tore them from the sample. The wire began as 1/2-mil pure gold wire. The wire was cut to

5 mm lengths and cleaned by sonication. The wire was pressed flat with a pair of mirror-polished tungsten carbide disks and a tool-steel die in which they were mounted. At a force of 40,000 pounds, the wires had work-hardened and actually dented the tungsten carbide. The resulting wires were flattened into strips 50 microns wide and a few microns thick. Using a clean, oil-free razor blade, these wires were cut to have sharp tips with included angles of 20° – 30°. Sharper tips did not hold glue.

During the wiring procedure, the sample rested on a glass slide. A small drop of MS907 epoxy was deposited on the glass slide a few millimeters from the sample. A sharpened, flattened wire was taken from the tungsten carbide disc, and its blunt end was lowered into the glue. The wire was bent slightly at the middle, so that it tended naturally to rest with the sharpened tip pointing slightly up into the air. The wire was maneuvered with a clean, sharpened wooden stick so that its tip was positioned over a contact pad on the sample. The MS907 was cured on a hot plate for several hours. Silver epoxy (Epoxy Technology H20E) was painted onto the end of the gold wire. The paintbrush was a short length of 0.0001" gold-plated tungsten wire glued to a wooden stick. Then the gold wire, firmly attached at its back end, was gently pushed down onto the contact pad on the sample. With practice it was possible to push it down with just enough pressure to cause the epoxy to wet the sample but not flow freely. When the wire was released to spring back, it lifted the sample. The epoxy was then cured for several hours on a hot plate.

After the silver epoxy was cured, the wire was cut loose from the MS907 epoxy, leaving a sample-wire combination lying loose on the glass slide. The other three wires could

be added in sequence in the same way. The resulting bonds withstood the stresses encountered in the sample mounting and pressurizing processes.

Mounting the sample

The wired sample could be mounted either on the gasket or on the opposing diamond. It was particularly important that the sample was properly aligned with the hole; this was difficult to achieve when the sample was mounted on the diamond. Gasket mounting was therefore found to work best. The contact pads and the wire attachments faced the diamond, leaving the sample to hang into the hole, as in Fig. 6. The wire attachments were not strong enough to survive severe manipulations such as bending, the wires were cut so that the assembly was small enough to fit in the indentation. To make it easier to handle the sample, a piece of flattened wire was glued to one of the leads in such a way that it projected up perpendicular to the assembly. The sample was lowered onto the gasket so that the sample was in the hole and the wires rested on the gasket. Silver epoxy was painted onto the wires and the gasket to secure the wires on the gasket. For convenience these operations were all performed while the gasket was outside the pressure cell, mounted on a steel base or sitting on a slide. Once the epoxy was cured so that the wires were firmly attached to the gasket, the wire handle was removed.

A further modification had to be made to the gasket. Once the sample leads were attached, the gasket was no longer flat, so that it would not seal against the diamond and hold in the pressure fluid. It was necessary to supply some low pressure seal. For this purpose, as on the underside of the gasket, five-minute epoxy was best. A thin layer was

painted on the gasket to produce a ring that was of the same thickness as the leads and their glue. After this the gasket was mounted on the lower diamond.

To make contact between the sample leads and the wires mounted on the sides of the diamond, the four facets of the pavilion which have wires mounted on them were painted with silver paint. The silver paint extended just over onto the edge of the culet so that the pressure of the diamond against the gasket pressed the silver paint against the sample leads. Silver paint is sufficiently soft that it made good contact and immediately deformed without affecting the low-pressure seal against the pressure fluid.

Pressurizing the cell

The two pressure fluids used were glycerin and liquid nitrogen. Glycerin is a better pressure fluid at low pressures, but it solidifies at room temperature at about 150 kbar.[91] Liquid nitrogen must be loaded cryogenically and therefore could not be used below pressures of a few tens of kilobar, but does not solidify at room temperature until 750 kbar.

Glycerin loading was quite simple. A drop of glycerin on the end of a clean wire was transferred to the indentation in the gasket. This sometimes left an air bubble; the air bubble was punctured and more glycerin was added. Then the pressure cell was assembled and the locknut was tightened finger tight. For nitrogen loading, a tall press with steel legs was used. The cell was mounted in the press with a small gap between the diamond and the gasket and transferred to an insulated bath. The bath was slowly filled with liquid nitrogen. After the level reached the sample volume, the press was tightened until the dia-

mond had pushed ten microns into the gasket. The press and cell were removed from the bath and allowed to warm to room temperature. The locknut was tightened and the cell was removed from the press.

At this point the pressure in the cell was between 1 and 15 kbar. The cell was compressed gradually using the press and the locknut, while the pressure was measured periodically in the microscope/spectrometer, until the desired pressure was reached. Mounting the sample on a probe and measuring resistance versus temperature were done using the methods standard in the Zettl labs.

CHAPTER 4

Introduction to nanotube experiments

Carbon nanotubes were first discovered by Iijima *et al.*[92] in the soot from an arc discharge chamber. This discovery led to an explosion of research into novel nano-structured materials, including metal and metal-oxide nanowires,[93] non-carbon nanotubes,[94] and filled nanotubes.[95] Carbon nanotubes retain a special interest because of their unique properties. From the strong covalent bonding of graphene they derive great strength, with moduli of 1 TPa.[96] From the peculiar electronic structure of graphene they derive a diversity of electronic properties including both metallic and semiconducting behaviors. From the strong bonding and stability of graphite they inherit a resistance to defects[97] that makes them among the cleanest of molecular wires. Single-walled nanotubes, the focus of this study, are perhaps the closest to one-dimensional behavior that humans have yet observed.

The rolling-up of the graphene sheet into a single-walled nanotube of chirality (n,m) produces a periodicity criterion that quantizes the two-dimensional wavevector to produce a set of one-dimensional bands. For a nanotube of arbitrary chirality, the band structure can be quite complicated. The main result in the tight-binding model is the separation of nanotubes into three classes: Armchair nanotubes, which are metallic with bands like those on the right side of Fig. 1; a subset of chiral nanotubes with n-m divisible by three, also metallic; and the majority of chiral nanotubes, which are semiconducting with bandgaps inversely proportional to their diameters. An exemplary, although simple, semicon-

ducting band structure is shown on the left side of Fig. 1. Notice that just as in graphene, the conduction bands are mirror images of the valence bands. The gap for the semiconducting tubes varies, independently of helicity, as $1/D$. The density of states in the metallic tubes is also inversely proportional to the diameter.

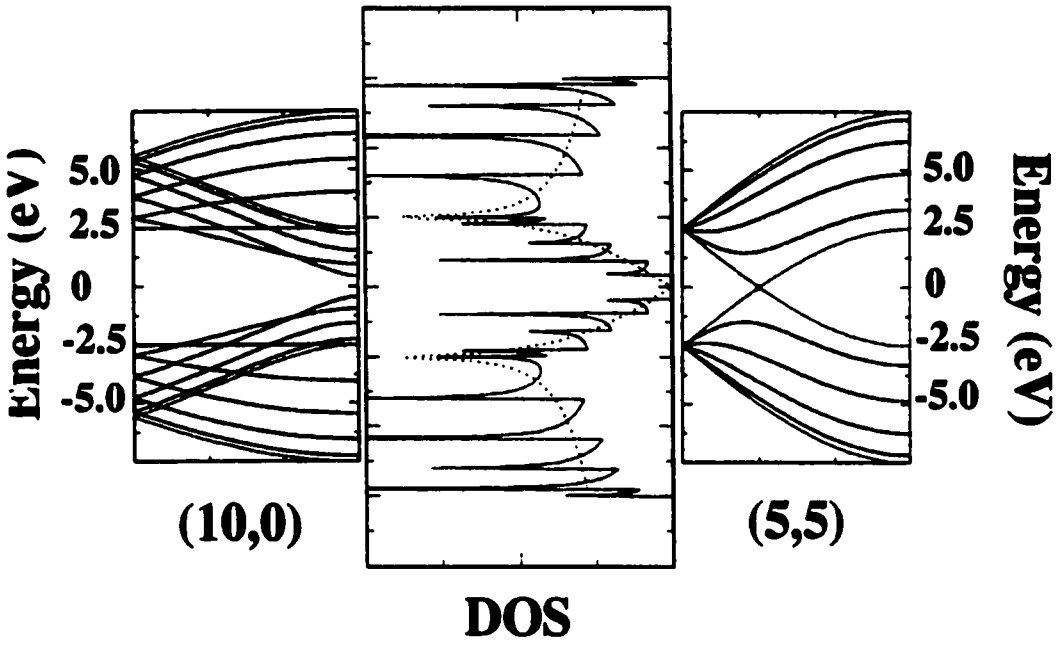

Figure 1. Band structure of semiconducting and metallic nanotubes. In the density of states, the solid line is (10,0), and the dashed line is (5,5).

More detailed theoretical work has modified this picture. Saito, Dresselhaus, and Dresselhaus included an additional trigonal warping term, which slightly splits the degenerate bands in chiral nanotubes.[98] The tight-binding model does not take account of the curvature, which causes hybridization between sigma and pi orbitals. This hybridization has been predicted to open gaps in chiral metallic nanotubes and decrease the gaps of

selected semiconducting nanotubes.[99] Delaney *et al.*,[100] suggested that even in armchair metallic nanotubes, any asymmetric interactions (such as the presence of ropes or substrates) opens a pseudogap. More recently Rochefort *et al.*[101] predicted that twist stress has a similar effect to chirality in opening up a bandgap in originally metallic nanotubes.

If nanotube helicities are distributed uniformly, the n-m divisible by three rule suggests that 2/3 of nanotubes should be semiconductors and 1/3 should be metals. Several groups have used scanning tunneling spectroscopy[102,103] to characterize the density of states of isolated nanotubes and nanotubes within bundles. Although the number of nanotubes that have been examined is small, the 2/3 ratio seems to be correct. Other features of the density of states, including linear dispersion until van Hove singularities at the band edges, have also been observed by STS.[104] Resonant Raman scattering has been used to correlate nanotube diameters with the separation between the van Hove singularities.[105,106]

Recent measurements by Collins *et al.*[107] brought this paradigm into question. They performed room-temperature STS on dispersed nanotubes in an enivronmentally controlled chamber. Before each measurement, he heated his chamber to 100°C in flowing argon. After cooling the samples in argon, he measured the spectrum of an individual nanotube. A typical result is shown in Fig. 2. One spectrum in the plot looks like many others for a semiconducting nanotubes. But after oxygen was admitted into the chamber, the spectrum of the nanotube has changed. The second curve in Fig. 2 has greater apparent density of states at the Fermi level and structure within the gap. It is difficult to extract quantitative estimates of the density of states from STS, so it is not clear how great is the

increase. But certainly it seems as though the semiconducting nanotube has become metallic. Surprising as this sounds, it will be argued later that it can in fact happen.

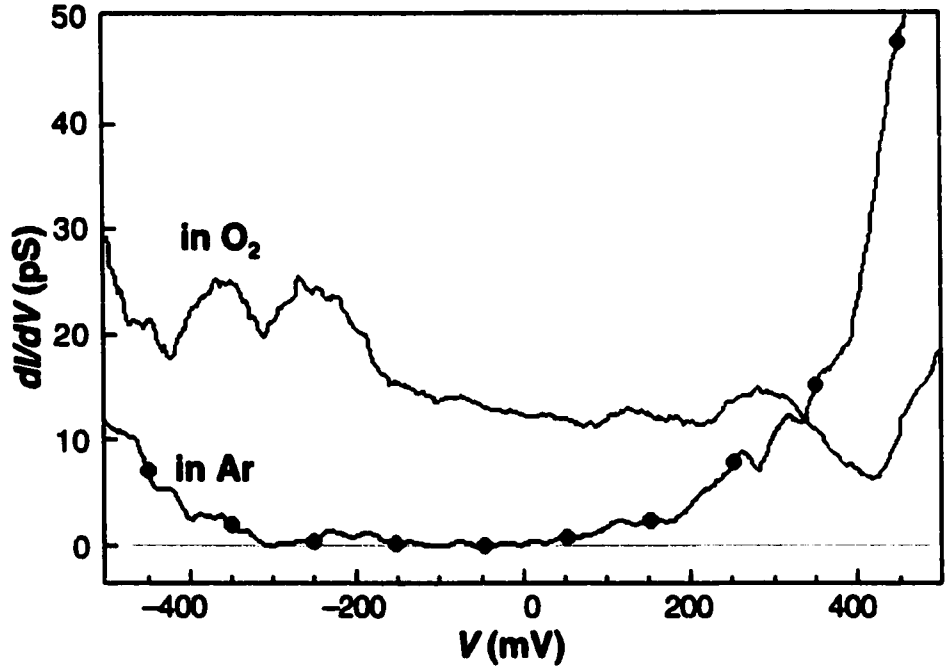

Figure 2. STS of an individual nanotube without and with oxygen environment.

The first two parts of this section will describe experiments on bulk samples to elucidate this oxygen effects on nanotubes. The behavior of thermopower was explored in an attempt to identify the intrinsic thermopower. The second part will discuss $1/f$ noise and the possibility that it might partly be caused by oxygen. Finally, the third part will describe an experiment underway to measure shot noise in nanotubes.

CHAPTER 5

Nanotube thermopower

Introduction

Thermoelectric power (TEP) is an extremely sensitive and incisive transport coefficient. Because it is related to the energy derivative of the electrical conductivity probed at the Fermi energy, it yields directly the sign of the charge carriers within a metallic conductor. For a semiconductor, the TEP probes the sign of the dominant carriers as well as the energy gap magnitude. Single-walled carbon nanotubes (SWNTs) typically cluster in crystalline bundles or "ropes",[108] where each bundle comprises an apparently random collection of metallic and semiconducting nanotubes. Thus, one expects transport measurements of SWNT bundles to reflect this parallel metal/semiconductor combination.

The TEP of SWNTs has been measured previously by various groups[109,110,111] with apparently inconsistent results and with significantly different interpretations. Several surprising features appeared in the measurement by Hone *et al.*[109] Compared to graphite,[112] the TEP is extremely large, and it is large as well compared to other metals.[113] The unusual temperature dependence does not directly fit common models. At low temperatures the nanotube TEP behaves linearly, and it does extrapolate to zero TEP at zero temperature, unlike semiconductors. But at higher temperatures it saturates and does not continue to increase as metallic TEP does. This behavior has been explained in a two-band model with parallel conduction.

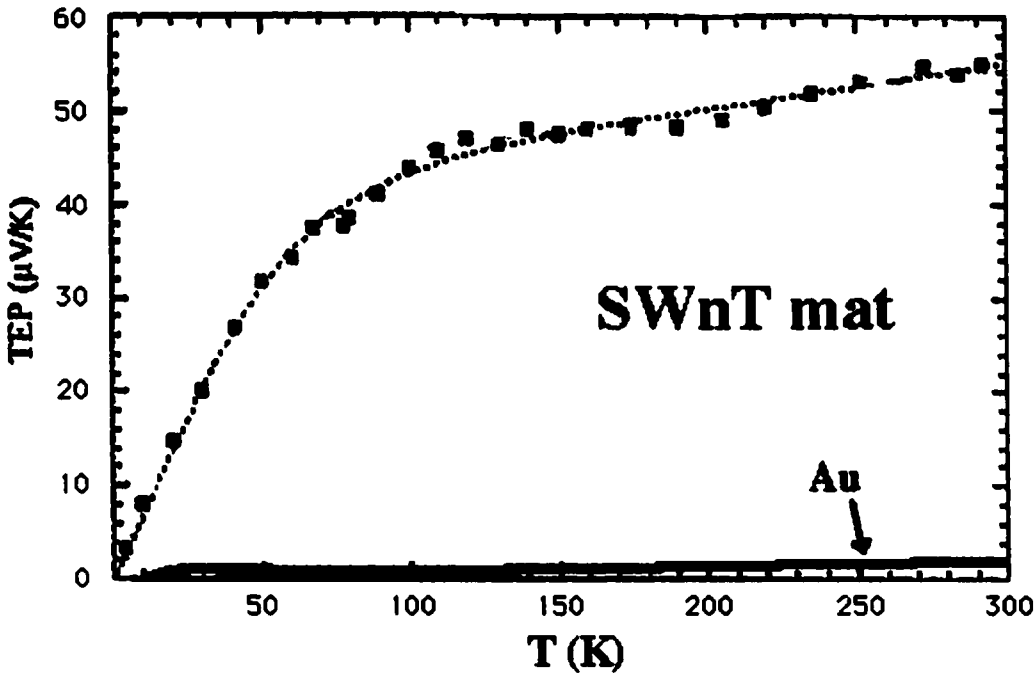

Figure 1. Nanotube TEP as measured by Hone *et al*, compared to TEP of gold.

A number of groups have measured the TEP of nanotubes prepared by various means and subjected to various doping treatments. Different authors report TEP magnitudes that vary by an order of magnitude. The Penn State group[110] have observed a peak in the thermopower. They have attributed this peak, as well as the low-temperature upturn in the resistance,[114] to Kondo scattering by magnetic catalyst particles remaining in the nanotubes.

Recently the Zettl group[107] reported that SWNT electronic properties, including local densities of electronic states, electrical resistance, and TEP, are extremely sensitive to the presence of oxygen. Jing *et al.*[115] have reported related room-temperature resistances changes upon exposing SWNTs to NO_2 and NH_3 gas. As pointed out by Collins *et al.*, the

methods commonly used to prepare SWNTs for measurement generally result in oxygen-contaminated tubes, and it is not obvious that simply placing SWNTs in vacuum at room temperature (as is typically done as an initial step in TEP measurements) reverses this condition. It is thus possible that previous SWNT TEP measurements represent not intrinsic behavior but rather reflect various degrees of oxygen doping.

SWNT TEP has been re-examined with a view to identifying the true, intrinsic behavior. Nanotubes stripped of oxygen indeed have a very different TEP from that of "as prepared" SWNTs. Most importantly, at all temperatures the TEP of oxygen-depleted SWNT's is negative, rather than positive. Using the TEP as a probe, the time constant for oxygen adsorption/desorption has been explicitly determined. A strong temperature dependence is found, and time constants ranging from seconds to days are observed. The temperature dependence of the "saturated" TEP is interpreted within a new model in which oxygen doping causes metallic behavior in a fraction of the semiconducting nanotubes.

Experiments

The experiment used two copper blocks on either end of a quartz substrate. Each copper heat sink comprised a sandwich of two copper blocks clamping two sapphire plates. Each pair of sapphire plates clamped a 0.001" chromel wire which was folded back and forth several times within their area. The chromel wire served as a heater, and was glued to the sapphire plates at the ends, where it exited, by silver epoxy. The quartz substrate, typically 3 mm wide by 12 mm, was clamped to one of the heat sinks at each end. The bottom copper block had a screw for attaching a thermocouple and a hole for inserting a

thermometer. Thick wires for the sample were heat sunk on the bottom end of the sample by being glued to the sapphire substrate by silver epoxy. To minimize heat flow through the sample wiring, all connections to the sample were made with 0.0005" wire. Bulk nanotube samples, or mats, were fabricated using the technique described in the next chapter. Four gold wires were connected at the corners of a mat for resistance and thermoelectric voltage measurements. Chromel-constantan (Type E) thermocouples were fabricated from 0.0005" wire by spark bonding. After spark bonding a junction, it was encased in a small drop of silver epoxy to strengthen it. One junction was glued to the quartz substrate near each end of the sample using silver epoxy.

The thermoelectric power of the sample was measured against gold using a slow ac technique. An ac current with a frequency of 1-10 mHz was applied to the heater at the top end of the sample. The amplitude of the current was chosen to control the size of the temperature gradient across the sample to be less then 1 K or 2% of the absolute temperature. The voltages across the sample and the thermocouple were recorded simultaneously using two Keithley 182 voltmeters. The analog outputs of the two instruments was measured using a data acquisition card in a computer. After one period of the heater current, the sample voltage-thermocouple voltage plot was fit with a line. If the ac current was too fast, the voltages changed faster than the filters in the instruments could respond, and the result was a loop in a plot of sample voltage versus thermocouple voltage. If the current was too slow, the overall thermal offsets in the voltages, which have a $1/f$ spectrum, changed too much, and this change contributed some additional slope. This was a particularly severe problem at high temperature. All cycles in which the plot did not fit a

line were discarded. The slope of the line was related to the thermopower of nanotubes by

$$S_{NT} = \frac{\Delta V}{\Delta V_{TC}} S_{TC} + S_{Au}.$$

Several types of nanotube material were measured, including nanotubes purchased from Rice University and material purified by different methods. Different samples exhibited different magnitudes of TEP that spanned a large part of the range of previous report, but all samples had the same temperature dependence. No reliable value for nanotube TEP was found in the sense that every sample of a given type always had the same magnitude of TEP. As a general rule, however, material which had been processed less had larger TEP. Samples of raw laser ablation product had thermopowers of roughly 60 μV/K; product sonicated in solvent had thermopowers around 30-40 μV/K; and nitric acid-treated nanotubes had smaller thermopowers of 10-20 μV/K. Processing removes impurities from the mats, at the cost of damaging the nanotubes themselves. Since the TEP of the main impurities, graphite and amorphous carbon, are small compared to the TEP of nanotubes, the purification in itself is probably less important than the damage that is inflicted. To examine the importance of various gases and establish a procedure for measuring the 'intrinsic' TEP, a set of experiments was conducted in variable vacuum. Samples were placed in a high-vacuum test chamber equipped with an ion gauge, a residual gas analyzer, and a leak valve close to the sample. The chamber was pumped continuously with a two-stage turbomolecular pump. The sample temperature was monitored with a thermocouple attached to the bottom block. After the sample was loaded, the chamber was pumped to below 1×10^{-8} torr. The chamber was then baked to 120°C and

the sample baked to 220°C for at least 24 hours. Thermopower was continuously monitored during this process. Eventually the thermopower stabilized, the sample was cooled to a test temperature, and a small amount of gas was introduced.

Results

The gases tested included nitrogen, helium, water, and oxygen. Only oxygen was found to affect the TEP. Figure 3 demonstrates the extreme gas sensitivity and associated thermal time constant of the TEP of SWNTs. The plots show the measured TEP (S) as a function of time for two different sample temperatures T. At selected times during the run, the sample environment was switched between 1×10^{-4} torr O_2 and vacuum ($P < 1\times10^{-6}$ torr). For $T=350$ K (filled circles), S switches from a value of -12 μV/K in vacuum to +20 μV/K in O_2. At this sample temperature the response time for the TEP is moderately fast, and the final steady state oxygen-free and oxygen-dosed TEP values are achieved on a timescale of minutes. Although it is not shown in the figure, at slightly higher temperatures (380 K) the TEP response was even faster, limited by the TEP measurements themselves.

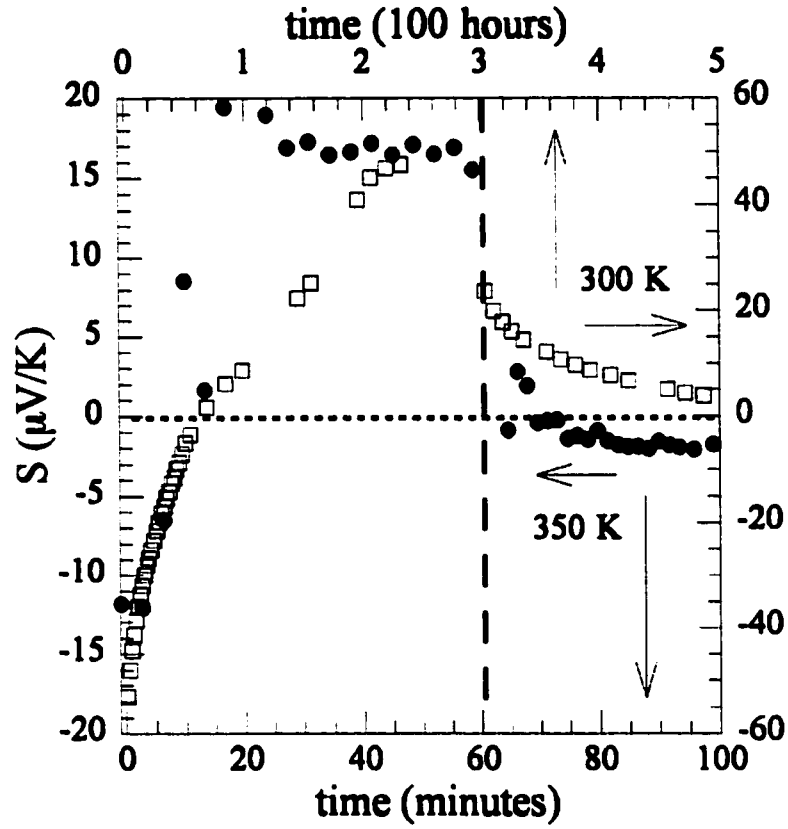

Figure 2. Thermopower histories of two different samples. Filled circles are at 350 K; open squares are at 300 K. In each case the samples in their stable "vacuum" states were exposed to oxygen at $t = 0$. At the time marked by the dashed vertical line, the samples were re-exposed to vacuum. Note the two different x-axis scales.

Figure 3 also shows similar TEP data taken for a different sample at room temperature, $T = 300$ K. Here the TEP again reversibly switches from positive to negative as the environment is switched from O_2 to vacuum, but the timescale for TEP response is much slower: it takes 200 hours for S to recover its final positive value upon oxygen exposure and much longer to approach its final negative value upon oxygen depletion. At

$T < 300$ K, even longer time constants are involved for oxygen depletion. The results of Fig. 3 suggest a complex O_2-pressure/temperature/time phase diagram for the TEP of SWNTs, and illustrate the dangers of measuring S without proper control of environmental conditions and respect for the possibly very long time constants involved.

The variable TEP shown in Fig. 3 is suggestive of a gas diffusion process, and the natural assumption is that the TEP of SWNT is exceedingly sensitive to adsorbed oxygen. As expected, the precise time constant for TEP response in SWNTs was found to be sample dependent. Thick films displayed significantly longer time constants than did dilute thin films. The temperature dependence of the time constant reflects the binding energy of the adsorbed oxygen, which I estimate to be 5000 ± 600 K. The TEP of deoxygenated samples could always be restored to their original "in air" oxygenated value by introducing as little as 1×10^{-5} torr of pure O_2. Higher pressures of O_2 decreased the relevant time constant, but did not affect the steady-state saturated TEP value. Although near-zero TEP was occasionally observed, this seemed only to take place in the course of a transition. It was difficult to reliably "tune" the TEP to selected intermediate values (such as zero) by using selected fixed pressures below 1×10^{-5} torr.

Of interest is the temperature dependence of the steady-state, "saturated" TEP of SWNTs for different oxygen coverage conditions. I explored the reliably-achieved extremes: the TEP of SWNTs in the "fully oxygenated" condition, and the TEP of SWNTs largely depleted of oxygen. These experiments were run in a specially constructed cryogenic probe. This probe was designed to allow the sample to be heated to 220°C and

cooled to cryogenic temperatures without changing the atmosphere. The vacuum chamber and dip probe were both formed by a long tube with Conflat flanges on both ends. A Macor block attached to a Conflat blank flange served as a partial thermal isolation. The copper blocks of the experiment were attached to the top of this standoff, and the blank flange was attached to the bottom of the long tube. Wires from feedthroughs at the top were clamped to insulating Macor heat sinks on the blank flange before being glued to the sapphire plates. The pressure was monitored by an ion gauge at the top of the tube, and the apparatus could be pumped continuously by a single-stage turbomolecular pump. The sample temperature was measured from cryogenic temperatures to high temperatures by a calibrated platinum resistance thermometer. It was tested to measure temperatures reproducibly above 20 K.

Based on the results of the first experiment, the procedure for the experiment was as follows. The chamber was evacuated for less than half an hour, a valve on the top was closed, and the probe was lowered into liquid helium. This cooled the sample quickly and directly to 20 K. During this process, the TEP is presumed not to have changed significantly. The sample was then heated slowly by the heater on the bottom copper block while the TEP was measured. As the sample temperature neared room temperature, the probe was removed from the helium. As it was heated above room temperature, pumping was resumed. When the sample temperature neared 100°C, the entire bottom flange was heated to 220°C. The flange and sample were left in dynamic vacuum at high temperature for at least 24 hours, while the vacuum was better than 1×10^{-6} torr. The sample and flange were allowed to cool slowly, while TEP was measured again. When they had

cooled to room temperature, the valve was closed and the probe was lowered into liquid helium. At this point the sample TEP was generally observed to change quickly by a small amount. This was probably due to the adsorption of a small amount of residual oxygen due to the temperature difference between the sample and the top part of the probe. The valve to the pump was opened quickly after lowering the probe to minimize this effect.

Figure 4 shows $S(T)$ for the same SWNT specimen for these two extremes. The upper curve shows the first measurement, $S(T)$ under the fully oxygenated conditions. The TEP is always positive and extrapolates to zero as $T \rightarrow 0$. Notably, these data contain no convincing evidence for a lower temperature bump or peak in S, as might be expected from a Kondo impurity mechanism.[110] The lower curve in Fig. 4 represents the second measurement of S, after the sample has been deoxygenated. In this case S is always negative, with a room temperature magnitude comparable to that measured under oxygenated conditions. Again, S smoothly approaches zero as $T \rightarrow 0$, and no anomalous low temperature bump or peak is observed. Interestingly, the functional forms of $S(T)$ for fully oxygenated and deoxygenated SWNTs appear to be rough "mirror images" of one another, reflected about the horizontal axis. I observed this apparent symmetry, suggestive of a universal $S|T|$, in all of the SWNT samples that I measured. This similarity suggests that a common mechanism may account for the TEP of both oxygenated and deoxygenated SWNTs.

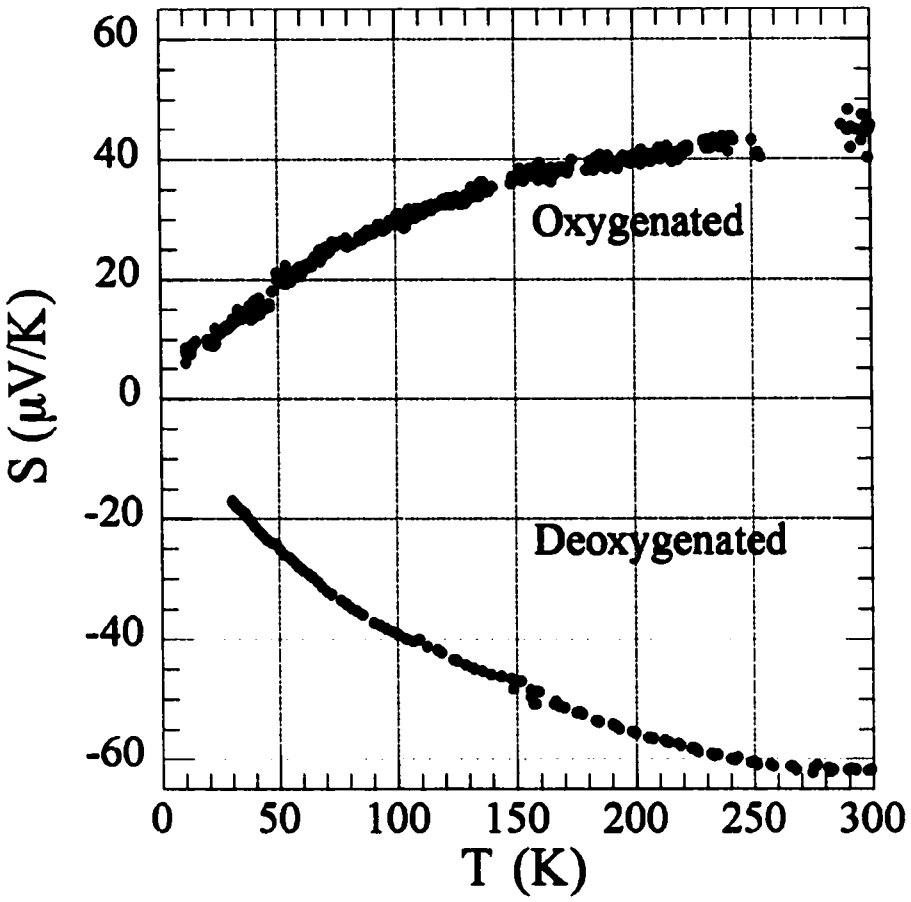

Figure 3. The temperature dependence of thermopower for a single sample in its "oxygenated" and "deoxygenated " states.

Discussion

Different SWNT TEP models have been proposed, which I will briefly review and discount in light of the data presented above. First note, again, that the observed TEP of SWNT is much larger in magnitude than that of graphite ($S \sim 5$ μV/K).[112] The temperature dependence of nanotube TEP is remarkably similar to what has been observed in

graphite intercalation compounds.[116] In these materials the high-temperature flattening of the thermopower has been explained in terms of the interaction of intercalants with two-dimensional phonons. Such effects are unlikely in nanotubes in one-dimensional nanotubes. I saw no Kondo peaks in the TEP, and I rule out a Kondo-based mechanism.

An obvious possibility previously considered is a simple two-band model in which the total TEP is a parallel combination of TEPs from semiconducting and metallic tubes.[109,111] Let us suppose that the conductivity and TEP of semiconducting and metallic nanotubes follow the formulae for bulk solids. For the semiconductors,

$$S_{SC} = \left(\pm\frac{k}{e}\right)\left(\frac{E_g}{T} + \frac{\partial}{\partial\varepsilon}\tau + \frac{5}{2}\right), \; G = d\exp((-E_g)/T).$$

For the metals, $S_m = \frac{k\pi^2}{e\,3}\left(\frac{\partial \ln\sigma}{\partial\varepsilon}\right)T$, $G = \frac{c}{T}$.

The ratio k/e, the natural unit of thermopower, is equal to 86 μV/K. Scaling by this unit, $\widehat{S}_{SC} = E_g/T + 5/2 + a$, $\widehat{S}_M = bT$.

The thermopower of the parallel combination is $S = \frac{1}{G}(G_M S_M + G_{SC} S_{SC})$. Assuming that the conductance of the metals dominates, the fitting model is

$$S = bT + \frac{d}{c}\exp(-E_g/T)\left(E_g + \left(\frac{5}{2} + a\right)T\right).$$

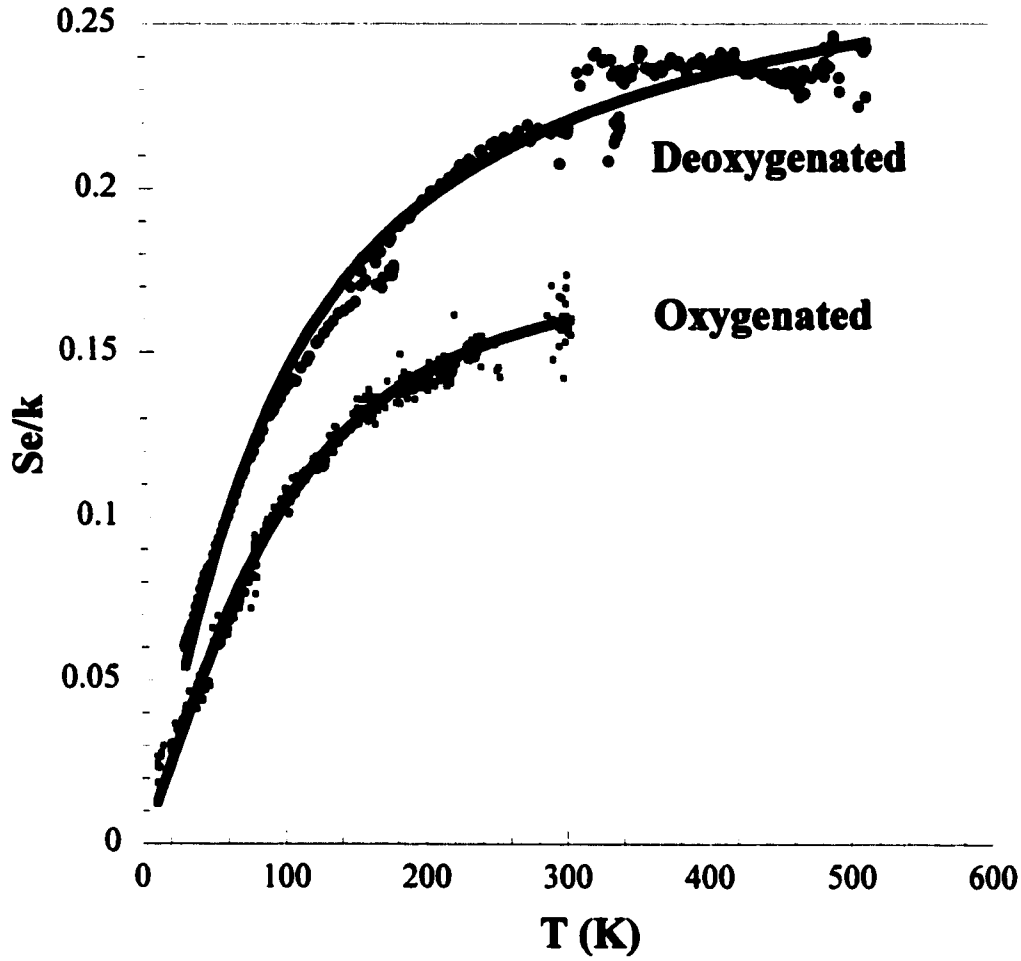

Figure 4. Two-band model fits to the data of Fig. 4. Both sets have been plotted as postive TEP for comparison.

TABLE 1. Parameters of the two-band model.

	a (K^{-1})	d/c	E_g (K)	b
Oxygenated	4×10^{-3}	-3×10^{-5}	190	164
Deoxygenated	-4×10^{-3}	8×10^{-4}	300	4

The TEP curves can be fit reasonably well using such a model, as shown in Fig. 5, but the fitting parameters (see the table for an example) are less than satisfactory in several respects. First, the extracted semiconducting tube energy gap values of 10-20 meV are significantly smaller than have been observed in single-tube transport[117,118] and scanning tunneling spectroscopy measurements.[119,120] This model consequently predicts conductances for the semiconducting tubes that are considerably larger than typical observations.[121] Similarly, the metallic contribution of $b = \frac{\pi^2}{3}\frac{\partial \ln\sigma}{\partial \varepsilon} = 0.004$ predicts an unphysically large TEP magnitude (100 μV/K at room temperature) for the metallic tubes. Within this model the measured magnitude of the (temperature dependent) TEP is due to a near-cancellation of very large metallic and semiconducting TEPs of opposite sign, a situation I regard as unlikely.

Recently a different two-band model[122] has used the Nordheim-Gorter relation. This rule was originally proposed to explain the thermopower of dilute alloys. The thermopower is considered to come solely from metallic nanotubes, with adsorbed gases providing large scattering. The resistivity ρ is the sum of intrinsic resistivity ρ_0 and additional gas-induced resistivity ρ_a. The conductivity is then $\sigma = \frac{1}{\rho} \approx \frac{1}{\rho_0}(1 - \rho_a/\rho_0)$.

The TEP of the metal can therefore be approximated by

$S = \frac{\pi^2}{3}T\frac{\partial \ln\sigma}{\partial \varepsilon} = \frac{\pi^2}{3}T\left[\frac{\partial \ln\sigma_0}{\partial \varepsilon} + \frac{\partial}{\partial \varepsilon}(1 - \rho_a/\rho_0)\right]$. The second term is approximately equal to $\left(-\frac{\partial}{\partial \varepsilon}\right)(\rho_a/\rho_0)$, which can be rearranged to give

$\frac{\rho_a}{\rho_0}\left(\frac{\partial \ln \rho_a}{\partial \varepsilon} - \frac{\partial \ln \rho_0}{\partial \varepsilon}\right) = \frac{\rho_a}{\rho_0}(S_0 - S_a)$. The total TEP is $S = S_0 + \frac{\rho_a}{\rho_0}(S_a - S_0)$. This model has been used to explain the change in sign as a result of gas scattering ρ_a (S_a). I believe this model is inappropriate. The key assumption made by Nordheim and Gorter and revealed in this discussion is that ρ_a is small compared to ρ_0. On the contrary, I have typically observed that degassing increases the resistance of nanotube mats by 40-50%. The Nordheim-Gorter model may be useful for explaining thermopower changes due to inert gas exposure, when the resistance changes because of scattering. In the case of oxygen effects, the resistance change is more likely to result from changes in carrier density.

New model calculations by Seung-Hoon Jhi[123] for the effect of oxygen on nanotubes provide a consistent explanation for the thermopower of SWNTs. Probably oxygen exposure will have little direct effect on metallic armchair nanotubes. In order to investigate the effect of oxygen doping on semiconducting nanotubes, Jhi carried out pseudopotential first-principles calculations on an oxygen-doped (8,0) semiconducting nanotube. O_2 was found to bind to the nanotube with an adsorption energy of about 0.3 eV. This number should be compared with the scale empirically determined from the temperature dependence of adsorption times, 0.4 eV. In the predicted band structure, O_2 molecular levels lie at the top of the valence band of the carbon nanotube and overlap slightly with carbon states. About 0.1 electron transfers from the nanotube to an oxygen molecule, supplying hole carriers to the nanotube.

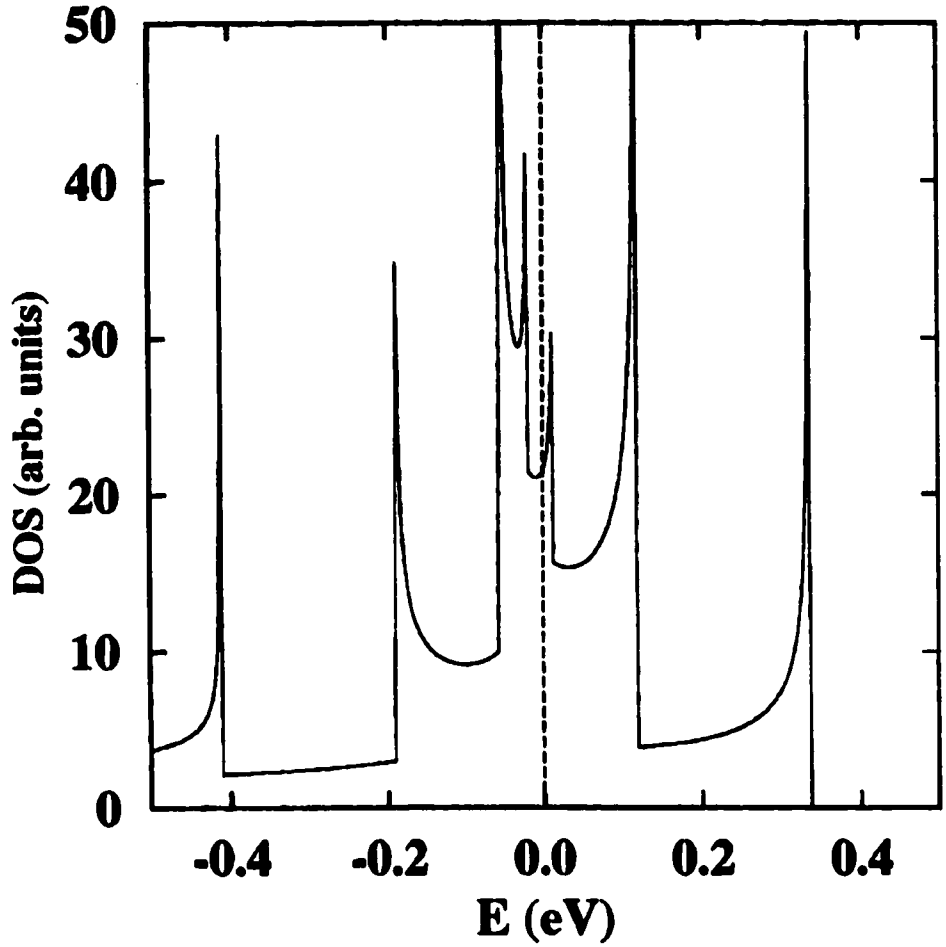

Figure 5. Calculated density of states for an (8,0) nanotube doped by adsorbed oxygen molecules.

Figure 5 shows the calculated density of states of an oxygen-doped (8,0) tube. The intrinsic DOS, not shown in the figure, features a gap of 0.6 eV centered on the Fermi level at zero energy. As the oxygen molecule breaks the symmetry of the nanotube, the two-fold degenerate valence bands split and give two peaks in the DOS. Near the Fermi level, the DOS of the doped semiconducting tube can be written as

$D_S(\varepsilon) \propto [\Delta^2 - (\varepsilon - \varepsilon_0)^2]^{1/2}$ where Δ is the band width ($\Delta \sim$ O(1) eV) and ε_0 is the center of the band energy.

The oxygen doping significantly enhances the conductivity of the semiconducting nanotubes. This conductivity can be estimated in a Drude model. The density of carriers, 0.1 electron/unit cell, suggests that the conductivity can be comparable to that of graphite. The TEP of the mats can then be written as $\widehat{S} = \frac{\pi^2}{3}kT\left[C + \alpha\frac{D'_S}{D_S}\right]$, where the constant C accounts for the small thermopower of the normally metallic tubes, D_S is the DOS for semiconducting tube, and D'_S is the derivative of D_S with respect to energy at the Fermi level. This is a two-band model in which the second band is also metallic. The metallic TEP expression for the semiconducting nanotubes is appropriate because the strong oxygen interaction produces states at the Fermi level. The coefficient α denotes the ratio of the conductivity of the semiconducting tubes to the total conductivity of tube mats. I will allow the TEP of the normally metallic nanotubes to be small as in graphite. This is reasonable since they have smooth DOS and electron-hole symmetry. Instead I will focus on the second term. Using Eq. (1) for the DOS of the semiconducting tubes, the second term in the TEP is $\widehat{S}_S = -\frac{\pi^2}{3}kT\alpha\frac{(\Delta - \delta)}{2\Delta|\delta|}\operatorname{sgn} D'_S$ where $\delta = \Delta - (\mu - \varepsilon_0)$. When the chemical potential μ is near the band edge, the magnitude of S_S can be very large. At room temperature, the second term in S is estimated to be about 60 μV/K with $\delta \approx 0.01$ eV and $\alpha \approx 0.2$. These particular values are not important; since the carrier

density depends on the position of the Fermi level, changes in δ are compensated by changes in α. This magnitude agrees well with the measurements.

The value of α for a particular sample will depend on the fraction of effectively doped semiconducting tubes. The model therefore provides a natural explanation for the different magnitudes of S that are observed. The different treatments are expected to functionalize the nanotubes to a greater or lesser degree. Acid-treated nanotubes, for example, are functionalized by carboxylic acid groups.[124] These groups reduce the number of available sites for oxygen adsorption. The density of doped holes should therefore be smaller.

The change of sign is also readily explained in this model. Due to the weak hybridization, the DOS of the carbon bands has a tail above the peak of the DOS. As the oxygen pressure changes, the doping level of the tubes is varied, moving the Fermi level. Because the sign of S_S depends on that of D'_S, the sign of the measured TEP changes when the Fermi level crosses from one side of the peak to the other. The sharpness of the peak accounts for the observation that the TEP cannot be easily stabilized at zero.

CHAPTER 6 *Nanotube 1/f noise*

The current capacity of a single metallic single-walled nanotube has been measured to be 25 μA,[125] which corresponds to a current density of more than 1 GA/cm^2. This excellent conduction makes nanotubes candidate materials for a variety of electronic applications, including interconnects,[126] electromechanical switches,[127] and field emitters.[128] These devices will depend not only on high currents, but also on low noise properties. Collins *et al.*[129] reported that, contrary to expectations, nanotubes exhibit enhanced levels of $1/f$ noise. Some method of reducing this noise is necessary for nanotube electronic applications to be viable. The recent discovery that nanotube electronic properties are extremely sensitive to oxygen suggests that $1/f$ noise may also be affected. I have explored the dependence of $1/f$ noise on sample treatment and gas environment with a view to decreasing noise levels.

Methods

Fabrication of nanotube films

Single-walled carbon nanotubes were obtained from Rice University. Some experiments used nanotubes purified at Rice University (Tubes@Rice). This purification process involved sonication in nitric acid, which digests all the amorphous carbon. The nanotubes were subsequently suspended in water with Triton-X surfactant. This purification results in material that is 90% nanotubes, but at a cost of significant damage. This Tubes@Rice material was transferred to isopropanol using a centrifuge for dilution. A

centrifuge was filled with 10 mL of nanotubes in Triton-X suspension and then run at 5000 rpm for 10 minutes. The nanotubes settled to the bottom but remained suspended, albeit in larger clumps. Approximately 8 mL of liquid was decanted and replaced with isopropanol. This process was repeated 4 times to obtain a suspension of nanotubes in isopropanol. This material will be referred to in this thesis as "acid-treated" nanotubes

Other material used was raw laser ablation product purchased from Rice University. The raw material contains roughly 15% nanotubes. This material was purified by filtration in methanol. A 2 μm filter was placed on top of a frit on a flask. On top of the filter was placed a second piece of glassware which served as a beaker. A quantity of fuzz was put into this beaker, which was then filled halfway with methanol. When vacuum was established under the frit, the methanol dripped through the filter, carrying small particles with it. To prevent nanotubes from clogging the filter paper, the methanol was sonicated continuously continuously with a 300 W horn. Periodically the methanol bath was refilled. This process was continued for several hours until clear methanol dripped from the frit. The resulting material contained perhaps 70-80% nanotubes. It was transferred into isopropanol in the same way as the acid-treated material.

Samples were dispersed onto quartz substrates by drying. Quartz substrates were cut to the desired shape, depending on the experiment. A drop of isopropanol suspension was deposited on the substrate. As the suspension dried, the nanotube webs gradually coalesced into larger networks. Convection carried them to the edge of the chip, where they were pinned on the cracked edge. Consequently, most nanotubes tended to be deposited on the edge, and few were deposited in the middle. To avoid this problem, when the solu-

tion had dried enough that the nanotube networks were fairly large, they were manipulated with a clean metal tip until they were in a desirable location. They were held in place by the metal, which was not allowed to touch the quartz surface, until the solution had dried so much that the networks could not move easily. The tip was removed and the substrate was allowed to dry completely. The networks formed a thin, flat, adsorbed layer on the substrate, which did not move and was not disturbed when another drop was added. This process was repeated until there was an area of continuous mat large enough for the desired experiment. In the course of this process, many of nanotubes were deposited in undesirable places, including over the edge. They were scraped from the substrate with a clean razor blade, leaving only the desired sample. Wires were attached using silver epoxy. The resistances of samples fabricated in this way varied from tens of ohms to a few thousand ohms, depending on their thickness. A sample with a resistance of a few thousand ohms was one or two microns thick.

Noise measurements

Resistance was measured using a standard four-wire technique. For measurements of resistance versus time, the sample voltage was detected with the computer's DAQ card reading voltages at a constant sampling rate. This sampling rate was used as the clock for the time measurement.

Noise was measured using two different four-wire techniques. In the first, a dc current was passed through the sample with two wires and the ac voltage across the sample was measured with two additional wires. Noise is a fairly small signal, so the details of the electronics are important. The circuit can be modelled with a small list of components. A

dc voltage source V_0 with output impedance r is in series with an ac voltage source v_1 and a resistance of δr; these represent the current source and its noise. The sample is represented by a resistance R_s in series with an ac voltage source v_t and a small resistance δR_s v_t. represents the thermal noise of the sample, and the variable resistance δR_s represents the fluctuations in the sample resistance that generate the $1/f$ noise. If the noise is caused by resistance fluctuations, the detected noise voltage will be proportional to the applied voltage $\delta V \propto V\frac{\delta R_s}{R_s}$.

The 'current source' is represented as a voltage source with high impedance not only for convenience in the model. None of the available current sources were quiet enough at low frequencies. In practice, a 9 V battery, which was found to be fairly quiet, and a current-limiting resistor, supplied the excitation. The amount of current through the sample was controlled with a potentiometer as part of the current-limiting resistor. The resistance fluctuations δr_s come primarily from those in the potentiometer; they were minimized by using 10-turn wire-wound potentiometers. All resistors were wire-wound precision resistors.

The voltage detection circuitry was built around a PAR 113 low-noise audio preamplifier. The equivalent noise impedance of this instrument is 1 MΩ, much larger than the typical mat samples. To make it possible to measure sample noise voltages below the thermal noise floor of the amplifier, a low-frequency transformer, Model PAR103, was inserted. The transformer gain of 100 raises the sample thermal noise to the level of the

amplifier noise. To protect the transformer from the high dc current passing through the sample, both legs were connected through capacitors designed for sub-hertz cutoff frequencies.

The output from the PAR 113 amplifier could be connected to a variety of measurement instruments, including a spectrum analyzer or a home-built software-based spectrum analyzer. For most ranges of sample resistance, the transformer gain is not flat in frequency, but has a peak near 32 Hz. For most measurements, therefore, the noise was measured with a Stanford 830 lock-in amplifier tuned to 32.537 Hz. The noise voltage was demodulated and rescaled by the lock-in for its analog output and then measured using the computer's DAQ card.

For extremely low values of $1/f$ noise, this method is insufficient. The smallest value of noise that can be measured in this way is the thermal noise of the sample. As the magnitude of the $1/f$ noise becomes smaller, it becomes necessary to measure the noise at lower frequencies in order to detect noise above the thermal noise floor. The method described above is limited by an inability to measure noise at very low frequencies. The dilemma is not the 32 Hz peak in the transformer, which could after all be replaced by a different transformer. Rather, there are additional sources of noise at low frequencies. Particular sources include thermoelectric fluctuations in the wires and $1/f$ noise in the preamplifier.

Noise values below the amplifier floor were measured with a modification of the method of Pelz.[130] He divided his sample in two halves and arranged them with two other

resistors in a Wheatstone bridge. He passed an ac current through them and balanced the Wheatstone bridge so that the average value of the ac voltage between the legs of the bridge was zero. As the two halves of the sample resistance fluctuate without correlation, the voltage between the legs fluctuates. This voltage can be measured by a lock-in amplifier tuned to the applied ac current.

The small fluctuating voltage can be amplified before being introduced to the lock-in amplifier. This provides the key advantage of the technique: The low-level signal of interest, this fluctuating signal, takes place very near the frequency of the applied current. This frequency can be made as high as necessary to avoid any $1/f$ noise in the amplifier or environment. The lock-in amplifier performs its processing on a considerably larger signal.

One disadvantage of the method just described is that it is a two-probe measurement. In addition, nanotube mats cannot simply be divided in half in the same way that a copper film can. They are not homogeneous conductors, and I found that the voltage measured at various places in a rectangular patch of mat usually did not correspond to a uniform current flow. To solve these problems, the current passed directly through he sample and then through a variable current-sense resistor. The voltages across the sample and the current-sense resistor were each amplified by a differential low-noise audio preamplifier (Stanford 530). The output of each amplifier was compared to ground. One amplifier was inverted, and then the two outputs were connected to the differential inputs of the lock-in amplifier. The voltage to be measured by the lock-in is then the difference between the sample four-wire voltage and the current-sensing resistor's voltage. The variable current-

sense resistor could be tuned to null this measurement. Any fluctuations in the contact resistance of the sample cause fluctuations in the current, which passes through both sample and current-sense resistance. They are therefore automatically nulled.

Consider the processing performed by a lock-in amplifier. The instrument multiplies the signal voltage by its reference voltage, of constant (presumed unity) amplitude. The products of this operation are two signal voltages shifted to higher and lower frequencies by the reference frequency. The $1/f$ noise signal takes place at frequencies very near the reference frequency, so its products will be near dc and $2f_0$. The lock-in then filters this product with a low-pass filter to remove unwanted signals, including the right-shifted signal. The Stanford 830 lock-in outputs the result of this filtration at an analog output on its back panel. This output therefore carries a signal which is proportional to the actual resistance fluctuation, but has a scale of 1 V. This signal was measured as a function of time with the computer's DAQ card. The Fourier transform of this signal was used to calculate the noise intensity spectrum.

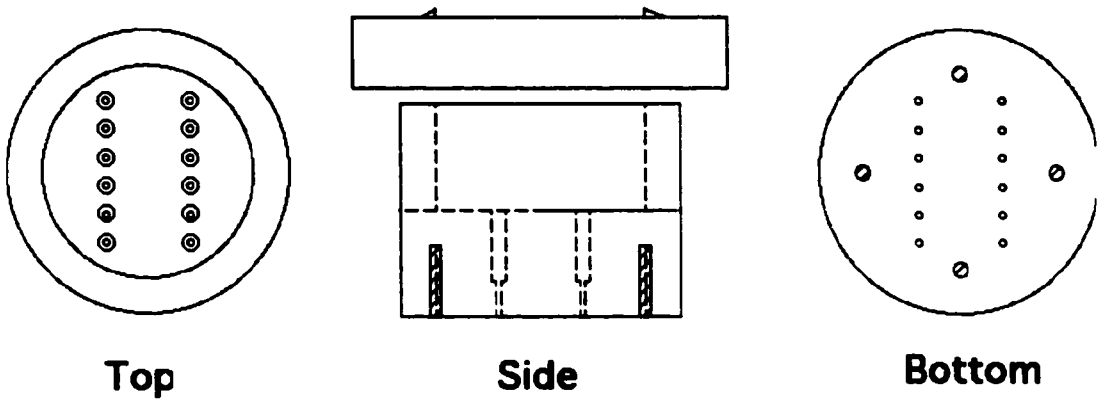

Figure 1. Diagram of the sample vacuum vessel.

Sample vacuum containers

Several vacuum chambers were used for these experiments, including the high-vacuum test chamber and the specially constructed cryogenic probe described in the last chapter. For low-level noise measurements a special UHV vessel constructed in the department machine shop was also used. Figure 1 shows a 1" diameter copper cylinder hollowed out, with holes drilled in its base to fit Samtec gold-plated connectors. These connectors, which served as electrical feedthroughs, were glued in the holes, pins sticking out, with Epo-Tek H-74F high-temperature solid epoxy. A Conflat flange was silver-soldered on the top of the vessel. After a sample was mounted in a chip carrier, the chip carrier was plugged into the Samtec gold pins. The vessel was sealed with a sescond Conflat flange connected by a glass-metal seal to a Pyrex tube. After the vessel was evacuated to the desired pressure, the Pyrex tube was sealed with a torch. The Samtec gold pins plugged into a cryogenic probe, and the vessel had screw holes for attaching it firmly to the probe. A thermometer was mounted on the outside of the vessel.

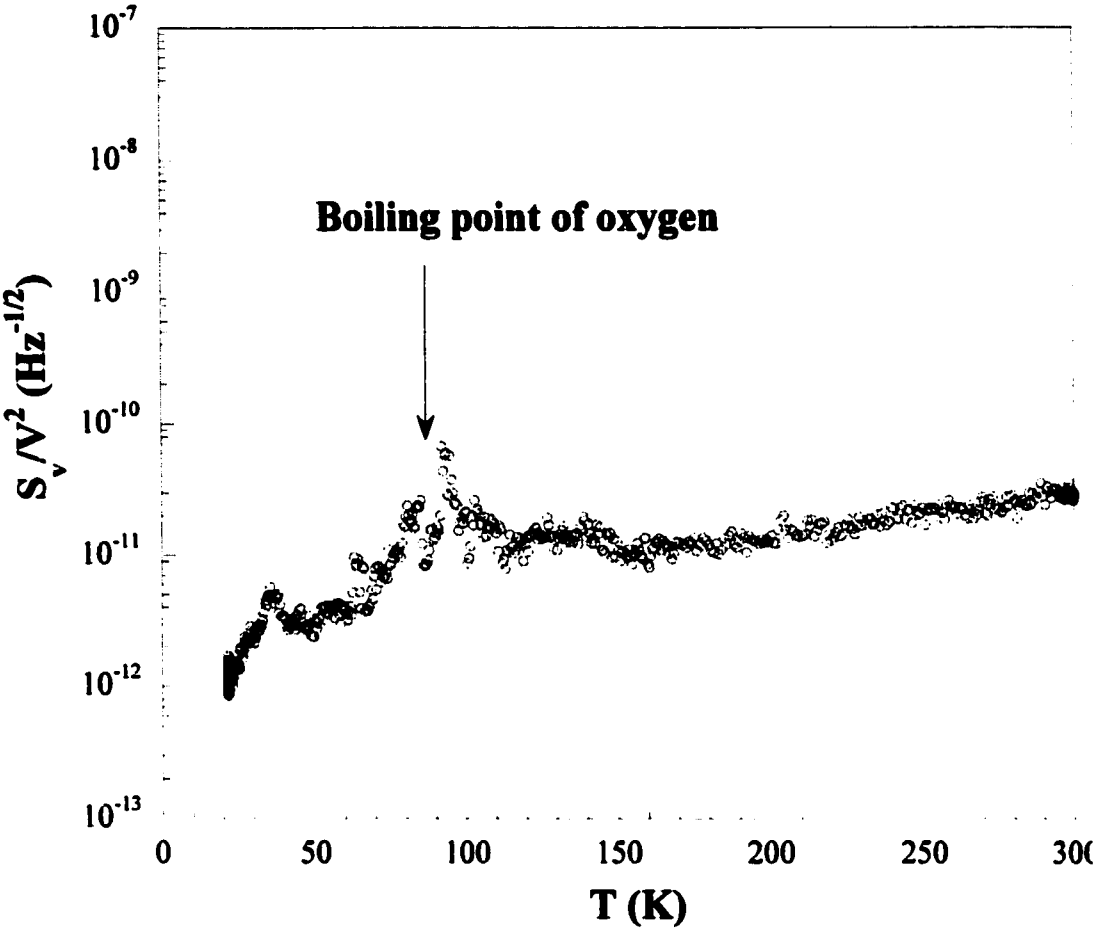

Figure 2. Noise of an 'oxygenated' sample sealed in rough vacuum. 32 Hz.

Results and discussion

Three paths have been identified for 1/f resistance noise: fluctuations in number, in mobility, and in temperature.[131] Two of these play significant roles in nanotube noise.

Two kinds of effects illustrate the importance of oxygen. In Fig. 2, the noise of a sample that has not been deoxygenated according to the recipe of the last chapter shows a pronounced peak around the boiling point of oxygen. This peak may be due to critical fluctuations in the pressure of oxygen. Figure 3 shows the effect of baking on the noise.

These data were taken by exposing a sample to vacuum at room temperature and measuring the noise continuously while the temperature was increased to 200°C. The sample remained at 200°C in dynamic vacuum while the noise fluctuated wildly up and down. After 24 hours, the noise settled at a final, lower value. The sample could be heated subsequently, and the noise level remained constant at the low value. This behavior can be understood as the result of number fluctuations. In their spectroscopy of bare and doped

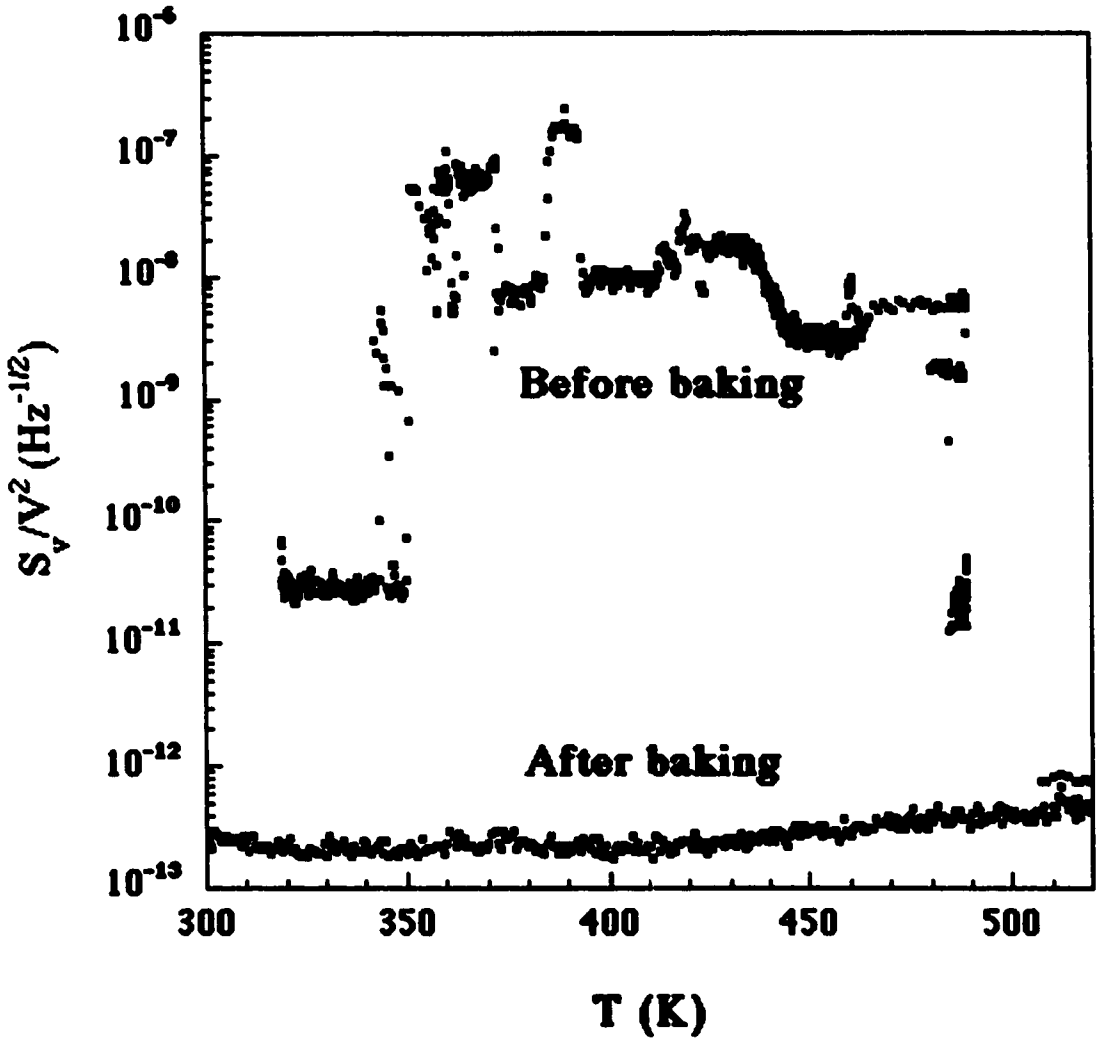

Figure 3. Comparison of oxygenated and deoxygenated noise levels.

nanotubes, Collins *et al.*[107] found that one half of the nanotubes they investigated were

semiconductors that became metallic after being exposed to oxygen. The evidence presented in the previous chapter suggests that the binding energy of oxygen molecules can reach 0.4 eV. In equilibrium, molecules are desorbing and adsorbing at a rate which can be estimated as follows. Jhi *et al.*[123] have calculated the shape of the potential well for an oxygen molecule adsorbed on a single-walled carbon nanotube. At the bottom of the well, the energy is approximately $U = \frac{1}{2}kx^2$, with $k = 3000\text{eV/nm}^2$. The vibration frequency of an oxygen molecule in this well is approximately $\omega = \sqrt{\frac{k}{m}}$; for an oxygen molecule in the calculated potential well the frequency is 9×10^{13} Hz With the Boltzmann factor $e^{-E/kT}$, the frequency with which molecules leave the nanotube is approximately $\nu = \omega e^{-E/kT}$, where ω has been used as an attempt frequency. These fluctuations will contribute noise with a Lorentzian spectrum of characteristic frequency ν (4 GHz for an (8,0) tube with an oxygen binding energy of 0.25 eV). In a real nanotube sample, the binding energies vary among nanotubes of different diameters and binding sites of different character. The smeared assembly of Lorentzian spectra presents a $1/f$ appearance as in the model of Dutta and Horn for $1/f$ noise.[132] The appearance of an activation factor in the noise power should cause the noise to depend on temperature. The detailed behavior must depend on the particular distribution of energies. Dutta and Horn calculated that for distributions that are approximately uniform, the noise power is roughly linear in temperature. The data of Fig. 2 fit this prediction reasonably well.

Let us estimate the intensity of the noise. Fuhrer *et al.*[133] have measured the resistance of nanotube-nanotube junctions to be approximately 100 KΩ. A If nanotubes are 1 micron long, a sample 10 mm long must contain, along any path, at least 10000 junctions. If the resistance of the sample is 1 KΩ, there must be 1×10^{6} paths in parallel. These paths form the bottleneck through which current must pass. Using the estimate discussed before that oxygen molecules donate 0.1 electron/unit cell of charge to a semiconducting nanotube, we can estimate that the number of oxygen molecules involved is $N = 1\times10^{8}$. The statistical fluctuation in the number of oxygen molecules is 1×10^{4}. As a crude estimate, the relative size of the resistance fluctuations should be $1/(\sqrt{N})$, or 1×10^{-4}.

After the nanotubes have been cleaned of oxygen, the noise is 100 times smaller. To examine this low level of noise further is difficult. In principle the noise could be increased by passing more current through a sample, but in practice this is not acceptable. When currents larger than several hundred μA were used, these samples exhibited nonlinear resistance due to Joule heating. I therefore turned to the extremely low-frequency techniques described. Figure 4 shows a spectrum extending to 1×10^{-4} Hz. The measurement of such extremely low frequencies requires good control of temperature. Typical temperature controllers allow the temperature to fluctuate by as much as several mK. Since nanotubes at low temperatures have insulating resistance, such fluctuations were reproduced in the sample noise at a detectable level. Stability was achieved at several temperatures by immersing the copper vessel (suitably protected) in liquid baths. The temper-

atures were set by the availability of liquid helium (4.2 K), liquid nitrogen (77.5 K), dry ice (in acetone slurry) (197.5 K), and ice water (273 K).

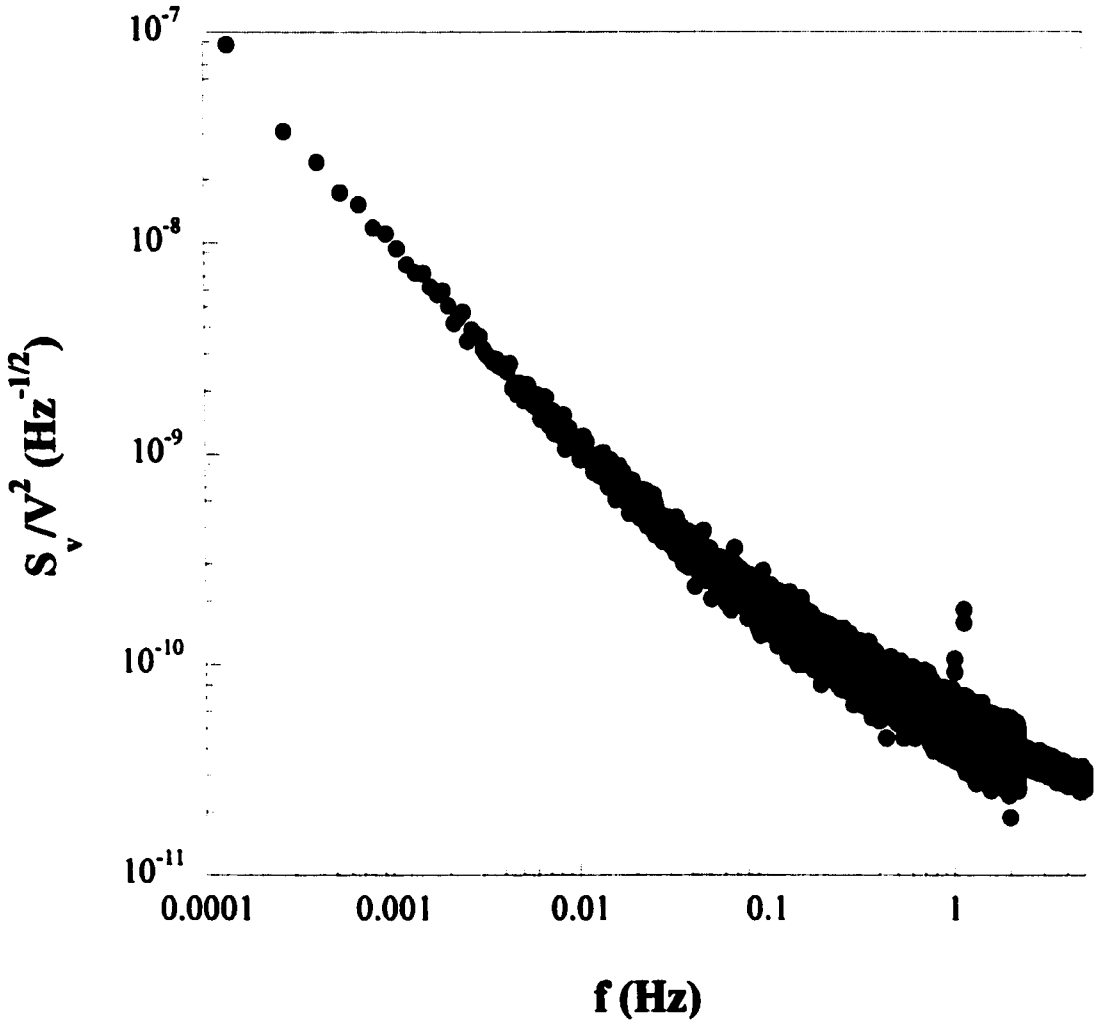

Figure 4. Low-frequency spectrum of a deoxygenated sample. No cutoff is apparent.

The results shown in Fig. 5 suggest that the remaining noise can be attributed to temperature fluctuations. In the model of Voss and Clarke,[134] the intensity of the fluctuations depends on temperature is $S\frac{S}{R^2} \propto \left(\frac{d\ln R}{d\ln T}\right)^2 \frac{1}{C_v}$. The resistance of nanotube mats is propor-

tional to $\exp(-(T_0/T)^{-1/4})$.[114] Although the specific heat of single-walled carbon nanotubes has been measured,[135] this measurement was probably complicated by the presence of adsorbed gas. For simplicity I will assume that $C_v \propto T$. So the value of S/R^2 should vary as $T^{-3/2}$. From my four points I find that the exponent is -1.1, which agrees reasonably well with the model of Voss and Clarke.

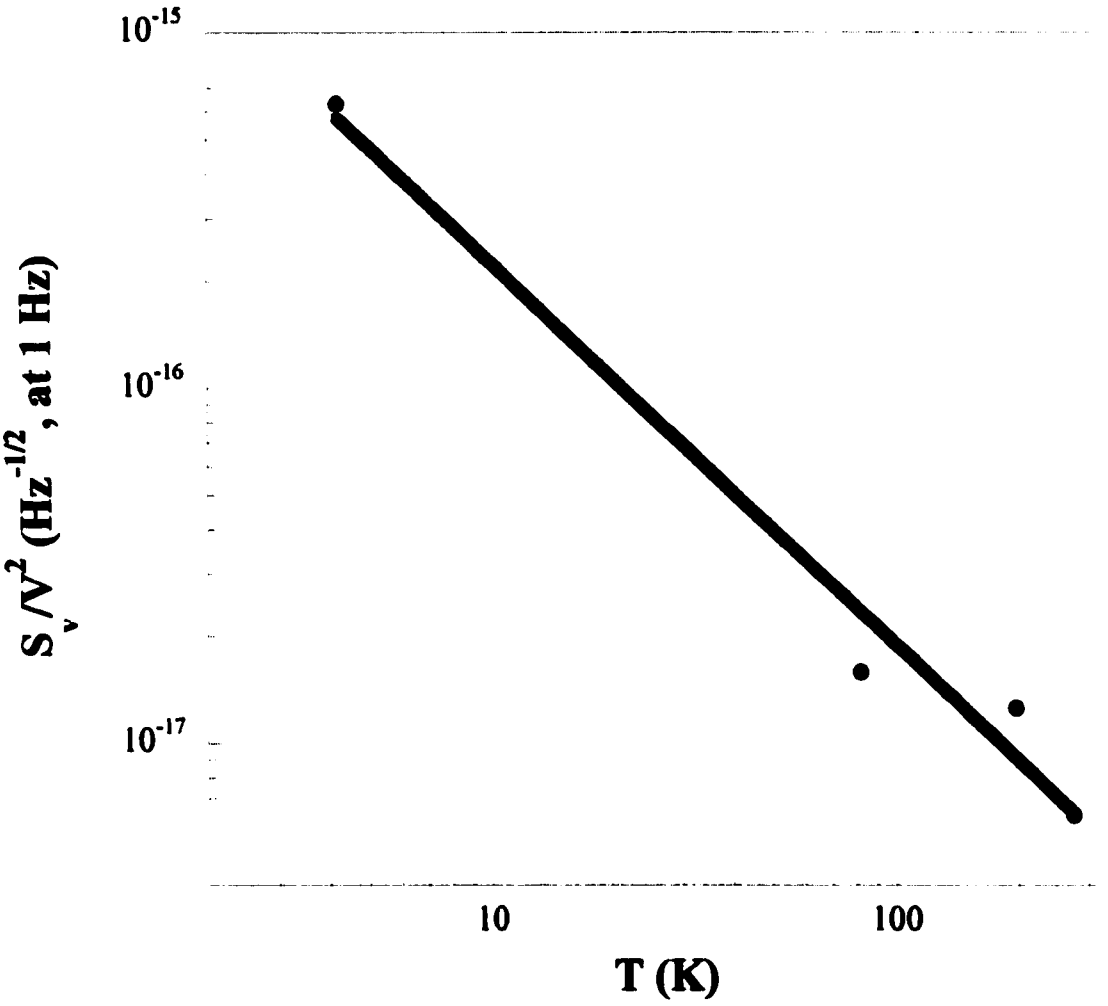

Figure 5. Noise (normalized to intensity at 1 Hz) at several stable temperatures follows $T^{-1.1\beta}$

In conclusion, the $1/f$ noise of carbon nanotube mats has been found to be extremely sensitive to the presence of oxygen. The removal of oxygen allows the noise to drop to a level set by temperature fluctuations. Nanotubes in good thermal contact with a reservoir should have noise low enough for applications.

CHAPTER 7

Search for shot noise in carbon nanotubes

Introduction to metallic nanotube devices

Metallic nanotubes have been the focus of intense research in the past five years. With only two conducting channels, they constitute truly one-dimensional objects of intrinsic interest. The peculiar features of these bands, including their symmetry and linearity, have been suggested to explain[136] the extremely long electronic coherence lengths that have been observed. Several groups have successfully fit transport data in nanotube devices with Luttinger liquid models.[137] But despite the wealth of data on such devices, there has been to date no observation of shot noise from carbon nanotubes. In this chapter I will briefly review the considerations from mesoscopic transport which make such an observation interesting. I will describe an experiment currently in progress which attempts to measure nanotube shot noise. The experiment is not only a search for shot noise, but a spectroscopic measurement of the variation of noise with frequency up to 1 GHz. Although this demanding task initially became important in order to distinguish shot noise from the excessive $1/f$ noise, I will first discuss the quantum transport physics that might be explored by shot noise before discussing this problem in detail. The second major impetus from Luttinger liquid physics will follow that exposition before I explain how I have attempted to measure shot noise.

Experiments with individual nanotubes were pioneered independently by several groups in 1996.[136,138,139] Typically a single nanotube or a small rope lies on a substrate, with two metal pads contacting it along its length. (See Fig. 1.) In these early devices, single-walled nanotubes synthesized by pulsed laser vaporization of graphite were suspended in dichloroethane. The dichloroethane was spun onto substrates of highly doped silicon covered with thick, smooth silicon oxide. After drying, these wafers could be examined with an atomic force microscope to locate individual nanotubes or small ropes. Using electron-beam lithography, metal leads could be patterned to connect the nanotube samples to large bonding pads.

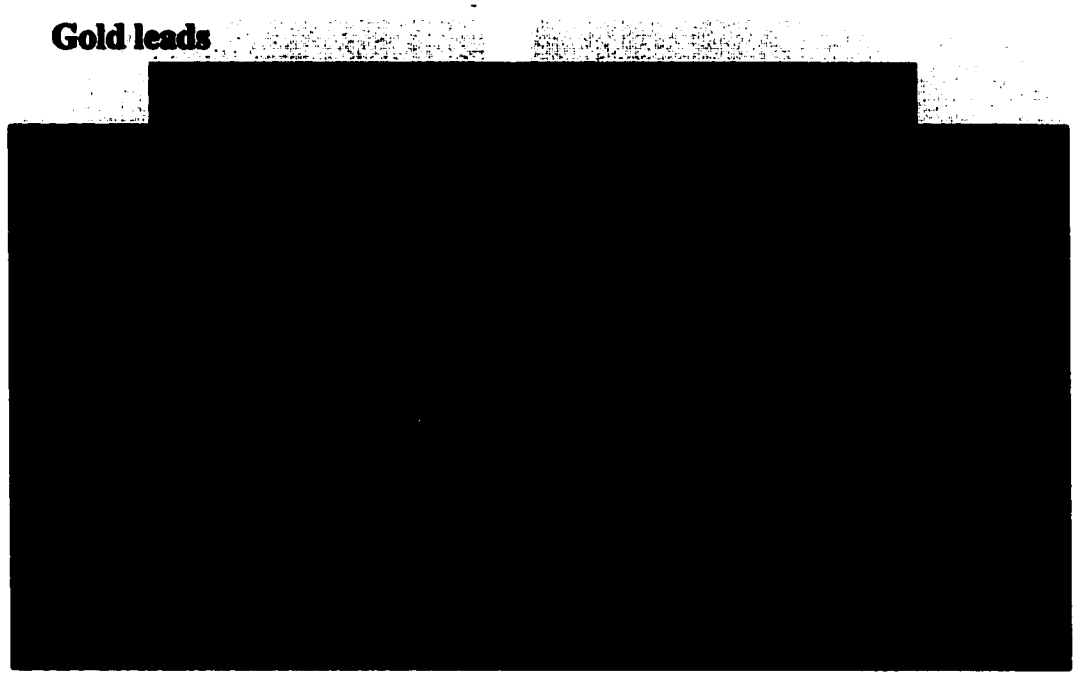

Figure 1. Schematic of a nanotube device. The nanotube lies on top of a layer of insulator. The gate underneath the insulator varies the charge on the nanotube, while the leads on top of the nanotube measure transport.

As the cross-sectional dimensions of a wire become smaller, the spacings between levels increase: $\Delta E \propto \frac{h^2}{4\pi^2 m L^2}$. In a metallic single-walled nanotube, two linear bands cross at the Fermi energy, and the nearest additional bands are 1 eV higher or lower in energy. In a 15 nm GaAs wire, by comparison, the level spacing is approximately 5 meV. The nanotube thus represents the experimentally accessible system that is the closest to one-dimensionality. The transport properties of nanotube devices is therefore amenable to analysis in the Landauer formalism.

As with many other phenomena, coherent transport in one-dimensional structures is extremely vulnerable to fluctuations, as pointed out by Abrahams *et al.*[140] The dependence of the resistance on the length of a structure is not $R \propto L$, as we would expect from classical physics, but $R \propto e^L - 1$. Nanotube devices have been measured with a variety of lengths and resistances. To determine whether such devices should be considered long or short requires a detailed analysis of the sources and strengths of disorder and scattering in nanotubes.

White and Todorov[141] suggested that because the two isolated bands at the Fermi energy are both rotationally symmetric, the effects of disorder are averaged with respect to nanotube circumference. Additionally, several authors[142,143] have argued that metallic nanotubes are insensitive to long-range disorder. This claim rests on the observation that the k_R and k_L states in a band have charge concentrated on one or the other of the two distinct atoms of the graphene basis. In a semiconducting nanotube whose electronic states are derived from slices near the K point, the overlap between these states is small; in an

armchair nanotube, the states are actually orthogonal. Long-range disorder potentials with wavevectors near zero are therefore not expected to couple very strongly to electrons near the Fermi energy.

Although some sources of scattering, such as acoustic phonons, may be suppressed by this mechanism, the influence of short-range disorder has not been thoroughly assessed. The significant effects of vacancies have been calculated by several authors;[144,145,146] certain varieties of defects are predicted to completely suppress conduction. Adsorbed gases are another source of short-range scattering potentials.[147] Electron-electron interactions, which constrain the length scale of ballistic transport in fabricated metal nanowires, are thought to cause Luttinger liquid behavior in isolated nanotubes.

There are thus several length scales to consider in interpreting experiments on individual metallic nanotubes, including the mean free path for inelastic scattering, for example phonon scattering and the mean free path for backscattering from a defect or adsorbed molecule. Coulomb blockade measurements in devices made from long nanotubes[121] have indicated that the mean free path for nanotubes in vacuum may be as long as a micron. Two-probe resistances as low as 6 KΩ have been obtained with short nanotubes;[148] these nanotubes are presumably shorter than the localization length.

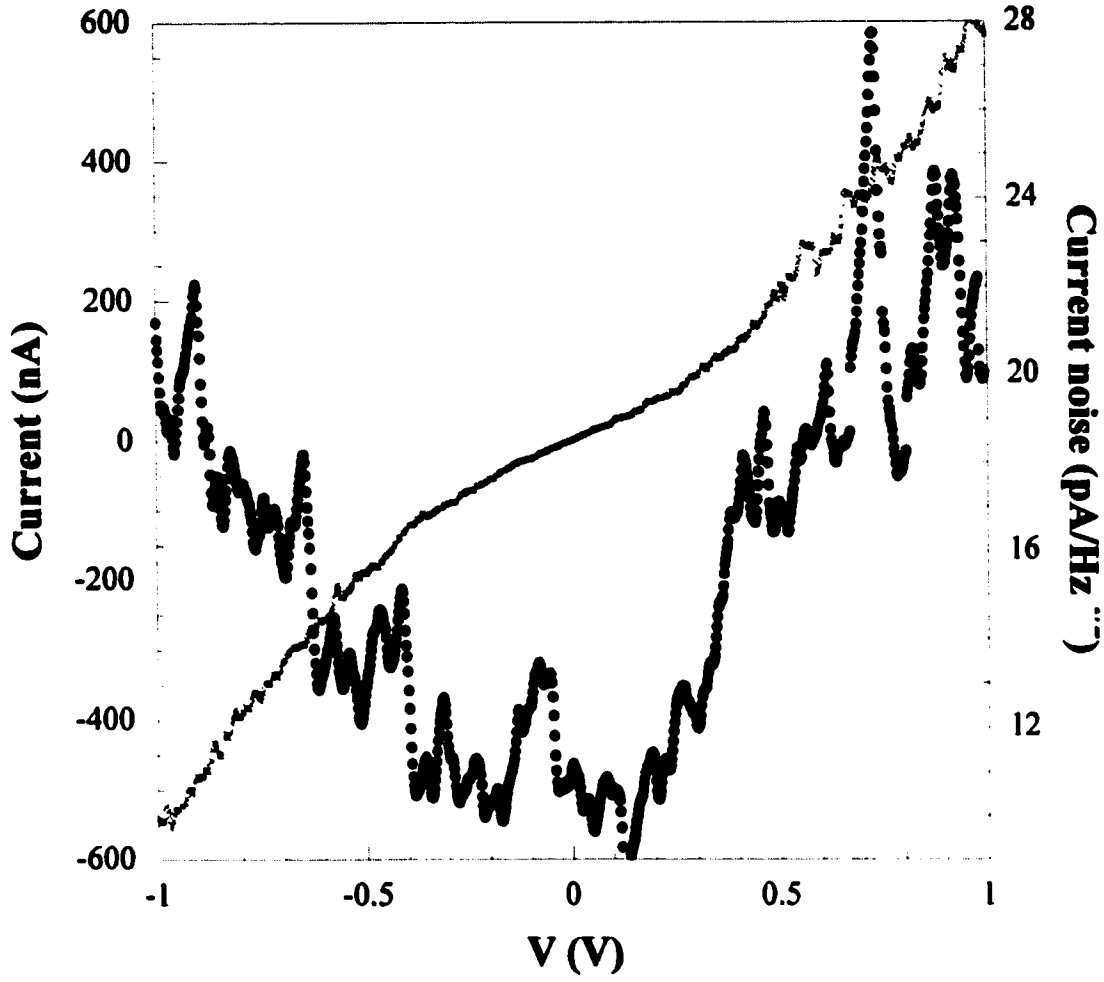

Figure 2. Noise at 2.3 KHz varies linearly with the current.

On the other hand, extremely large $1/f$ noise can be observed in conduction through a single nanotube in air (Fig. 2). It may be argued that this noise arises from fluctuations in the contact resistances and capacitances to a coherent electron device. But since the nanotube lies underneath metal contacts, it is difficult to understand why these connections fluctuate so dramatically. Given the observations described earlier about the oxygen sensitivity of nanotubes, and given that we are now discussing metallic nanotubes, it is

natural to ask if the noise might be due to time-dependent scattering from adsorbed gas molecules.

There are thus two pictures that emerge from the data on poorly contacted nanotubes. The observation of Coulomb blockade at low temperatures suggests that they should be regarded as quantum dots. On the other hand, anomalous $1/f$ noise is more consistent with a picture of one-dimensional systems that are localized by fluctuating disorder. Shot noise is a useful property that can distinguish these two models.

Introduction to shot noise

Shot noise was first observed in the thermionic current in vacuum tubes, and was explained by Schottky.[149] A number of equivalent derivations of the intensity of the noise have since been developed, but I will focus on the physical elements of the description. Let us imagine that the current consists of emitted electrons, each of which deposits a current pulse $i(t)$ at the anode. The integrated charge of the pulse is $q = \int i(t)dt$. In general the duration τ of each pulse is much shorter than observable times. An individual, isolated pulse can be detected with a narrow-bandwidth meter, such as a lock-in amplifier. During most cycles of the lock-in's reference wave, no current is present. Since the pulse is extremely short, it will be detected in one half-period of the reference wave of frequency f. Depending in which half-period it appeared, it is recorded as either q or $-q$ of charge, *i.e.* $2(q^2/T^2)$ of current intensity. (T is the length of time over which the measurement is made. The factor of two accounts for the fact that the rms value of the short pulse is the same as its amplitude.) This is true as long as the period of the reference is much longer

than the pulse duration. The mathematical form of these statements is that the Fourier transform $\hat{i}(f)$ of the current pulse $i(t)$ has the same intensity at all frequencies below $1/\tau$ and random phase. Now consider a stream of pulses with average rate I. Each produces a response in the lock-in detector, but because the phases are random, they add incoherently. The total current intensity from the random walk of lock-in responses is $\langle \delta I^2 \rangle = 2(q^2/T^2)N$, where N is the number of pulses in the measurement time T. The average current $I = q(N/T)$, so $\langle \delta I^2 \rangle(f) = 2qI(1/T)$, or $\langle \delta I^2 \rangle(f, \Delta f) = 2qI(\Delta f)$. Note that in performing the sum I have assumed that the current pulses are uncorrelated. The calculation predicts that classical shot noise will deviate from flatness at the frequency $1/\tau$. In a more detailed derivation this would turn out to be the current-current correlation time. The rolloff of shot noise at the correlation time distinguishes it from Johnson noise. Because Johnson noise is essentially blackbody radiation in a conductor, it rolls off at frequencies $f \sim kT/h$.

Because the shot noise depends directly on the charge of the current-carrying particle, it can be used to measure that charge. Several measurements of the electronic charge e were thus made. In recent years, charge discretization has been examined in a variety of many-electron systems. Tunneling through normal metal/superconductor junctions produces shot noise with Cooper pair carriers of $q = 2e$.[150] The cascade of multiple Andreev reflections in SNS tunneling features shot noise corresponding to Andreev clusters of carriers with $q = ne$.[151] As a more exotic example, the fractionally-charged com-

posite fermions in quantum Hall liquids have been observed for $q = \frac{1}{3}e$ and $q = \frac{1}{5}e$ by shot noise measurements.[152,153]

Quantum shot noise

What all these systems have in common is the restriction of current flow through a tunneling barrier. In such a circumstance the current can reasonably be regarded as a semiclassical flow of uncorrelated individual particles. Mesoscopic conductors can be small enough for this assumption to fail. In the Landauer-Buttiker picture of mesoscopic transport,[154,155,156] a mesoscopic conductor can be described by a coherent quantum mechanical wavefunction. Contacts to the conductor sample and modify that wavefunction by injecting carriers and adjusting the electrochemical potential. Consider a narrow conductor with only one available electronic band, henceforth called a channel or a mode, and no scattering. At the left and right ends of the conductors are two charge reservoirs with a bias voltage between them. All right-moving carriers in the conductor are assumed to exit into the right reservoir, and all left-moving carriers exit into the left reservoir. We can speak of two different chemical potentials in the wire, μ_R and μ_L, which are at equilibrium with the right and left reservoirs. The difference between them is the bias, $qV = (\mu_R - \mu_L)$. The net current is the difference in the currents of right- and left-moving carriers: $I = 2\frac{q}{2\pi}[\int v(k) f_R(k) dk - \int v(k) f_L(k) dk]$. (The initial factor of two counts the two spins.) To integrate over energy, the velocity factor cancels the density of states, so that $I = 2\frac{q}{h}(\mu_R - \mu_L) = 2\frac{q^2}{h}V$. This is the simplest version of the Landauer formula

for conductance. The special conductance $2\frac{q^2}{h}$, sometimes called the quantum of conductance, is equivalent to 12.9 $K\Omega$. In the presence of a single scattering center, the conductance formula is modified by imagining that carriers are reflected from the center with a probability R and transmitted with a probability $T = 1 - R$. The consequent mixing between left and right movers in the wire complicates the picture of the chemical potentials, but I will simply quote here the result that $I = 2\frac{q^2}{h}TV$. Occasionally the formula $G = 2\frac{q^2}{h}\frac{T}{(1-T)}$ is used. The conductance I have given in the text is the full two-wire conductance measured between the two reservoirs. This latter formula is the conductance of the scattering center itself, which is useful for calculating the conductance of a wire with several scatterers in series.

The shot noise in conduction through a coherent wire was first discussed by Lesovik.[157] Martin and Landauer discussed it in the framework described above and incorporated the finite-temperature Johnson-Nyquist noise consistently.[158] They calculated the zero-bias noise, the zero-temperature noise, and a third cross-term which can be important at finite temperature. The first term is the familiar conductance-dependent Johnson current noise, $\langle \delta I^2 \rangle = 4kTG$. The second term features an additional factor of $1 - T$: $\langle \delta I^2 \rangle = 2\frac{q^2}{h}T(1-T)V$. The cross-term is proportional to $\exp(-eV/kT)$.

For $T = 0$, the shot noise is zero; this is not surprising, because the current is also zero. For $T = 1$, the current is large, as specified by V, but the shot noise is still zero. Only for intermediate, partial transmission is there any noise. The key point is that for perfect transmission, $T = 1$, the right-moving and left-moving states respectively are always completely populated. The Pauli exclusion principle leaves no room for fluctuations in the flow of electrons. Since $I = 2\frac{q^2}{h}TV$, the formula can be rewritten $\langle \delta I^3 \rangle = 2\frac{q^2}{h}(1-T)I$. This suggests a view in which the effective charge is reduced by the factor $1 - T$ because current fluctuations must actually be carried by counter-propagating holes. Because the shot noise will always be in principle smaller than the full classical value of $2qI$, this type of noise is commonly called quantum shot noise.

In real mesoscopic conductors there are almost always multiple channels conducting in parallel. The extension of these arguments to multiple channels is complicated in detail but simple in concept. The current is $I = 2\frac{q^2}{h}(\sum T)V$, and the shot noise is $\langle \delta I^3 \rangle = 2\frac{q^2}{h}[\sum T(1-T)]V$. Again, we can rewrite the formula to compare to classical shot noise: $\langle \delta I^3 \rangle = 2\frac{q^2}{h}\left[\frac{\sum T(1-T)}{\sum T}\right]I$. What is apparent here is that although the majority of the current is carried by the channels with the best transmission, the majority of the shot noise is generated by those with the worst transmission. Shot noise can therefore be a sensitive probe for those weakly conducting channels which are hidden by dc

conductance measurements. This is not to say that they will always generate large amounts of noise; a noisy channel will be suppressed by $\frac{T}{\sum T}$, as it carries only a fraction of the current.

The use of shot noise to count a small number of channels was first carried out by Reznikov *et al.*,[159] who controlled the number of channels in GaAs 2DEGs by means of a gate. They observed strong suppression of the shot noise whenever the conductance equalled an integer times the quantum of conductance $2\frac{e^2}{h}$. Between the integer conductances the noise exhibited broad peaks. These peaks were centered, as expected, on half-integer values of conductance, where $T(1-T)$ has its greatest value. Van den Brom and van Ruitenbeek[160] used this technique to characterize a sample of unknown atomic gold contacts fabricated with break junctions. They observed a similar dependence of noise on conductance and counted the channels in their junctions accordingly. Recently, Scheer *et al.*,[161] combined this approach with multiple Andreev reflection shot noise to measure the complete set of complex transmission coefficients for an aluminum junction.

As a multimoded quantum wire becomes longer than the mean free path of the carriers, the shot noise might be expected to increase. The decrease in conductance cannot simply be modeled by an effective transmission, however. Several authors have examined the limit of diffusive transport, in which the sample is much longer than the elastic (*i.e.* impurity) scattering length. Beenakker and Buttiker[162] calculated that the shot noise assumes a universal magnitude, independent of sample geometry. If we write

$\langle \delta I^2 \rangle = 2q\alpha I$, they predicted $\alpha = 1/3$. Kozub and Rudin[163] extended this analysis to samples in which there is significant inelastic scattering. They found that in the presence of electron-electron scattering $\alpha = (\sqrt{3})/4$. The interesting departure of these calculations from $\alpha = 1$, as expected for $T \ll 1$, is due to the random distribution of transmission coefficients. In both cases, a certain fraction of channels remain essentially open, with T near 1. The noise is reduced because these channels carry much of the current. The first attempt to observe such universal behaviors, by Liefrink *et al.*,[164] was relatively imprecise, and could not distinguish between α of 0.3 or 0.4. Subsequently Henny *et al.*,[165] using carefully designed reservoirs to contact their gold wires, measured $\alpha = 1/3$.

It is important to explain the empirical fact that bulk samples of normal material do not generate shot noise at all. Wires rendered diffusive by impurity scattering or electron scattering may still be shorter than an electronic phase coherence length. As Kozub and Rubin pointed out, phonons destroy coherence, and suppress shot noise as well. De Jong and Beenakker[166] explained this neatly in terms of charge neutrality. A sample of size L which is much larger than the phase length l_φ can be thought of as comprising $N = L/l_\varphi$ regions of coherent transport. Within each region, the current I flows, generating noise currents of $\langle \delta I^2 \rangle = 2q\alpha I$. It is the voltage noise of the various regions which add: $\langle \delta V^2 \rangle = \sum \langle \delta v^2 \rangle = \sum \langle \delta I^2 \rangle r^2$. If each region has resistance $r = R/N$, the current noise of the entire sample is $\langle \delta I^2 \rangle = \sum \langle \delta I^2 \rangle \frac{1}{N^2} = 2q\alpha I \frac{1}{N}$. The incoherent addition of

the fluctuations suppresses the shot noise by a factor L/l_φ that can be very large for a macroscopic conductor.

The shot noise in well-contacted individual nanotubes should be fairly simple. Consider the noise for nanotube devices with increasing values of resistance. At zero scattering and perfect contacts, the two channels have a total (contact) resistance of 6.47 KΩ, and the noise is zero. Some scattering will increase the resistance, and can be modeled by sites of $T < 1$. As the transmission gets worse, the shot noise increases towards its full classical value. For nanotubes larger than the phase length, which roughly corresponds to resistances much larger than 6.47 KΩ, the noise decreases again to the zero value expected in a bulk conductor. Departures from this behavior might be seen in devices made from multi-tube ropes. The distribution of transmission among the ropes should lead to a series of broad peaks in the noise in ropes shorter than a few scattering length and a plateau of $1/3$ shot noise before the bulk-material rolloff in longer ropes.

Shot noise in coherent tunneling

Different behaviors are observed in poorly contacted nanotubes. If tunneling contacts are applied to each end of a coherent electron system, resonant tunneling is commonly observed.[167] In the finite-length object between the tunneling contacts, the energy level spacing is approximately $\frac{h}{2\pi}\frac{v_F}{L}$. As the bias voltage is increased from zero, the energy levels in the object are shifted downward with respect to the Fermi level of the source. At some bias the Fermi level is aligned with an energy level, and there is large current flow. As the bias is increased, the energy level is lowered beyond the Fermi level, and the cur-

rent decreases. This phenomenon has been observed in nanotubes[136] together with the associated Coulomb blockade in which the small nanotube capacitance can be observed. Bockrath *et al.* fit their current-gate voltage data with the relation $U = 1.4\text{eV}/L(\text{nm})$.

The theory of the shot noise of resonant tunneling devices has been discussed extensively.[168,169] Between conductance peaks, the tunneling is classical, and the shot noise reaches the full classical value. At the conductance peaks, the noise is generally smaller, but depends on the details of the tunneling barriers, the temperature, and any small incoherence in the device. Most noise observations have been dominated by random telegraph noise.[170] But Sasaki *et al.*,[171] measuring at 10 MHz, showed that the noise does oscillate between $\alpha = 1$ and $\alpha \approx 0.2$ as the conductance is swept through Coulomb peaks.

Nanotubes differ from ordinary resonant tunneling systems in that they are one-dimensional.[137] The breakdown of Fermi-liquid theory in one dimension leads to the formation of a different, correlated ground state, the Luttinger liquid, which has been well reviewed by Voit.[172] The differences between the two electronic liquids is most easily observed in the low-lying excited states. In a Fermi liquid these are a continuum of charged, fermionic quasiparticles with states lying arbitrarily close to the Fermi level. Above a Luttinger liquid there is a soft power-law gap in the density of states, and the excitations are separate spin and charge particles. All observations of Luttinger-liquid behavior in nanotubes thus far have been essentially tunneling measurements of the density of states, interpreted with a simple plasmon model proposed by Kane, Balents, and Fisher.[173] The ingredients are the charging energy, which models the Coulomb interaction and the level spacing delta.

The plasmon model calculates the Luttinger coupling constant g as $g = \left(1 + 2\frac{U}{\Delta}\right)^{-1/2}$).

The shot noise of Luttinger liquid tunneling has been calculated by a number of authors.[174,175,176] The zero-frequency behavior is relatively simple. An electron-like quasiparticle entering from the normal-metal leads injects a cloud of spin and charge excitations into the Luttinger liquid. The interaction renormalizes the charge of the excitations, so that $\langle \delta I^2 \rangle = 2(ge)I$. Note that the noise depends directly on I. Since the non-equilibrium current $I \propto V^{2/g-2}$, the combined measurement of shot noise and current as a function of voltage should provide a rigorous test for Luttinger liquid behavior.

There are several sources of possible structure in the shot noise spectrum. The interactions responsible for the Luttinger liquid introduce quantum corrections to the shot noise with a frequency scale $\omega_0 = 2\pi g\frac{eV}{h}$. Chamon *et al.* calculated the first-order correction[175] to be $4\pi g(2g-1)^2\left(\frac{I}{\omega_0}\right)^2\omega$. In nanotube devices conducting nonlinearly, conductances are typically about 10 μS.[137] At a frequency of 1 GHz, this correction will therefore be about 1×10^5 times smaller than the classical shot noise. A second time scale is the length of the current pulse, which I introduced in the discussion of vacuum tube shot noise; near this scale the shot noise deviates from a white spectrum. As Ponomarenko[177] observed, this should be the time that the particle takes to traverse the Luttinger liquid. Nanotubes provide an unusual opportunity to observe the correlation-induced rolloff of shot noise. Because the interaction strength U comes from the geometry via the capaci-

tance, the ratio U/Δ and the coupling strength are independent of the length of the nanotube. Nanotube devices 10 μm long can be fabricated. The traversal frequency at the Fermi velocity, 5×10^5 m/s, should be 50 GHz. The Fourier transform argument can be used to estimate that the noise at 2 GHz should be reduced by 0.2%, which is just within the experimental resolution. When devices are operated in their current-limited regime,[125] it has been suggested that a charge density wave is formed due to the interaction of optical phonons. The pinning of this charge density wave would provide a third, unknown frequency scale at which narrow-band sliding noise might be observed.

Device fabrication

These experiments used an integrated chemical vapor deposition approach developed by the Dai group at Stanford University.[178] Devices were fabricated in the Microlab at the UC-Berkeley Department of Electrical Engineering and Computer Sciences. All lithography was performed using the JEOL 6400 scanning electron microscope and Nanometer Pattern Generation System in the Microlab, using either PMMA 950 weight monolayer or MMA/MMA under PMMA bilayer resists. Both were diluted to 5% in anisole. The recipes were: for single layer, PMMA was spun on at 4000 rpm for 45 seconds and then cured at 150°C for an hour. For bilayer, MMA/MAA was spun on at 4000 rpm for 45 seconds and cured, then PMMA was spun on at 6000 rpm for 45 seconds and cured. For highest resolution, monolayer resists were exposed to 400 μC/cm2, bilayer resists to 250 μC/cm2 for highest resolution. Both resists were developed in 1:5 MIBK in IPA

solution for 60 s. Metal films were deposited in the v401 thermal evaporator; both alignment marks and contact pads comprised 3.5 nm chromium sticking layers beneath 30 nm gold films.

Figure 3. Micrograph of a typical CVD-fabricated device. The image is an overlay of an SEM image of the nanotubes and catalysts and an optical micrograph made after the metal leads were deposited.

Alumina-supported, nanocrystalline transition metal catalysts were synthesized according to the prescription of Cassell *et al.*[179] and used to fabricated devices by the recipe developed at Berkeley by Jeff Gore. The catalyst particles were suspended in salt solu-

tion in bulk quantities. To fabricate a chip with nanotube devices, small gold alignment marks were patterned using a standard liftoff process. I began by patterning small gold alignment marks using a standard liftoff process. (The metal film covering the reist was removed in a continuous sheet by dissolving the resist for an hour in acetone.) Then, without aligning the SEM, an array of holes in resist were patterned for catalyst deposition. The bulk catalyst solution was sonicated for a minute, and a drop was placed on the substrate. After the water was dry to the eye, the wafer was placed in a 175°C oven for fifteen minutes. This step presumably sintered the nanoparticle catalyst to the substrate; without it the catalyst did not stick to the wafer. After the oven cure, the substrate was soaked for two hours in dichlorethane to remove the resist and the particles atop it.

Nanotubes were grown by catalytic decomposition of methane.[179] The substrate with patterned catalyst was placed in a tube oven. Under argon flowing at 3 sccm, it was heated quickly to 900°C. Once the temperature had stabilized, the argon was stopped and replaced by methane flowing at 900°C. After ten minutes, the methane was stopped and replaced by argon, and the substrate was cooled by turning the oven off. Nanotubes were observed sprouting from the catalyst islands. Most nanotubes were only a few microns long and fairly sharply curled, but a few nanotubes were tens of microns long and relatively straight. Figure 3 shows a completed nanotube device.

Noise experimental methods

The basic noise circuit, diagrammed in Fig. 4, contains the sample and a current-sensing resistor. The behavior of the circuit can be modeled by assuming that a nearly ideal

generator sources a voltage V_a in series with a resistance r V_a. contains only a dc and a low-frequency ac component, and has zero rf intensity. The sample resistance R_s is in series with this voltage source and the current sense resistor R. A small stray capacitance C_x shunts the resistor to ground. The noise current generated by the sample can be modeled by an equivalent current source is in parallel with the sample. Because the voltage source V_a is ideal, the rf behavior of this circuit can be calculated with the voltage source V_a replaced by simply its rf impedance r. A simple calculation reveals that the voltage developed across the resistor R is $\langle \delta V^2 \rangle = \langle \delta I^2 \rangle \left(\frac{R_s R}{R_s + R} \right)^2$.

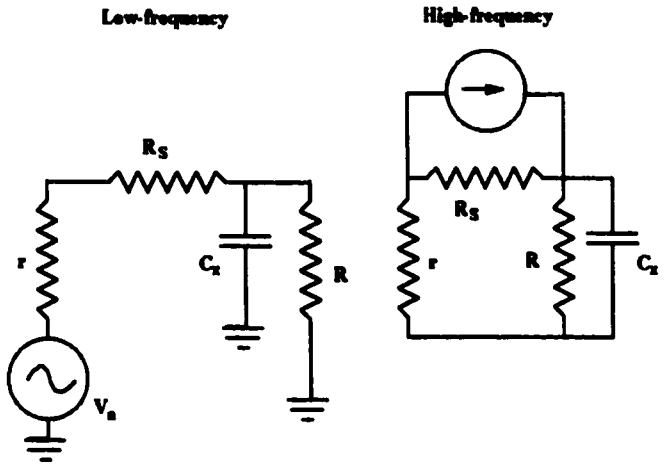

Figure 4. The basic noise circuit has different characteristics at dc and at rf frequencies.

Background noise

The most significant additional source of noise is Johnson noise in the current sense resistor. The intensity of thermal noise increases only linearly with R, so larger resistors have better shot noise to thermal noise ratios. Rf measurements are restricted essentially to 50 Ω resistors. The rms thermal noise in a 50 Ω resistor at 4 K is 0.1 nV, which is equivalent to -186.6 dBm. (The most common unit for rf signal levels is dBm. 0 dBm = 1 mW. In a 50 Ω system, 0 dBm = 220 mV.) By contrast, the rms voltage due to full classical shot noise from 1 μA of current in the same resistor would be 30 pV (-197.3 dBm), which is smaller than the thermal noise! In order to measure smaller quantities of noise or the current dependence of noise, let us suppose that it is necessary to be able to detect the full shot noise from 10 nA. The 'signal-to-noise' ratio is then 1/35 (31 dB).

An additional source of noise is the $1/f$ noise, which may be due to random telegraph noise. The mechanism would be the fact that an instantaneous switching of the resistance, as has been observed in a number of mesoscopic systems,[170] has a Fourier spectrum proportional to $1/f$. This argument is analogous to the way that white shot noise results from the Fourier spectrum of a current spike. Typically the switching states have been observed to have lifetimes between 10 μs and 10 ms. The rf measurement samples only one at a time; in other words, it is beyond the rolloff of the Fourier spectrum. If the $1/f$ noise has some other source but does in fact decrease as $1/f$, the measurements depicted in Fig. 2 imply that it should subsume into the 50 Ω thermal noise at about 5 MHz.

Figure 6 shows a conceptualized spectrum, in which the $1/f$ noise decreases until it

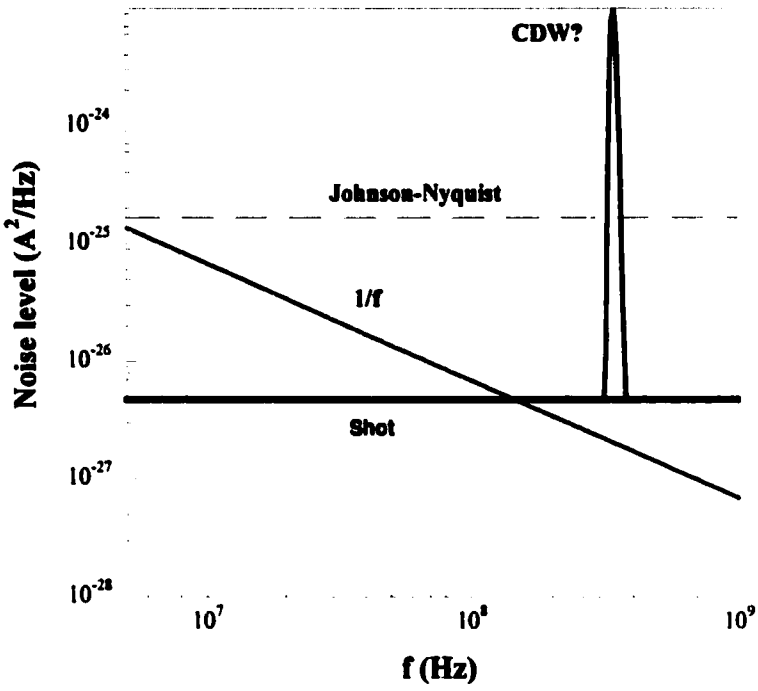

Figure 5. Imagined contributions to the noise spectrum.

reaches the thermal floor. At these frequencies there may be some interesting behavior due to random telegraph noise. At higher frequencies there is flat thermal noise, with a much smaller shot noise component below it. The shot noise may be flat, or it may vary with frequency according to a Luttinger-liquid power law.

Finally, interference from the environment must be avoided. The dewar in which the sample and rf circuit are mounted on the end of a probe also serves as a metallic enclosure. The two lines of semi-rigid coaxial cable are soldered through the top flange of the dewar. All signals but the rf signal pass into the dewar pass through pi filters in rf shielded boxes. (The rf signal is connected entirely through continuous-ground rf connectors and cable.) Several remaining holes, such as the cryogen filling port and the feedthrough for the level

meter, are capped with copper foil. The pumping port is shielded by a copper mesh soldered across its cross section. The isolation achieved by these methods was verified with a spectrum analyzer to leave less than −180 dBm/Hz at most frequencies and less than −80 dBm at specific frequencies, such as the 100 MHz FM radio band.

The small signal is detected using an approach adapted from the measurement by Reznikov *et al.*[159] The total noise can be detected with a power meter of some sort. The output of this meter will fluctuate; the spectral density of these fluctuations is the same as the density of the underlying noise. This is a fundamental property of Gaussian noise.[180] The output of the power meter can be averaged, so that the fluctuations have a bandwidth much smaller than the bandwidth of the power being sampled. Let the noise spectral density be S; the rms power detected is $V \propto S\Delta f$, where Δf is the bandwidth of the meter. The rms fluctuation is $\delta V \propto S\Delta\omega$, where $\Delta\omega$ is the bandwidth of the averager or filter. So S is detected as $S = \frac{V}{\Delta f}$, and the uncertainty in S is $\delta S = \frac{\delta V}{\Delta f} = S\frac{\Delta\omega}{\Delta f}$.

The Reznikov method detects shot noise as long as the shot noise is greater than δS. The shot noise and the thermal noise differ in that the former varies with current. Let the current varies as a slow sine wave of frequency omega. A lock-in amplifier can discriminate the dc value of S, which is determined by the thermal noise, from the component at omega, which is dominated by the shot noise. Since the shot noise is coherent with respect to the slow sine wave, a decrease of $\Delta\omega$ does not change its contribution to the ω component. Thermal noise power fluctuates randomly and incoherently with respect to the sine wave, and a decrease of $\Delta\omega$ averages away these fluctuations.

Implementation

Nanotube samples are most likely to have much greater resistances than 50 Ω , of magnitude 10 KΩ or more. The voltage equation can thus be simplified to $\langle \delta V^2 \rangle = \langle \delta I^2 \rangle R^2$, as long as several other assumptions hold true. First, the rf impedance of the voltage source must be considerably smaller than the sample resistance. This is a restatement of the condition that the voltage source is ideal, producing zero voltage at rf frequencies. This condition is achieved simply by placing rf pi filters in series with the dc voltage source.

The second requirement, that on the stray capacitance, is more stringent. The shunt impedance must be greater than R, for all frequencies of interest. For a 50 Ω resistor and a 1 GHz upper frequency, this implies that $C < 2$ pf. There are several sources of stray capacitance. The wire bonding pads on the samples are typically 100 μm across. They form capacitors with the metal-like silicon substrate through 1 μm of silicon dioxide dielectric. These capacitors are 0.3 pf each, so that the shunt capacitance across the sample is 0.15 pf. The more difficult problems come from objects such as the chip carriers, with pin-to-pin capacitances of 3 pf, and the sealed vessels described in the previous chapter, with pin-to-pin capacictances of 16 pf. These capacitances are eliminated by a special sealed vessel. The vessel has three commercial wire-glass brazed electrical feedthroughs, which are glued to the copper body of the vessel with silver epoxy. The large thickness of dielectric gives these feedthroughs capacitances less than 2 pf. The sample sits on an alumina plate with three gold sockets glued upside-down on its sides.

These sockets plug onto the wires protruding from the feedthroughs. Before an experiment, wires must be attached between the sample and these gold pins.

Two of the three feedthroughs are connected through the pi filters to gate voltage and bias voltage. The third, which is used as the drain, has a female SMA connector. From this point on the signal is carried entirely by rf cable and components. The cable is UT-141 type cable with an outer conductor of 0.141" outer diameter beryllium copper for low losses. Its impedance of the semi-rigid coaxial cable is 50 Ω, real, over a wide band in the rf but its impedance at dc is infinite. The current sense resistor (and dc current return) is provided by a 50 Ω termination connected to the signal path through a tee. (The termination has a resistance of 50 Ω at 78 K and 68 Ω at 5 K.) The other arm of the tee is connected through a bias tee to the input of the first stage amplifier. The bias tee contains an inductor and a capacitor, which split the dc and rf components into different paths. The dc signal, which measures the average value of the current, returns through UT-141 cable and a pi filter. The rf part is connected to the input of the first amplifier. The rf representation of this configuration is just as in the diagram. Unlike the situation normal in dc measurements, the amplifier does not have approximately infinite input impedance, but approximately 50 Ω input real impedance. Since the effective impedance of the two components in parallel is 25 Ω , the shot noise signal (and the thermal noise signal) will be decreased by a factor of two.

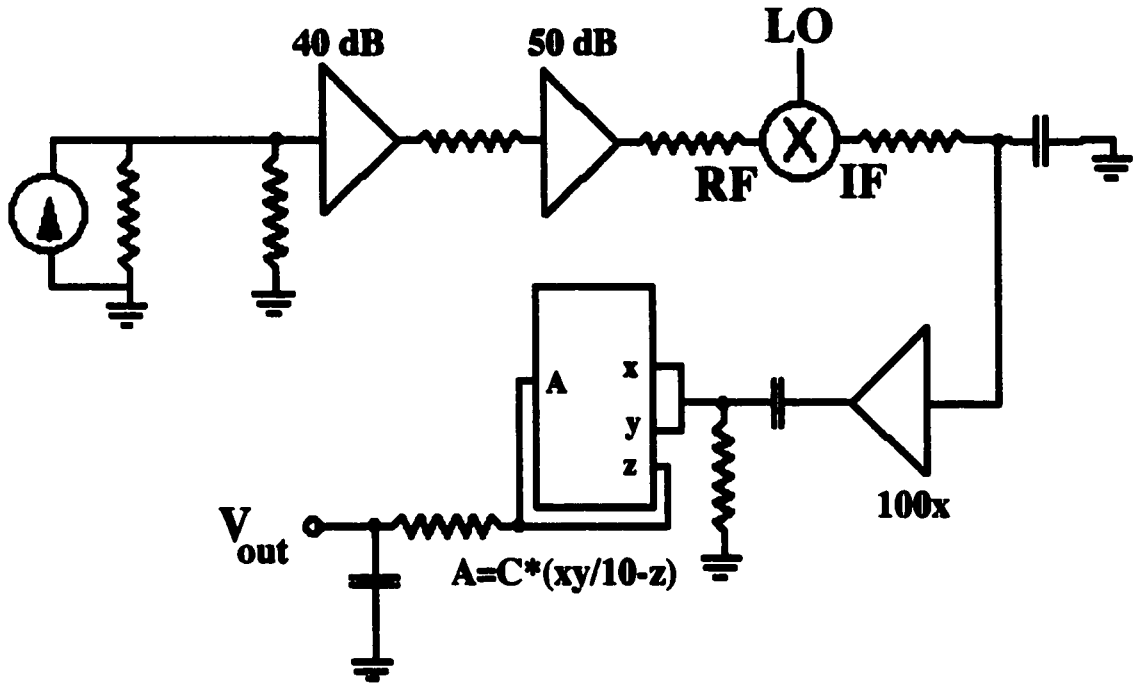

Figure 6. Diagram of the components in the rf shot noise circuit. The 50 dB amplifier is the first component that is not kept cold.

The amplifier features a gain of 41 dB over a bandwidth from 100 Mhz to 2 GHz. Its low noise figure of 0.9 dB improves considerably when it runs at low temperatures; it is rated for 0.25 dB at 77 K. Its effective noise temperature at 77 K is 18 K. This produces the floor of thermal noise against which the lock-in averaging must discriminate. Its output is connected through 8 dB of attenuators to a second amplifier situated at room temperature. The role of the attenuators is to prevent ringing, which can result from small impedance mismatches in the two amplifiers. They are kept at the same temperature as the first amplifier to reduce their contribution to the thermal noise. The second amplifier has a gain of 50 dB and a noise figure of 1.5 dB over a bandwidth from 1 MHz to 1 GHz. At its

output is another attenuator, which prevents ringing from the mismatch of the amplifier and the detection system.

The signal at the output of the amplification system can be detected in several ways. The integrated intensity over the entire 1 GHz bandwidth can be measured with a commercial diode detector. If the sample is maintained at 77 K, the thermal noise of −173.7 dBm/Hz is amplified to −6 dBm rms power. A spectrum analyzer, such as the HP 8558B, can be used to inspect the output of the amplifiers in detail. For quantitative spectral measurements by lock-in averaging a purpose-built detection circuit is used. The output from the amplifiers is fed to the RF port of an rf mixer. The LO port of the mixer is driven by a 13 dBm signal of user-specified frequency f from a signal generator (HP 8656A). Noise signal components with frequencies near f are split at the IF port into down-shifted parts with frequencies nearly zero and up-shifted parts with frequencies near 2f. The down-shifted half is selected by a 1 MHz filter (50 Ω real, single-pole RC) following the mixer.

At this stage the magnitude of the thermal noise, decreased by the mixing, is approximately −100 dBm/Hz, or $2\mu V/Hz^{-1/2}$. The shot noise is approximately $20nV/Hz^{-1/2}$, which is smaller than the noise in the power meter. The signal is therefore stepped up by a Stanford 530 1 MHz programmable gain preamplifier ($4nV/Hz^{-1/2}$ input noise). Typically the amplifier is set to a gain of 100. The dc component of the noise is removed by a 10 KHz, two-pole, high-pass filter incorporated in the commercial preamplifier box. This step is important; it prevents the output of the amplifier and the input of the detector from being overloaded by spurious dc signals. It affects the analysis relatively little, as the

bandwidth of detection 1 MHz is much larger than the 20 Khz slice of spectrum that is removed from the center.

The power meter is a square-law detector, at the core of which is a multiplier opamp with 10 V reference and $1\mu V/Hz^{-1/2}$ output noise. After the Stanford preamp, the noise is filtered again by a 1 MHz filter and applied to both inputs of the opamp, The output voltage of this circuit, $V_{out} = V^2/(10V)$, is filtered again (low-pass, 1 KHz), and this final signal is proportional to the noise in a 1 MHz band centered on frequency f. The signal can be watched on an oscilloscope or measured with a dc voltmeter or a lock-in.

Most of the circuit is transparent to the analysis, because it treats thermal noise and shot noise the same. Imagine a sinusoidal rf voltage with an amplitude equal to the rms noise voltage: $V(t) = A\sin(2\pi ft)$. The amplitude is given by $A = G[4kTR + 2R^2\alpha qI_0 + 2R^2\alpha qI_1\sin\omega_0 t]^{-1/2}$. The gain G bundles together all the amplitude-changing effects, including amplifiers, attenuators, mixer losses, the preamplifiers, and the squarer reference, with the fixed bandwidth Δf of about 1 MHz. The first term represents the thermal contribution to the noise and the second is the shot noise due to the dc sample current. The third term, the shot noise from the ac sample current, is the quantity of interest. The effect of the mixer is to shift f by f_0, where f_0 is not quite equal to f. The input to the squaring circuit is $V_{in}(t) = A\exp(-j2\pi f_1 t)$, where $f_1 = f - f_0$. The remanent frequency f_1, which is passed by the 10 KHz high-pass filter, is still large compared to 1 KHz and ω_0. The output of the squaring circuit is

$$V_{out} = \frac{A^2}{10}(\sin 2\pi ft)^2 = \left(\frac{1}{2} - \frac{1}{2}\cos 4\pi ft\right)\frac{G^2}{10}[4kTR + 2R^2\alpha qI_0 + 2R^2\alpha qI_1 \sin\omega_0 t].$$

After the low-pass 1 KHz filter removes the high-frequency part, the output voltage has an ac part that is $G^2/2$ greater than the ac current's shot noise. This analysis is unrealistic in the sense that the actual rf signal is not sinusoidal but a complex, fluctuating signal with a Fourier intensity given by A. The simple discussion here represents the correlations between the phases of Fourier components within a few ω_0 of f by bundling them all into a single component.

The 'power transamplification' $G^2/2$ can be estimated by cascading all the known components to be 5×10^{15} VHz/mW. The thermal noise at 77 K of −174 dBm/Hz produces an output of 20 mV. In practice this is an extremely inaccurate way to measure the shot noise. Each component differs from its nominal gain or loss by as much as 2 dB; in the rf stages these differences vary with frequency. Figure 7 shows the result of measuring the shot noise in a standard diode. The extent to which the spectrum is not flat, or white, reflects the tolerances of the components. The shot noise is actually measured by calibrating the system with a known noise source. This is effected most easily by measuring the voltage simultaneously with a dc voltmeter and a lock-in tuned to ω_0. The dc component of the output voltage actually contains a shot noise contribution. Since this is usually much smaller than the thermal noise, it can be ignored for this calibration. If necessary,

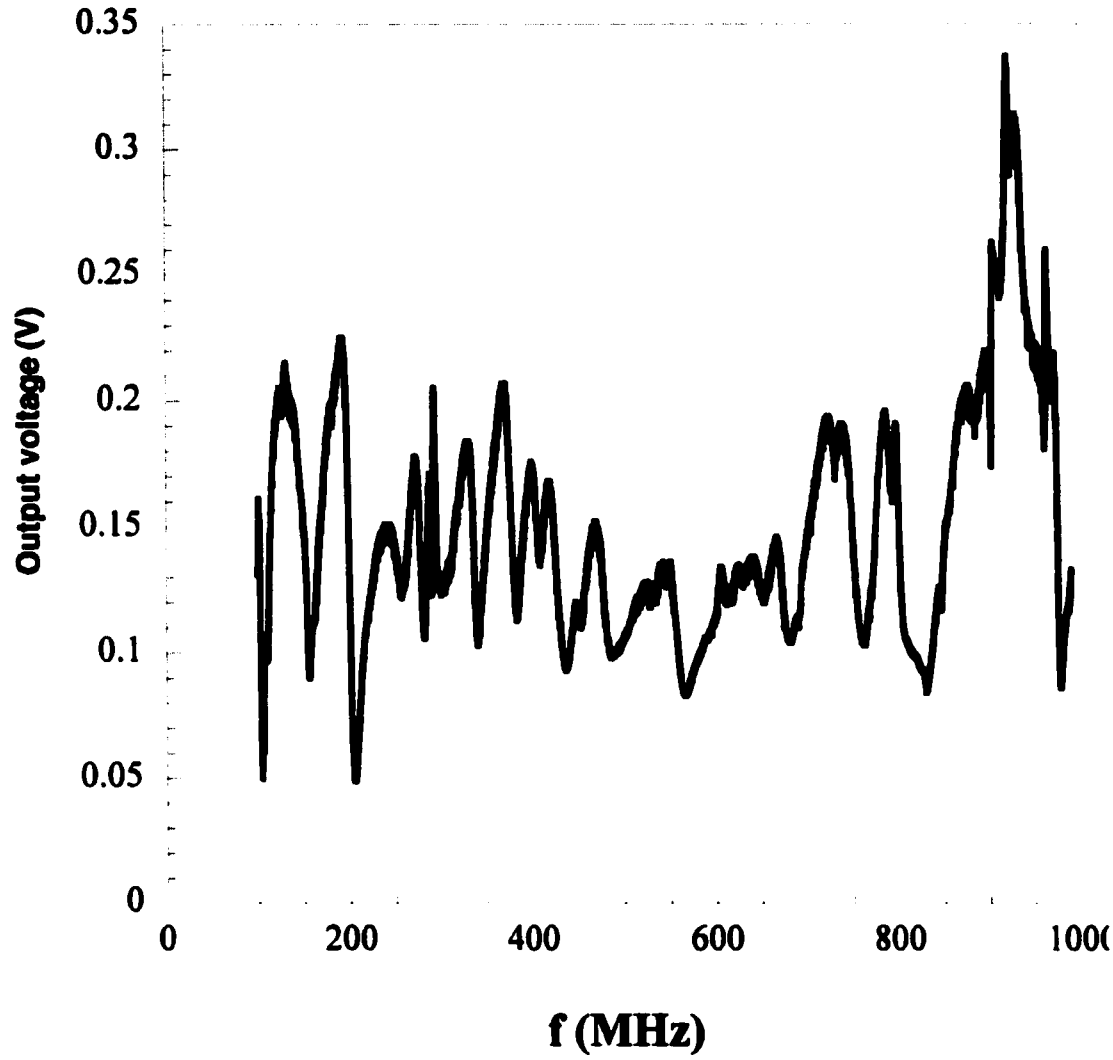

Figure 7. Output voltage from the shot noise of a diode.

the sample current can be turned off to measurethe thermal noise voltage. The output voltage spectrum in Fig. 7 varies around the level expected from the known gains. To measure shot noise, the ac voltage spectrum is divided by the dc voltage spectrum and multiplied by the known thermal noise.

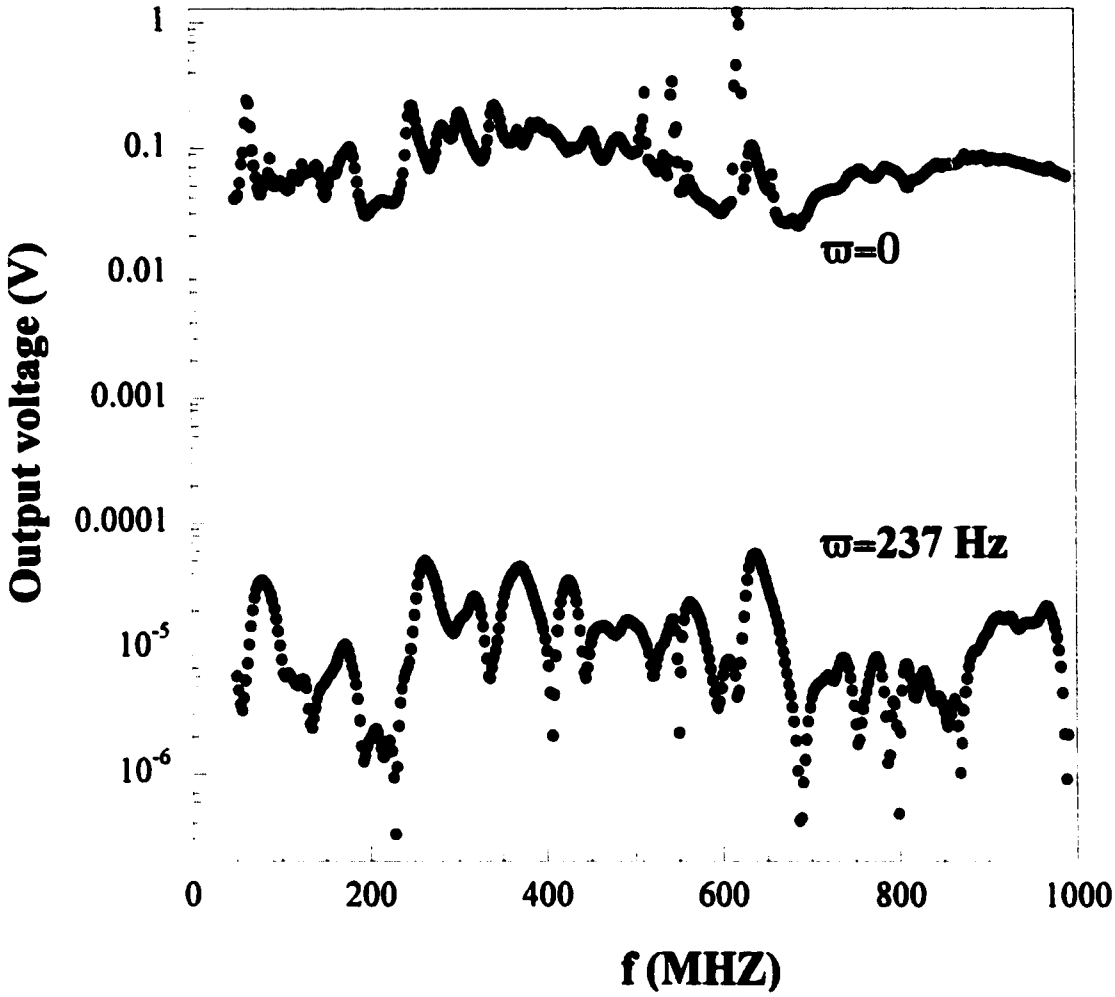

Figure 8. "Shot noise" and thermal noise measured simultaneously by two different instrument. The ratio between is the magnitude of the thermal noise rejection.

The first measurement has been performed with this apparatus. Figure 8 shows the shot noise measured with 0.44 μA of current in a nanotube device. In the same plot the upper curve is the thermal noise floor measured at the same time with a dc voltmeter. In this particular device, the apparent shot noise is the floor of background noise achieved by my suppression technique; the spectrum is the same with and without current actually flowing. The device features zero shot noise within the uncertainty of the experiment;

$\alpha < 1/15$. In Fig. 9, the noise spectrum is shown in terms of α. In the inset, the I-V characteristic for this device indicates that it is an extremely high resistance sample. The absence of tunneling noise indicates that it is not behaving as a resonant tunneling device. In the framework of noise possibilities that I have discussed, this device seems to be in the high-resistance localized regime. The scattering length in this device must be considerably less than the electrode separation of 1 micron.

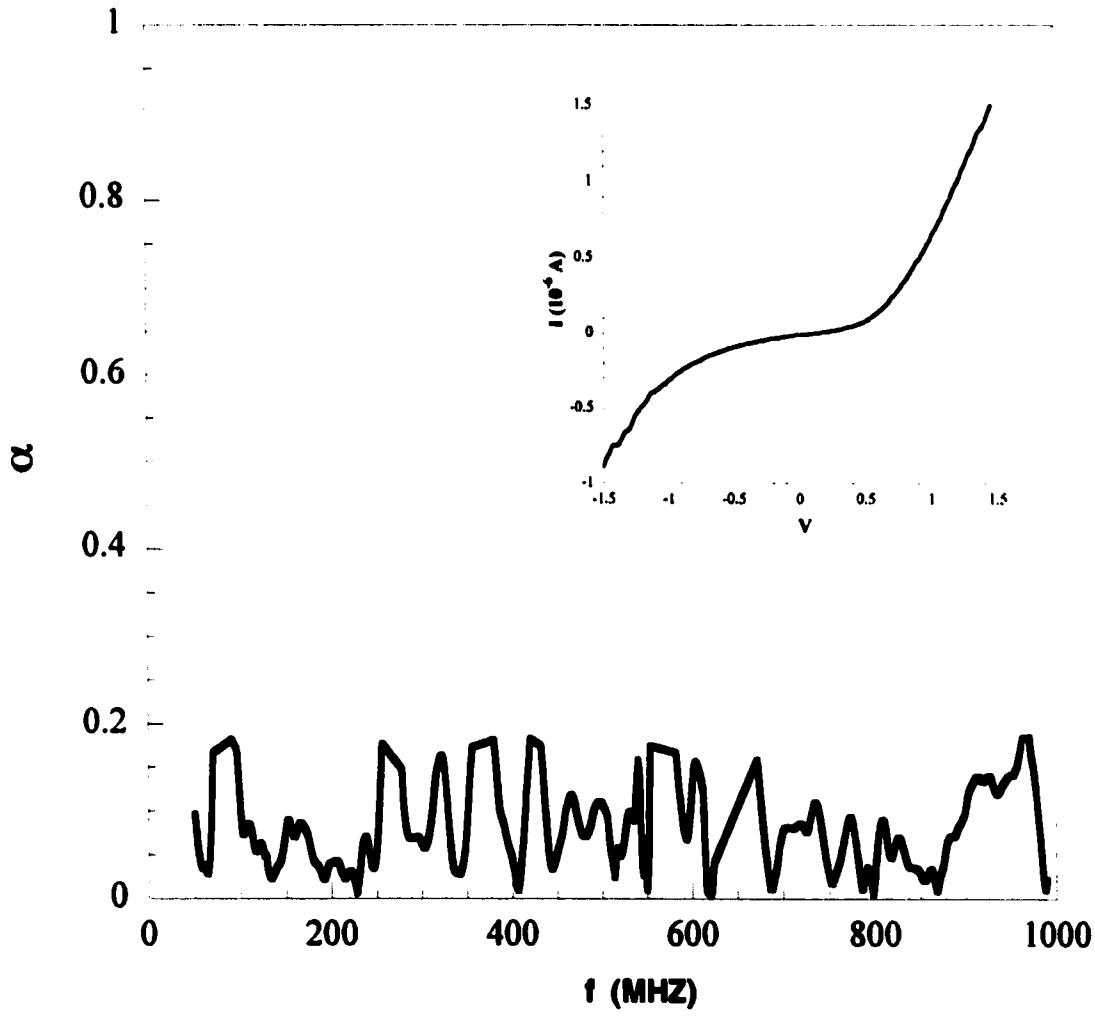

Figure 9. Example spectrum of reduction factor α, showing the sample depicted in the inset has no detectable shot noise.

Bibliography

1. C. Zener, *Physical Review* **82**, 403 (1951).

2. R. von Helmolt, J. Wecker, B. Holzapfel, L. Schultz and K. Samwer, *Physical Review Letters* **71**, 2331 (1993).

3. S. Jin, T. H. Tiefel, M. McCormack, R. A. Fastnacht, R. Ramesh and L. H. Chen, *Science* **264**, 413 (1994).

4. J. A. M. van Roosmalen, P. van Vlaanderen, E. H. P. Cordfunke, W. L. Ijdo and J. W. Ijdo, *Journal of Solid State Chemistry* **114**, 516 (1995).

5. Q. Huang, A. Santoro, J. W. Lynn, R. W. Erwin, J. A. Borchers, J. L. Peng and R. L. Greene, *Physical Review B* **55**, 14987 (1997).

6. J. Topfer and J. B. Goodenough, *Journal of Solid State Chemistry* **130**, 117 (1997).

7. T. Proffen, R. G. DiFrancesco, S. J. L. Billinge, E. L. Brosha and G. H. Kwei, *Physical Review B* **60**, 9973 (1999).

8. J. Rodriguez-Carvajal, M. Hennion, F. Moussa, A. H. Moudden, L. Pinsard and A. Revcolevschi, *Physical Review B* **57**, R3189 (1998).

9. Y. Murakami, J. P. Hill, D. Gibbs, M. Blume, I. Koyama, M. Tanaka, H. Kawata, T. Arima, Y. Tokura, K. Hirota and Y. Endoh, *Physical Review Letters* **81**, 582 (1998).

10. J. A. M. van Roosmalen, E. H. P. Cordfunke, R. B. Helmholdt and H. W. Zandbergen, *Journal of Solid State Chemistry* **110**, 100 (1994).

11. M. Verelst, N. Rangavittal, C. N. R. Rao and A. Rousset, *Journal of Solid State Chemistry* **104**, 74 (1993).

12. R. Mahendiran, R. Mahesh, A. K. Raychaudhuri and C. N. R. Rao, *Solid State Communications* **94**, 515 (1995).

13. H. L. Ju, C. Kwon, Q. Li, R. L. Greene and T. Venkatesan, *Applied Physics Letters* **65**, 2108 (1994).

14. S. Sundar Manoharan, N. Y. Vasanthacharya, M. S. Hegde, K. M. Satyalakshmi, V. Prasad and S. V. Subramanyam, *Journal of Applied Physics* **76**, 3923 (1994).

15. Y. X. Jia, L. Li, K. Khazeni, V. H. Crespi, A. Zettl and M. L. Cohen, *Physical Review B* **52**, 9147 (1995).

16. R. Mahendiran, R. Mahesh, A. K. Raychaudhuri and C. N. R. Rao, *Physical Review B* **53**, 3348 (1996).

17. B. C. Hauback, H. Fjellvag and N. Sakai, *Journal of Solid State Chemistry* **124**, 43 (1996).

18. A. K. Cheetham, C. N. R. Rao and T. Vogt, *Journal of Solid State Chemistry* **126**, 337 (1996).

19. C. Ritter, M. R. Ibarra, J. M. de Teresa, P. A. Algarabel, C. Marquina, J. Blasco, J. Garcia, S. Oseroff and S. W. Cheong, *Physical Review B* **56**, 8902 (1997).

20. Q. Huang, A. Santoro, J. W. Lynn, R. W. Erwin, J. A. Borchers, J. L. Peng, K. Ghosh and R. L. Greene, *Physical Review B* **58**, 2684 (1998).

21. P. Schiffer, A. P. Ramirez, W. Bao and S. W. Cheong, *Physical Review Letters* **75**, 3336 (1995).

22. E. O. Wollan and W. C. Koehler, *Physical Review* **100**, 545 (1955).

23. P. W. Anderson and H. Hasegawa, *Physical Review* **100**, 675 (1955).

24. P.-G. De Gennes, *Physical Review* **118**, 141 (1960).

25. K. Kubo and N. Ohata, *Journal of the Physical Society of Japan* **33**, 21 (1972).

26. T. A. Tyson, Q. Qian, C. C. Kao, J. P. Rueff, F. M. F. de Groot, M. Croft, S. W. Cheong, M. Greenblatt and M. A. Subramanian, *Physical Review B* **60**, 4665 (1999).

27. Y. Okimoto, T. Katsufuji, T. Ishikawa, A. Urushibara, T. Arima and Y. Tokura, *Physical Review Letters* **75**, 109 (1995).

28. C. W. Searle and S. T. Wang, *Canadian Journal of Physics* **48**, 2023 (1970).

29. M. A. Subramanian, B. H. Toby, A. P. Ramirez, W. J. Marshall, A. W. Sleight and G. H. Kwei, *Science* **273**, 81 (1996).

30. H. L. Ju, H. C. Sohn and K. M. Krishnan, *Physical Review Letters* **79**, 3230 (1997).

31. W. E. Pickett and D. J. Singh, *Physical Review B* **53**, 1146 (1996).

32. J. H. Park, E. Vescovo, H. J. Kim, C. Kwon, R. Ramesh and T. Venkatesan, *Nature* **392**, 794 (1998).

33. J. Y. T. Wei, N. C. Yeh and R. P. Vasquez, *Physical Review Letters* **79**, 5150 (1997).

34. D. C. Worledge, L. Mieville and T. H. Geballe, *Physical Review B* **57**, 15267 (1998).

35. L. Sheng and C. S. Ting, *Physical Review B* **57**, 5265 (1998).

36. C. H. Chen and S. W. Cheong, *Physical Review Letters* **76**, 4042 (1996).

37. P. G. Radaelli, D. E. Cox, M. Marezio and S. W. Cheong, *Physical Review B* **55**, 3015 (1997).

38. S. Mori, C. H. Chen and S. W. Cheong, *Nature* **392**, 473 (1998).

39. H. Kuwahara, Y. Tomioka, A. Asamitsu, Y. Moritomo and Y. Tokura, *Science* **270**, 961 (1995).

40. V. Kiryukhin, D. Casa, J. P. Hill, B. Keimer, A. Vigliante, Y. Tomioka and Y. Tokura, *Nature* **386**, 813 (1997).

41. K. Miyano, T. Tanaka, Y. Tomioka and Y. Tokura, *Physical Review Letters* **78**, 4257 (1997).

42. A. Asamitsu, Y. Tomioka, H. Kuwahara and Y. Tokura, *Nature* **388**, 50 (1997).

43. Z. Guo-Meng, K. Conder, H. Keller and K. A. Muller, *Nature* **381**, 676 (1996).

44. J. P. Franck, I. Isaac, C. Weimin, J. Chrzanowski and J. C. Irwin, *Physical Review B* **58**, 5189 (1998).

45. I. Isaac and J. P. Franck, *Physical Review B* **57**, R5602 (1998).

46. N. A. Babushkina, L. M. Belova, O. Y. Gorbenko, A. R. Kaul, A. A. Bosak, V. I. Ozhogin and K. I. Kugel, *Nature* **391**, 159 (1998).

47. A. J. Millis, P. B. Littlewood and B. I. Shraiman, *Physical Review Letters* **74**, 5144 (1995).

48. K. Ghosh, C. J. Lobb, R. L. Greene, S. G. Katabashev, D. A. Shulyatev, A. A. Arsenov and Y. Mukovskii, *Physical Review Letters* **81**, 4740 (1998).

49. T. G. Perring, G. Aeppli, S. M. Hayden, S. A. Carter, J. P. Remeika and S. W. Cheong,, *Physical Review Letters* **77**, 711 (1996).

50. A. J. Millis, *Physical Review B* **53**, 8434 (1996).

51. H. Roder, J. Zang and A. R. Bishop, *Physical Review Letters* **76**, 1356 (1996).

52. C. H. Booth, F. Bridges, G. J. Snyder and T. H. Geballe, *Physical Review B* **54**, R15606 (1996).

53. C. H. Booth, F. Bridges, G. J. Snyder and T. H. Geballe, *Physical Review Letters* **80**, 853 (1998).

54. S. J. L. Billinge, R. G. DiFrancesco, G. H. Kwei, J. J. Neumeier and J. D. Thompson, *Physical Review Letters* **77**, 715 (1996).

55. A. Lanzara, N. L. Saini, M. Brunelli, F. Natali, A. Bianconi, P. G. Radaelli and S. W. Cheong, *Physical Review Letters* **81**, 878 (1998).

56. D. Pengcheng, H. Y. Hwang, Z. Jiandi, J. A. Fernandez-Baca, S. W. Cheong, C. Kloc, Y. Tomioka and Y. Tokura, *Physical Review B* **61**, 9553 (2000).

57. H. Y. Hwang, P. Dai, S. W. Cheong, G. Aeppli, D. A. Tennant and H. A. Mook, *Physical Review Letters* **80**, 1316 (1998).

58. Z. Guo-Meng, H. Keller and W. Prellier, *Journal of Physics: Condensed Matter* **12**, L361 (2000).

59. D. J. Singh and W. E. Pickett, *Physical Review B* **57**, 88 (1998).

60. M. L. Cohen, private communication, 1996.

61. Y. Moritomo, T. Akimoto, A. Nakamura, K. Ohoyama and M. Ohashi, *Physical Review B* **58**, 5544 (1998).

62. T. Roch, S. Yaghoubzadeh, F. S. Razavi, B. Leibold, R. Praus and H. U. Habermeier, *Applied Physics A* **A67**, 723 (1998).

63. D. N. Argyriou, J. F. Mitchell, J. B. Goodenough, O. Chmaissem, S. Short and J. D. Jorgensen, *Physical Review Letters* **78**, 1568 (1997).

64. S. Jin, T. H. Tiefel, M. McCormack, H. M. O'Bryan, L. H. Chen, R. Ramesh and D. Schurig, *Applied Physics Letters* **67**, 557 (1995).

65. M. G. Blamire, B. S. Teo, J. H. Durrell, N. D. Mathur, Z. H. Barber, J. L. McManus Driscoll, L. F. Cohen and J. E. Evetts, *Journal of Magnetism and Magnetic Materials* **191**, 359 (1999).

66. D. Cao, F. Bridges, D. C. Worledge, C. H. Booth and T. Geballe, *Physical Review B* **61**, 11373 (2000).

67. S. Lee, H. Y. Hwang, B. I. Shraiman, W. D. Ratcliff, II and S. W. Cheong, *Physical Review Letters* **82**, 4508 (1999).

68. A. K. M. A. Hossain, L. F. Cohen, F. Damay, A. Berenov, J. MacManus-Driscoll, N. M. Alford, N. D. Mathur, M. G. Blamire and J. E. Evetts, *Journal of Magnetism and Magnetic Materials* **192**, 263 (1999).

69. N. D. Mathur, G. Burnell, S. P. Isaac, T. J. Jackson, B. S. Teo, J. L. MacManus-Driscoll, L. F. Cohen, J. E. Evetts and M. G. Blamire, *Nature* **387**, 266 (1997).

70. A. H. Morrish, B. J. Evans, J. A. Eaton and L. K. Leung, *Canadian Journal of Physics* **47**, 2691 (1969).

71. Y. X. Jia, L. Li, K. Khazeni, V. H. Crespi, A. Zettl and M. L. Cohen, *Physical Review B* **52**, 9147 (1995).

72. C. J. Lu, Z. L. Wang, C. Kwon and Q. X. Jia, *Journal of Applied Physics* **88**, 4032 (2000).

73. P. W. Bridgman, *Proceedings of the American Academy of arts and Sciences* **81**, 167 (1952).

74. S. J. Clark, G. J. Ackland and J. Crain, *Physical Review B* **52**, 15035 (1995).

75. W. C. Moss, J. O. Hallquist, R. Reichlin, K. A. Goettel and S. Martin, *Applied Physics Letters* **48**, 1258 (1986).

76. A. W. Webb, D. U. Gubser and L. C. Towle, *Review of Scientific Instruments* 47, **59** (1976).

77. D. Braithwaite, G. Chouteau and G. Martinez, *Measurement Science & Technology* **1**, 1347 (1990).

78. L. Sam-Hyeon, K. Luszczynski, R. E. Norberg and M. S. Conradi, *Review of Scientific Instruments* **58**, 415 (1987).

79. S. W. Tozer and H. E. King, Jr., *Review of Scientific Instruments* **56**, 260 (1985).

80. S. A. Catledge, Y. K. Vohra, S. T. Weir and J. Akella, *Journal of Physics: Condensed Matter* **9**, L67 (1997).

81. D. Erskine, P. Y. Yu and G. Martinez, *Review of Scientific Instruments* **58**, 406 (1987).

82. M. I. Eremets, K. Shimizu, T. C. Kobayashi and K. Amaya, *Science* **281**, 1333 (1998).

83. A. Jayaraman, *Review of Scientific Instruments* **57**, 1013 (1986).

84. M. I. Eremets, *High pressure experimental methods* (Oxford University Pressq, New York, 1996).

85. I. Silvera, private communication, 1997.

86. N. H. Chen and I. F. Silvera, *Review of Scientific Instruments* **67**, 4275 (1996).

87. C. Mu and J. M. Brown, *Geophysical Research Letters* **23**, 3539 (1996).

88. *Wrought Beryllium Copper*, Brush-Wellman technical note.

89. R. Buehler, private communication, 1998.

90. S. W. Tozer, private communication, 1998.

91. R. L. Cook, H. E. King, Jr., C. A. Herbst and D. R. Herschbach, *Journal of Chemical Physics* **100**, 5178 (1994).

92. S. Iijima and T. Ichihashi, *Nature* **363**, 603 (1993).

93. J. Westwater, D. P. Gosain, S. Tomiya, S. Usui and H. Ruda, *Journal of Vacuum Science & Technology B* **15**, 554 (1997).

94. N. G. Chopra, R. J. Luyken, K. Cherrey, V. H. Crespi, M. L. Cohen, S. G. Louie and A. Zettl, *Science* **269**, 966 (1995).

95. P. M. Ajayan and S. Iijima, *Nature* **361**, 333 (1993).

96. M. M. J. Treacy, T. W. Ebbesen and J. M. Gibson, *Nature* **381**, 678 (1996).

97. J. C. Charlier, T. W. Ebbesen and P. Lambin, *Physical Review B* **53**, 11108 (1996).

98. R. Saito, G. Dresselhaus and M. S. Dresselhaus, *Physical Review B* **61**, 2981 (2000).

99. X. Blase, L. X. Benedict, E. L. Shirley and S. G. Louie, *Physical Review Letters* **72**, 1878 (1994).

100. P. Delaney, C. Hyoung Joon, I. Jisoon, S. G. Louie and M. L. Cohen, *Nature* **391**, 466 (1998).

101. A. Rochefort, P. Avouris, F. Lesage and D. R. Salahub, *Physical Review B* **60**, 13824 (1999).

102. T. W. Odom, H. Jin-Lin, P. Kim and C. M. Lieber, *Nature* **391**, 62 (1998).

103. L. C. Venema, J. W. Janssen, M. R. Buitelaar, J. W. G. Wildoer, S. G. Lemay, L. P. Kouwenhoven and C. Dekker, *Physical Review B* **62**, 5238 (2000).

104. P. Kim, T. W. Odom, H. Jin-Lin and C. M. Lieber, *Physical Review Letters* **82**, 1225 (1999).

105. A. Kasuya, M. Sugano, T. Maeda, Y. Saito, K. Tohji, H. Takahashi, Y. Sasaki, M. Fukushima, Y. Nishina and C. Horie, *Physical Review B* **57**, 4999 (1998).

106. L. Alvarez, A. Righi, T. Guillard, S. Rols, E. Anglaret, D. Laplaze and J. L. Sauvajol, *Chemical Physics Letters* **316**, 186 (2000).

107. P. G. Collins, K. Bradley, M. Ishigami and A. Zettl, *Science* **287**, 1801 (2000).

108. A. Thess, R. Lee, P. Nikolaev, H. Dai, P. Petit, J. Robert, X. Chunhui, L. Young Hee, K. Seong Gon, A. G. Rinzler, D. T. Colbert, G. E. Scuseria, D. Tomanek, J. E. Fischer and R. E. Smalley, *Science* **273**, 483 (1996).

109. J. Hone, I. Ellwood, M. Muno, A. Mizel, M. L. Cohen, A. Zettl, A. G. Rinzler and R. E. Smalley, *Physical Review Letters* **80**, 1042 (1998).

110. L. Grigorian, G. U. Sumanasekera, A. L. Lopez, S. L. Fang, J. L. Allen and P. C. Eklund, *Physical Review B* **60**, R11309 (1999).

111. T. Mingliang, L. Fanqing, C. Lin, M. Zhiqiang and Z. Yuheng, *Physical Review B* **58**, 1166 (1998).

112. B. T. Kelly, *Physics of graphite* (Applied Science, London, 1981).

113. F. J. Blatt, *Thermoelectric power of metals* (Plenum Press, New York, 1976).

114. M. S. Fuhrer, M. L. Cohen, A. Zettl and V. Crespi, *Solid State Communications* **109**, 105 (1999).

115. K. Jing, N. R. Franklin, Z. Chongwu, M. G. Chapline, P. Shu, C. Kyeongjae and D. Hongjie, *Science* **287**, 622 (2000).

116. K. Sugihara, *Physical Review B* **28**, 2157 (1983).

117. S. J. Tans, R. M. Verschueren and C. Dekker, *Nature* **393**, 49 (1998).

118. R. Martel, T. Schmidt, H. R. Shea, T. Hertel and P. Avouris, *Applied Physics Letters* **73**, 2447 (1998).

119. J. W. G. Wildoer, L. C. Venema, A. G. Rinzler, R. E. Smalley and C. Dekker, *Nature* **391**, 59 (1998).

120. O. Teri Wang, H. Ji-Lin, K. Philip, O. Min and C. M. Lieber, *Journal of Materials Research* **13**, 2380 (1998).

121. P. L. McEuen, M. Bockrath, D. H. Cobden, Y. G. Yoon and S. G. Louie, *Physical Review Letters* **83**, 5098 (1999).

122. C. K. W. Adu, G. U. Sumanasekera, B. K. Pradhan, H. E. Romero and P. C. Eklund, *Chemical Physics Letters*, 31 (2001).

123. J. Seung-Hoon, S. G. Louie and M. L. Cohen, *Physical Review Letters* **85**, 1710 (2000).

124. M. A. Hamon, J. Chen, H. Hu, Y. Chen, M. E. Itkis, A. M. Rao, P. C. Eklund and R. C. Haddon, *Advanced Materials* **11**, 835 (1999).

125. Y. Zhen, C. L. Kane and C. Dekker, *Physical Review Letters* **84**, 2941 (2000).

126. K. Jing, H. T. Soh, A. M. Cassell, C. F. Quate and D. Hongjie, *Nature* **395**, 878 (1998).

127. T. Rueckes, K. Kim, E. Joselevich, G. Y. Tseng, C. L. Cheung and C. M. Lieber, *Science* **289**, 94 (2000).

128. W. B. Choi, D. S. Chung, J. H. Kang, H. Y. Kim, Y. W. Jin, I. T. Han, Y. H. Lee, J. E. Jung, N. S. Lee, G. S. Park and J. M. Kim, *Applied Physics Letters* **75**, 3129 (1999).

129. P. G. Collins, M. S. Fuhrer and A. Zettl, *Applied Physics Letters* **76**, 894 (2000).

130. J. P. Pelz, Ph.D. thesis, University of California at Berkeley, 1987.

131. I. N. Hooge, in *Noise in physical systems and 1/f noise*, edited by A. D'Amico and P. Mazzetti (Elsevier Science Publishers, 1985).

132. P. Dutta and P. M. Horn, *Reviews of Modern Physics* **53**, 479 (1981).

133. M. S. Fuhrer, J. Nygard, L. Shih, M. Forero, Y. Young-Gui, M. S. C. Mazzoni, C. Hyoung Joon, I. Jisoon, S. G. Louie, A. Zettl and P. L. McEuen, *Science* **288**, 494 (2000).

134. R. F. Voss and J. Clarke, *Physical Review B* **13**, 556 (1976).

135. A. Mizel, L. X. Benedict, M. L. Cohen, S. G. Louie, A. Zettl, N. K. Budraa and W. P. Beyermann, *Physical Review B* **60**, 3264 (1999).

136. M. Bockrath, D. H. Cobden, P. L. McEuen, N. G. Chopra, A. Zettl, A. Thess and R. E. Smalley, *Science* **275**, 1922 (1997).

137. M. Bockrath, D. H. Cobden, L. Jia, A. G. Rinzler, R. E. Smalley, L. Balents and P. L. McEuen, *Nature* **397**, 598 (1999).

138. D. Hongjie, E. W. Wong and C. M. Lieber, *Science* **272**, 523 (1996).

139. T. W. Ebbesen, H. J. Lezec, H. Hiura, J. W. Bennett, H. F. Ghaemi and T. Thio, *Nature* **382**, 54 (1996).

140. E. Abrahams, P. W. Anderson, D. C. Licciardello and T. V. Ramakrishnan, *Physical Review Letters* **42**, 673 (1979).

141. C. T. White and T. N. Todorov, *Nature* **393**, 240 (1998).

142. T. Ando, T. Nakanishi and R. Saito, *Journal of the Physical Society of Japan* **67**, 2857 (1998).

143. T. Ando and T. Nakanishi, *Journal of the Physical Society of Japan* **67**, 1704 (1998).

144. M. Igami, T. Nakanishi and T. Ando, *Journal of the Physical Society of Japan* **68**, 716 (1999).

145. L. Chico, L. X. Benedict, S. G. Louie and M. L. Cohen, *Physical Review B* **54**, 2600 (1996).

146. C. Hyoung Joon, I. Jisoon, S. G. Louie and M. L. Cohen, *Physical Review Letters* **84**, 2917 (2000).

147. A. Rochefort and P. Avouris, *Journal of Physical Chemistry A* **104**, 9807 (2000).

148. J. Nygard, D. H. Cobden and P. E. Lindelof, *Nature* **408**, 342 (2000).

149. W. Schottky, *Annalen der Physik* **57**, 541 (1918).

150. X. Jehl, M. Sanquer, R. Calemczuk and D. Mailly, *Nature* **405**, 50 (2000).

151. P. Dieleman, H. G. Bukkems, T. M. Klapwijk, M. Schicke and K. H. Gundlach, *Physical Review Letters* **79**, 3486 (1997).

152. R. De-Picciotto, M. Reznikov, M. Heiblum, V. Umansky, G. Bunin and D. Mahalu, *Nature* **389**, 162 (1997).

153. M. Reznikov, R. De Picciotto, T. G. Griffiths, M. Heiblum and V. Umansky, *Nature* **399**, 238 (1999).

154. R. Landauer, *IBM Journal of Research and Development* **1**, 223 (1957).

155. R. Landauer, *Philosophical Magazine* **21**, 863 (1970).

156. R. Buttiker, Y. Imry, R. Landauer and S. Pinhas, *Physical Review B* **31**, 6207 (1985).

157. G. B. Lesovik, *Soviet Physics- JETP Letters* **49**, 592 (1989).

158. T. Martin and R. Landauer, *Physical Review B* **45**, 1742 (1992).

159. M. Reznikov, M. Heiblum, H. Shtrikman and D. Mahalu, *Physical Review Letters* **75**, 3340 (1995).

160. H. E. van den Brom and J. M. van Ruitenbeek, *Physical Review Letters* **82**, 1526 (1999).

161. E. Scheer, W. Belzig, Y. Naveh, M. H. Devoret, D. Esteve and C. Urbina, *Physical Review Letters* **86**, 284 (2001).

162. C. W. J. Beenakker and M. Buttiker, *Physical Review B* **46**, 1889 (1992).

163. V. I. Kozub and A. M. Rudin, *Physical Review B* **52**, 7853 (1995).

164. F. Liefrink, J. I. Dijkhuis, M. J. M. de Jong, L. W. Molenkamp and H. van Houten, *Physical Review B* **49**, 14066 (1994).

165. M. Henny, S. Oberholzer, C. Strunk and C. Schonenberger, *Physical Review B* **59**, 2871 (1999).

166. M. J. M. de Jong and C. W. J. Beenakker, *Physical Review B* **46**, 13400 (1992).

167. D. K. Ferry and S. Goodnick, *Transport in nanostructures* (Cambridge University Press, Cambridge, 1997).

168. S. Hershfield, J. H. Davies, P. Hyldgaard, C. J. Stanton and J. W. Wilkins, *Physical Review B* **47**, 1967 (1993).

169. A. N. Korotkov, *Physical Review B* **49**, 10381 (1994).

170. D. H. Cobden, N. K. Patel, M. Pepper, D. A. Ritchie, J. E. F. Frost and G. A. C. Jones, *Physical Review B* **44**, 1938 (1991).

171. S. Sasaki, K. Tsubaki, S. Tarucha, A. Fujiwara and Y. Takahashi, *Solid State Electronics* **42**, 1429 (1998).

172. J. Voit, *Reports on Progress in Physics* **58**, 977 (1995).

173. C. Kane, L. Balents and M. P. A. Fisher, *Physical Review Letters* **79**, 5086 (1997).

174. C. L. Kane and M. P. A. Fisher, *Physical Review Letters* **72**, 724 (1994).

175. C. de C. Chamon, D. E. Freed and X. G. Wen, *Physical Review B* **51**, 2363 (1995).

176. U. Weiss, R. Egger and M. Sassetti, *Physical Review B* **52**, 16707 (1995).

177. V. V. Ponomarenko, *Physical Review B* **54**, 10328 (1996).

178. H. T. Soh, C. F. Quate, A. F. Morpurgo, C. M. Marcusa, K. Jing and D. Hongjie, *Applied Physics Letters* **75**, 627 (1999).

179. A. M. Cassell, J. A. Raymakers, K. Jing and D. Hongjie, *Journal of Physical Chemistry B* **103**, 6484 (1999).

180. S. Kogan, *Electronic noise and fluctuations in solids* (Cambridge University Press, Cambridge, 1996).